

An Atomistic Simulation Method for Oxygen Impurities in Aluminium Based on Variable Charge Molecular Dynamics

THÈSE N° 4702 (2010)

PRÉSENTÉE LE 21 MAI 2010

À LA FACULTÉ SCIENCES ET TECHNIQUES DE L'INGÉNIEUR
LABORATOIRE DE MÉTALLURGIE MÉCANIQUE
PROGRAMME DOCTORAL EN SCIENCE ET GÉNIE DES MATÉRIAUX

ÉCOLE POLYTECHNIQUE FÉDÉRALE DE LAUSANNE

POUR L'OBTENTION DU GRADE DE DOCTEUR ÈS SCIENCES

PAR

Andreas ELSENER

acceptée sur proposition du jury:

Prof. N. Baluc, présidente du jury
Prof. H. Van Swygenhoven, directrice de thèse
Prof. M. Hou, rapporteur
Prof. E. Kaxiras, rapporteur
Prof. R. Spolenak, rapporteur



ÉCOLE POLYTECHNIQUE
FÉDÉRALE DE LAUSANNE

Suisse
2010

Abstract

Impurities are known to have a significant impact on materials properties. In particular, the presence of impurities can change mechanical properties and stabilize the microstructure by reducing grain growth and recrystallization processes.

In the past atomistic simulations, in particular molecular dynamics, have contributed a lot to the understanding of deformation mechanisms in nanocrystalline metals. Especially, insights into details of dislocation/GB interactions have been gained. Additionally, simulations on coupled grain boundary migration in bicrystalline samples have played an important role in understanding stress assisted grain growth in nanocrystalline metals. However, all these simulations have been performed on monatomic systems. This means that the role of impurities has not yet been considered in these simulations.

Some of the important difference between experiments and simulations could be removed by introducing dilute O distributions to computational Al samples. For this purpose, a simulation method is required which can deal with the oxidation of Al atoms around the O impurities and which can simulate the ionic and metallic nature of bonding simultaneously.

Here, a method is suggested which fulfills the requirements by modifying the variable charge method of Streitz and Mintmire [Phys. Rev. B **50**, 11996 (1994)]. A local chemical potential approach which optimizes the charge on only those atoms expected to be ionic is developed. Additionally the EAM potential for the non-electrostatic interaction given in the publication of Streitz and Mintmire is substituted by empirical potentials which treat the Al-Al interactions with a well-known Al potential. The Al-O and O-O interactions in these EAM potentials are fitted for the simulation of dilute O impurities in Al and additionally for the simulation of corundum in case of a second potential.

The aforementioned developments are applied to study the effect of O impurities on the deformation of nc Al. A fully three-dimensional nc sample containing 15 grains of 12 nm grain-size is deformed with a dilute O content in the triple junction lines. The impact of O impurities on dislocation propagation is also considered in a sample which consists of a single grain extracted from a large molecular dynamics simulation. This simulation geometry contains a perfect dislocation, which is pinned at the surrounding grain boundary network. Therefore it allows the study of pinning strength and after unpinning the propagation behavior of the

dislocation under various O impurity distributions. Additionally, the role of O impurities on coupled GB migration is investigated by studying two bicrystalline samples with different O distributions in both of them.

In the discussion, the emphasis is on the simulation method. Especially, the significance of the samples, simulation conditions and the performance of the method in the different applications are discussed. Additionally, the different developments (local chemical potential approach and EAM potentials) are critically analyzed and improvements for future simulations of impurities are suggested.

Keywords: Variable charge molecular dynamics, impurities, nanocrystalline aluminium, dislocation propagation, coupled grain boundary migration

Zusammenfassung

Verunreinigungen sind für ihren bedeutenden Einfluss auf Materialeigenschaften bekannt. Im Speziellen kann die Anwesenheit von Verunreinigungen mechanische Eigenschaften verändern und die Mikrostruktur durch die Verminderung von Kornwachstums- oder Rekristallisationsprozessen stabilisieren.

In der Vergangenheit haben atomistische Simulationen, insbesondere Moleküldynamiksimulationen, viel zum Verständnis von Verformungsmechanismen in nanokristallinen Metallen beigetragen. Vor allem hat man Einblick in Details von Versetzungskornrenzinteraktionen gewonnen. Zusätzlich haben Simulationen zu gekoppelter Korngrenzbewegung in bikristallinen Proben eine wichtige Rolle für das Verständnis von spannungsgetriebenem Kornwachstum in nanokristallinen Metallen gespielt. Allerdings, sind all diese Simulationen in einatomigen Systemen durchgeführt worden. Das heisst, die Rolle von Verunreinigungen ist bis jetzt in diesen Simulationen nicht berücksichtigt worden.

Ein Teil dieses wichtigen Unterschiedes zwischen Experimenten und Simulationen könnte durch das Einführen von verdünnten O-Verteilungen in numerischen Al-Proben beseitigt werden. Zu diesem Zweck wird eine Simulationsmethode, welche die Oxidation von Al-Atomen in der Nähe von O-Verunreinigungen handhaben und die gleichzeitig die ionischen und die metallische Bindungsart simulieren kann, benötigt.

Hier wird eine Methode vorgeschlagen, die diese Anforderungen durch das Modifizieren der Variablen-Ladungs-Methode von Streitz und Mintimire [Phys. Rev. B **50**, 11996 (1994)] erfüllt. Ein Ansatz für lokale chemische Potentiale wird entwickelt, der die Ladung nur für jene Atome optimiert, welche als ionisierbar angenommen werden. Zusätzlich wird das „EAM“-Potential für die nicht-elektrostatische Wechselwirkung in Streitz und Mintmires Publikation durch empirische Potentiale, welche die Al-Al-Wechselwirkung mit einem bekannten Al-Potential modellieren, ersetzt. Die Al-O- und die O-O-Interaktionen werden in diesen „EAM“-Potentialen für die Simulation von verdünnten O-Verunreinigungen in Al und zusätzlich für die Simulation von Korund im Falle des zweiten Potentials, gefittet.

Die erwähnten Entwicklungen werden zum Studium des Einflusses von O-Verunreinigungen auf die Verformung von nanokristallinem Al eingesetzt. Eine dreidimensionale nanokristalline Probe mit 15 Körnern von 12 nm Grösse wird mit einer verdünnten O-Verteilung in den

Tripellinien der Korngrenzen verformt. Der Effekt der O-Verunreinigungen auf die Versetzungsbewegung wird an Hand einer Probe, die aus einem einzigen Korn besteht, das von einer grossen Moleküldynamiksimulation extrahiert wurde, untersucht. Die Simulationsgeometrie beinhaltet eine perfekte Versetzung, die am umgebenden Korngrenznetzwerk verankert ist. Darum erlaubt diese Probe das Studium der Festhaltstärke und das Bewegungsverhalten der Versetzung nach deren Loslösen unter dem Einfluss von verschiedenen O-Verunreinigungsverteilungen. Zusätzlich wird die Rolle von O-Verunreinigungen auf die gekoppelte Korngrenzbewegung durchs Studium von zwei Bikristallen untersucht, wobei in beiden Proben mehrere O-Verteilungen eingesetzt werden.

In der Diskussion liegt der Schwerpunkt auf der Simulationsmethode. Im Speziellen, werden die Bedeutsamkeit der Proben, die Simulationsbedingungen und die Leistung der Methode in den verschiedenen Anwendungen besprochen. Zusätzlich, werden die Entwicklungen (Ansatz vom Lokalen-chemischen-Potential und die „EAM“-Potentiale) kritisch analysiert und Verbesserungen für die zukünftige Simulationen von Verunreinigungen vorgeschlagen.

Schlüsselwörter: Moleküldynamik mit variablen Ladungen, Verunreinigungen, nanokristallines Aluminium, Versetzungsbewegung, gekoppelte Korngrenzbewegung

Résumé

Les impuretés sont connues pour avoir un impact significatif sur les propriétés des matériaux. En particulier, la présence d'impuretés peut drastiquement changer les propriétés mécaniques ou stabiliser la microstructure en réduisant les mécanismes de grossissement de grains ou de recristallisation.

Dans le passé, les simulations atomistiques, en particulier par dynamique moléculaire, ont beaucoup contribué à la compréhension des mécanismes de déformation des matériaux nanocristallins. Elles ont notamment permis une meilleure connaissance des interactions entre dislocations et joints de grains. De plus, les simulations du déplacement couplé des joints de grains dans des bi-cristaux ont joués un rôle important pour la compréhension de la croissance des grains dans les matériaux nanocristallins sous contraintes. Cependant, ces simulations ont été restreintes à des systèmes monoatomiques et le rôle des impuretés toujours négligé.

Une partie des différences observées entre les expériences et les simulations pourrait être supprimée en introduisant une faible concentration d'oxygène dans les échantillons d'aluminium. Dans ce but, il est nécessaire de disposer d'une méthode de simulations pouvant traiter l'oxydation des atomes Al autour des impuretés O et pouvant décrire simultanément des liaisons ioniques et des liaisons métalliques,

Ici, une méthode répondant à ces exigences est proposée en modifiant la méthode des charges variables de Streit et Mintmire [Phys. Rev. B **50**, 11996 (1994)]. Une approche de potentiel chimique local, qui optimise seulement les charges des atomes attendus à devenir ionique, est développée. De plus, les potentiels «EAM» utilisés par Streit et Mintmire pour décrire les interactions non-électrostatiques sont substitués par de nouveaux potentiels empiriques bien connus pour représenter les interactions Al-Al. Pour ces potentiels «EAM», les interactions Al-O et O-O furent déterminées pour la simulation d'impureté d'O dans Al et pour la simulation de la structure corindon dans un second temps.

Les développements mentionnés ci-dessus sont appliqués à l'étude de l'effet des impuretés d'O sur la déformation de Al nanocristallin. Un échantillon nanocristallin tridimensionnel contenant 15 grains de 12 nm est déformé en présence d'O dilué aux lignes de jonctions triples entre les joints de grains. L'impact des impuretés d'O sur la propagation des dislocations est également considéré dans un échantillon consistant d'un grain extrait d'une simulation par dynamique

moléculaire à grande échelle. Cette géométrie contient une dislocation parfaite qui est ancrée aux joints de grains environnants. Elle permet donc l'étude de la force d'ancrage et du comportement de la propagation de la dislocation après sa libération pour différentes distributions des impuretés d'O. De plus, le rôle des impuretés d'O sur le mouvement des joints de grain est analysé en étudiant deux échantillons bicristallins contenant différentes distributions d'O.

Dans la discussion, l'accent est mis sur la méthode de simulation. Surtout, les significations des échantillons, des conditions de simulations et la performance de la méthode pour différentes applications sont discutés. De plus, les différents développements (méthode du potentiel chimique local et des potentiels «EAM») sont analysés de façon critique et des améliorations pour de futures simulations des impuretés sont proposées.

Mots clés: Dynamique moléculaire à charges variables, impuretés, aluminium nanocristallin, propagation de dislocations, mouvement couplé de joints de grains.

Abbreviations

Sample description

nc	nanocrystalline
fcc	face center cubic
hcp	hexagonal close packed
GB/GBs	grain boundary/boundaries

Methods

TEM	transmission electron microscope/microscopy
EELS	electron energy loss spectroscopy

MD	molecular dynamics
MS	molecular statics
EAM	embedded-atom method
MEAM	modified embedded-atom method

DFT	density functional theory
LDA	local density approximation
GGA	generalized gradient approximation

Units

nm	nanometer ($= 10^{-9}$ m)
Ang.	angstroms ($= 10^{-10}$ m)
ps/fs	pico- or femtoseconds ($= 10^{-12}$ or 10^{-15} s)
MPa/GPa	mega- or gigapascal ($= 10^6$ or 10^9 N/m ²)
K	kelvin
E	elementary charge ($= 1.602 \times 10^{-19}$ C)
eV	electronvolt ($= 1.602 \times 10^{-19}$ J)

Local crystallinity classes

Color-code used in visualizations

Grey	fcc atoms
Red	hcp atoms
Green	other 12 coordinated atoms
Blue	non 12 coordinated atoms
Yellow	O atoms

Contents

Abstract	iii
Zusammenfassung	v
Résumé	vii
Abbreviations	ix
Local crystallinity classes	ix
Contents	x
1 Introduction	1
1.1 Deformation of polycrystalline metals.....	2
1.2 Nanocrystalline face centered cubic metals.....	7
1.2.1 Experimental work	8
1.2.2 Molecular dynamics simulations.....	9
1.3 A method for oxygen impurities in aluminum.....	11
2 Simulation methods	15
2.1 Ab initio.....	16
2.1.1 Density functional theory	17
2.1.2 Limitations of ab initio methods.....	19
2.2 Molecular dynamics.....	19
2.2.1 Basics.....	19
2.2.2 Interaction potentials	22
2.2.3 Additional simulation techniques	24
2.2.4 Atomic properties and visualization.....	26
2.3 Molecular dynamics with charged atoms	29
2.3.1 Streitz and Mintmire's potential.....	30
2.3.2 Ewald summation	34
2.3.3 Application and improvements of Streitz and Mintmire's method	36

3	Results on developments	39
3.1	Development I - Local chemical potential approach	40
3.1.1	Motivation	40
3.1.2	Streitz and Mintmire's approach reconsidered	41
3.1.3	Charge optimization for the dilute oxygen limit	42
3.1.4	Optimization of long-range interaction	45
3.1.5	Timing of the approach	47
3.1.6	Implementation	48
3.2	Development II - First potential	49
3.2.1	Motivation	49
3.2.2	Simulation of defect structures	49
3.2.3	Fitting procedure	52
3.2.4	Results	54
3.3	Development III – Second potential	57
3.3.1	Motivation	57
3.3.2	Fitting procedure	58
3.3.3	Results	60
3.3.4	Comparison to first potential	62
4	Results on applications	65
4.1	Application I - Nanocrystalline structures	66
4.1.1	Motivation	66
4.1.2	Sample description and simulation details	66
4.1.3	Results	69
4.1.4	Discussion	73
4.2	Application II – Dislocation propagation	74
4.2.1	Motivation	74
4.2.2	Sample description and simulation details	74
4.2.3	Results	76
4.2.4	Discussion	95
4.3	Application III - Coupled grain boundary migration	97
4.3.1	Motivation	97
4.3.2	Sample description and simulation details	98
4.3.3	Results on the $\Sigma 75$ sample	99
4.3.4	Results on the $\Sigma 21$ sample	116

4.3.5	Discussion	119
5	Discussion	123
5.1	Applications	124
5.1.1	Samples and simulation conditions	124
5.1.2	Performance of the method	126
5.2	Developments	128
5.2.1	Local chemical potential approach.....	128
5.2.2	EAM potentials.....	130
6	Conclusions and outlook	133
	References	137
	Appendix A - The corundum structure	a
	Appendix B – Partial charge determination	c
	A personal retrospect	e
	Curriculum vitae	h

“Most properties of solids depend on the microstructure [...]”

H. Gleiter, 2000.

1 Introduction

1.1 Deformation of polycrystalline metals

In polycrystalline metals, i.e. metals consisting of several crystals or grains with different orientations, numerous and often competing mechanisms can occur during the plastic deformation depending on the temperature, the strain rate and/or the applied stress. For example, it is known that at higher temperatures ($> 0.4 T_m$, where T_m is the melting point of the material) an anelastic deformation can occur under smaller applied stresses than the yield stress of the material. This time-dependent deformation of the material is known as creep. Different mechanisms are known which contribute to creep, e.g. Coble creep (vacancies diffuse along GBs), Nabarro-Herring creep (vacancies diffuse through the lattice) or dislocation climb (dislocation climb is driven by the diffusion of point defects). All the mechanism can be assigned to diffusion processes. Due to the time-scale restriction of classical MD simulations diffusion based mechanisms are difficult to access by simulations. Therefore, a restriction to the lower temperature regime (below $0.4 T_m$) where the deformation of coarse grained polycrystalline metals is dominated by dislocation glide is made for this work. Additionally GB processes, especially coupled GB migration, are introduced because it is studied in one of the applications for the newly developed method.

Dislocations, i.e. line defects of the regular crystal lattice, determine the deformation behavior via their interaction with point defects, other dislocations and/or interfaces such as GBs. Dislocation-dislocations interactions are very diverse and can even lead to dislocation networks during the deformation of coarse-grained polycrystals. However these interactions and dislocation networks are less relevant in nc materials (see section 1.2). Therefore these interactions are not explained in this introduction.

Dislocations are present in the as-prepared state of a coarse grained polycrystalline metal due to stresses (mechanical, thermal, ...) coming from the materials processing. If a coarse-grained metal is plastically deformed, the dislocation density increases and more dislocations have to be generated. If a crystal is defect free dislocations would have to nucleate in a homogenous way which requires very high stresses as e.g. Hirth and Lothe calculated¹. Homogenous dislocation nucleation is rather unlikely due to the high stresses and the pre-existing defects. Nucleation stresses are reduced by the presence of stress concentrations in the crystal. Stress concentrations can be found at defects such as precipitates, interstitials or vacancies. However the classical mechanism for dislocation generation in a polycrystalline metal is the Frank-Read source where dislocations are bulged out between two existing pinning points. After bowing around the

existing pinning point, two parts of the dislocation can annihilate and form a dislocation loop and a new segment between the existing pinning points. The stress required to bow a dislocation is proportional to one over to the distance between the pinning points. Frank-Read sources can cease their operation if the distance between the pinning points becomes too small because the stress to bow out dislocations can ultimately reach the value of the theoretical shear stress ². Dislocations can be nucleated from GBs, too. Stress concentrations such as triple junctions, ledges or “GB dislocations” are possible nucleation sites. Dislocation nucleation from GBs was predicted already in the sixties in a theoretical approach by Li ³.

In fcc materials, dislocations usually dissociate in two partials: A leading and a trailing partial dislocation. Between the two partials, there is a stacking fault. If a leading partial propagates without nucleation of a trailing, an extended stacking fault is formed. If in this case a second partial dislocation nucleates on adjacent plane and moves also through the whole grain, a twin faults is formed.

Dislocations propagate during the deformation and produce slip. They can e.g. propagate as expanding loops which are produced by Frank-Read sources. As a dislocation can never end in the perfect crystal, GBs or other defects act as dislocation sinks and dislocations can be attached to them. In general GBs are strong barriers for dislocation propagation. By the reduction of the grain-size the interface density increases. Grain refinement leads to an increase in yield strength which scales with one over square-root of the grain-size in coarse-grained crystalline materials. This relationship is known as the Hall-Petch law^{4, 5} and is traditionally explained by the pile-up of dislocations at GBs.

For the interaction of dislocations with defects other than interfaces and/or dislocations, the interaction with point defects, solute atoms, precipitates, dispersions or voids can be considered. The interaction of dislocations with voids and vacancies will not be addressed here. However the interaction with solute atoms and precipitates is relevant as later the effect of O impurities on dislocations is investigated.

Solute atoms are present in a metallic matrix as substitutions, i.e. at lattice sites, if they are of roughly the same size as matrix atoms or as interstitials, i.e. between the matrix atoms, which is usually the case for smaller solute atoms. A solute atom induces a strain and/or stress field which can hinder the mobility of dislocations. The difference in size causes a so-called parelastic effect and the difference in shear modulus induces a so-called dielastic interaction between impurities and dislocations. Both parelastic and dielastic stress fields around the impurities and combinations of them interact with the stress field caused by dislocations.

However there is no parelastic interaction with screw dislocations because the screw has no hydrostatic stress field. The dielastic interaction between solutes and dislocations is of short-range and the parelastic is long-range. There are other types of interaction between dislocations and solute atoms such as the chemical or the electrical. For the chemical interaction, the Suzuki effect, where the stacking fault energies are reduced by the presence of impurities, is well known. The electrical effect in a metal is caused by the conduction electrons, which are rearranged due to the variation in hydrostatic pressure around an edge dislocation. This leads to the formation of an electrical dipole at the dislocation which can interact with the electronic charge of the impurities.

The presence of obstacles such as solute atoms hinders dislocation motion and extra stresses are required to overcome these obstacles. Dislocations can be imagined as flexible bands which are pinned at the obstacles and bow between them (Figure 1.1). The additional stress required for the bowing is inversely proportional to the interparticle distance analogous to the case of Frank-Read sources. The increase in strength due to small particles is proportional to the square root of the particle concentration.



Figure 1.1 In crystals, the obstacles (blue spheres) are arranged in an irregular pattern. The orange line represents a pinned dislocation. Taken from Ref. ⁶

If the mobility of the impurities is high enough, they can cluster and even form second phases, so-called precipitates. The interface between the precipitate and the matrix can either be coherent, semicoherent or incoherent. The interaction with a dislocation can happen in several ways: Dislocations can be pinned at precipitates as it was seen in TEM experiments ⁷, they can cut through precipitates (Figure 1.2b) or they can navigate around them (Figure 1.2a). Cutting means that a dislocation moves through the precipitates and shears it (Figure 1.2b). For this, a coherent interface between the matrix and the precipitate is required to have a continuous slip plane. If the dislocation bypasses the obstacle, this can for instance happen by an Orowan mechanism (Figure 1.2a). In this mechanism, the dislocation bows between the particles leaving

a dislocation loop about each particle. Alternatively, dislocations overcome obstacles by climb or cross-slipping (Figure 1.2c). Whether an Orowan mechanism or cutting is observed is determined by the precipitate size, its strength and the interfacial energy. The cutting strength is dependent on the square root of the precipitate size whereas the Orowan strength (bowing) is inversely dependent on precipitate size. Therefore a change of mechanisms can be expected depending on the precipitate size. A precipitate has a maximal strength if its size is at the crossover between the two mechanisms. This change in mechanism is observed for Al-Sc alloys where Al_3Sc precipitates are formed. In case of precipitate sizes around 1.4 nm cutting is observed and for size of 5.9 nm the precipitates are bypassed according to the Orowan mechanism⁸.

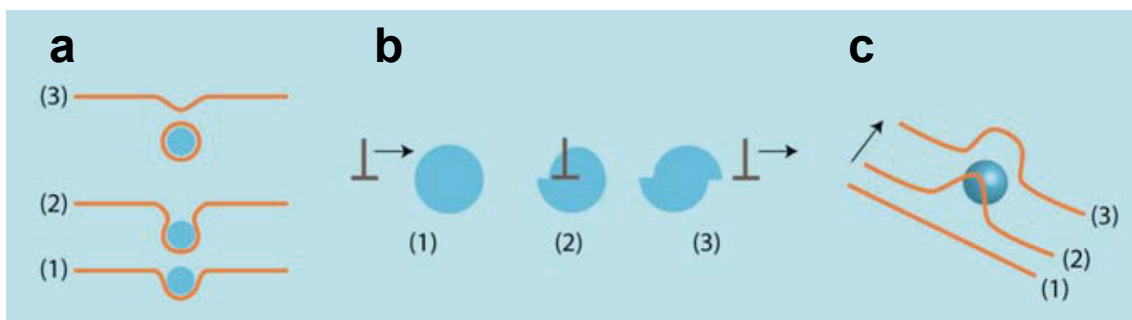


Figure 1.2 Different interaction mechanisms between dislocation and precipitates. The number correspond with the temporal evolution. (a) Orowan bowing mechanism in which a dislocation loop is left behind. (b) Cutting of a precipitate by passage of an edge dislocation. (c) Bypass of an obstacle via dislocation climb. Extracted from Ref. ⁶.

The load applied on a polycrystal acts also on GBs (Figure 1.3a). Different non-diffusion based responses can be expected such as dislocation emission into the grains (Figure 1.3b), interface sliding (Figure 1.3c), interface migration coupled to shear deformation (Figure 1.3d), crack nucleation and propagation or combinations of them. Stress induced GB motion has e.g. been observed by ab initio⁹⁻¹¹, MD simulations¹²⁻¹⁶ and experiments on low angle^{17, 18} and high angle GBs¹⁹⁻²⁷.

Coupling means that a GB responds to shear deformation or other driving forces tangential to the interfacial plane with motion normal to the GB plane. Cahn and Taylor²⁸ constructed a theory which shows that coupling is a feature which is valid for a lot of GBs. Coupled GB motion has been observed in many GBs using simulations²⁹⁻³², and experiments in bicrystalline metals^{21, 22, 25-27, 33, 34} and ceramics²⁴. From theory²⁸ it is known that for curved GBs the coupling effect induces grain rotation which has been confirmed by simulations in columnar structures³⁵. There are also exceptions for coupling: It is not possible to have coupling for pure twist GBs²⁹, as the dislocation content of the twist GB induces GB sliding under shear

deformation. Simulations have shown that triple junctions and other defects can shutdown coupling³⁵. In simulations of Cu bicrystals it has also been observed that high temperatures (above $0.7 T_m$) can activate sliding mechanisms with lower critical stresses²⁹. So sliding instead of coupled GB motion is then the dominant response to the applied shear stress. Independent of this, coupled GB migration is considered as possible source for stress driven GB motion or stress induced grain growth (see section 1.2 on nc metals).

The mechanism of coupled GB motion is not based on diffusion. It is determined by the transformation of the structural units which form the GBs. Usually it is observed as a stick-slip process (see e.g. Figure 4.33) where the shear stress rises until a critical value is reached and drops then rapidly. At the critical stress the migration event is triggered. The value of the critical stress scales with the tangential velocity parallel to the GB and depends on the temperature²⁹.

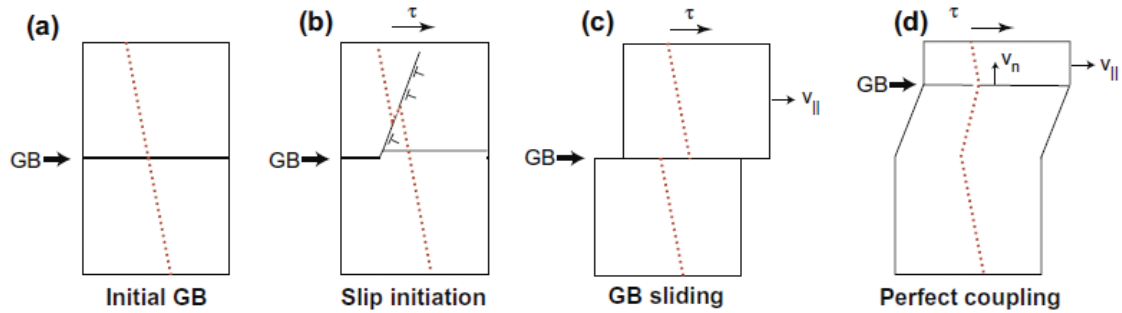


Figure 1.3 Possible mechanical responses of a plane GB to applied shear stresses. (a) Initial bicrystal with a dotted line showing a set of inert markers. (b) The GB initiates slip by emitting a dislocation. (c) Rigid GB sliding with a grain translation velocity $v_{||}$; note the discontinuity of the marker line. (d) GB motion coupled to shear deformation (v_n is the normal GB velocity). Extracted from Ref.³⁶.

Geometrical conditions determine the coupling constants, i.e. the ratio between the tangential velocity of the bicrystal parallel to the GB over the normal velocity of the GB. Simulations have shown that these coupling constants are independent of the tangential velocities or temperatures and depend only on the geometry²⁹. The Frank-Bilby equation³⁷, which determines the Burgers vector content of a GB, can be used to determine such coupling constants. Due to symmetry of crystals the Frank-Bilby equation can have multiple solutions which can result in more than one coupling constant or mode for a given system. Multiple coupling modes for one bicrystal can also be observed in simulations²⁹. Which coupling mode is active depends on the critical resolved shear stress of the present modes²⁹. Recently a generalization of the concept for coupling constants was proposed by Caillard³⁸ with which many more coupling constants can

be derived. They can be used to rationalize recent TEM investigations on coupled GB migration
26

Impurities interact also with GBs, which is in the simplest case an elastic interaction. However also electronic interactions have to be taken into account: The energy of the elastic stress field of the GB and the impurity is lower if the impurity is present in the GB instead of the undisturbed lattice³⁹. This causes an attractive force between impurities and GBs which can lead to segregation of impurities to GBs. If a GB which contains impurities starts to move, the foreign atoms will be left behind. However the attractive force between the GB and the impurities gives the diffusion of the impurities a net direction towards the new GB position. In case of slow enough GBs the impurities are able to follow or move with the GB. The segregation of impurities to GBs leads to a drag effect on the GB mobility³⁹⁻⁴¹ which arises from the fact that the mobile dislocation has to overcome the attractive force due to the impurities.

Solute segregation of impurities to GBs is also related to mechanical behavior of materials through embrittlement effects³⁶. For some impurities (e.g. H, O, S and P) it is known that segregation to GBs reduces their cohesion which can turn otherwise ductile materials to brittle materials. For other elements (e.g. B and C) an increasing GB cohesion or an expelling of harmful elements from GBs by site competition can be expected which improves mechanical behavior. In Al it is Ga which is known from ab initio simulations^{42, 43} to cause severe GB embrittlement. In reference⁴⁴ it is expected that embrittling impurities should have a stronger binding to surfaces than to GBs. The opposite is expected for GB-strengthening elements. Electronic effects such as charge transfer towards the impurities are possible reasons for weakening of the bonding in impure interfaces which can lead to the aforementioned embrittlement. As chemical effects are involved in these segregation and embrittlement mechanisms, ab initio simulations are more successful in uncovering atomistic process than MD simulations which rely on empirical potentials. However, MD simulations of impurities in GBs are emerging as it will be shown at the end of section 1.2.2.

1.2 Nanocrystalline face centered cubic metals

Nc fcc metals are conventionally defined as polycrystalline metals with a mean grain-size below 100 nm. These materials have very appealing properties such as an ultra-high strength but also a reduced elongation to failure. If the ultra-high strength of nc materials is explained with the Hall-Petch law one implicitly assumes the existence of dislocations in nc materials. However in small grains the stress to bow out a dislocation increases significantly and might reach even the

theoretical shear strength⁴⁵. So a limitation in the usual dislocation multiplication processes must be expected due the reduced grain sizes⁴⁶.

With further grain-refinement a break-down of the Hall-Petch law is observed. Sometimes materials with very small grains become even softer. This indicates that a different mechanism than the conventional dislocation generation from Frank-Read sources is present and that dislocation-dislocation interactions and dislocation pile-up at GBs are less relevant in nc materials. It is envisioned that GBs become more effective as the interface density increase significantly in nc metals.

1.2.1 Experimental work

Postdeformation analysis in compressed or indented nc Ni does not show major dislocation debris^{2, 47}. In contrast, there are TEM observations which show twinning in nc Al at low temperature and high strain⁴⁸. Twinning indicates the operation of partial dislocations. Additionally, there are high-resolution TEM experiments for cold-rolled nc Ni where dislocation activity and even dislocation accumulation inside grains was observed under severe plastic deformation⁴⁹. So dislocation activity is also observed in nc materials although the operation of Frank-Read sources in small grains such as nanocrystals is questioned.

Insitu X-ray deformation experiments showed that the broadening of the diffraction peak is reversible after unloading at room temperature⁵⁰, but not at lower temperatures⁵¹. The broadening of the peak width is determined by limitations in the spatial extent of the coherent scattering volumes and by the presence of inhomogeneous strain. Lattice dislocations can be a possible source for inhomogeneous strain because it is known that an increasing dislocation density in coarse grained metals contributes to peak broadening⁵². One interpretation of the observation of the reversibility of the peak broadening is that there is no dislocation network built up at room temperature. The irreversibility of the peak broadening after unloading at lower temperatures could indicate that there are residual dislocations after unloading. Furthermore it is observed that the broadening of the peak width can be reversed by heating the sample up.

The role of impurities on the dislocation activity in nc metals could not yet be directly observed. However, from experiments on nc Al thin films⁵³ it is known that a variation in the base pressure during sample production influences the impurity content in the samples. A significant change in the mechanical behavior is observed and attributed to the presence of impurities in the sample.

Stress assisted grain growth is a feature which can be observed in many experiments on pure nc metals. Grain coarsening has e.g. been observed in nanoindentation of Cu ⁵⁴, high pressure torsion of Ni ⁵⁵, compression of Ni and Cu ⁵⁶ or tension of Al ⁵³. As Mishin ³⁶ explains stress-assisted grain growth exists independently from the temperature. In experiments on nc Cu at cryogenic temperatures it was even found that the grain coarsening is more pronounced than at room temperature ⁵⁴. Grain coarsening in nc metals is a serious issue, because a degradation of the mechanical properties e.g. a reduction in strength would happen during testing or service ³⁶. According to Rupert ⁵⁷, stress assisted grain growth in nc materials is governed by coupled GB migration described above although the role of triple junctions is not so well understood. The observation of grain growth during deformation in many nc metals is one of the driving forces for the current research on the basic mechanisms of coupled GB migration.

From Gianola's experiments on Al thin films ⁵³ it is known that purer samples show more grain growth than impure ones produced under higher base pressure. This corresponds to the article of Koch and co-workers ⁵⁸ where the stabilization of the nc grain sizes is reviewed under the presence of solute additions. As the authors write, there are mainly two mechanisms to reduce grain growth: a kinetic approach by pinning of GBs or reducing their mobility and a thermodynamic approach by reducing the GB energy. In the first case mainly drag effects e.g. due to solutes or second phases come into play and in the second case solute segregation is the main driving force. So, impurities could contribute to both effects.

Impurities are inherently present in all experiments because of the exposure to an atmosphere during production or testing which leads to impurity contamination. The impurity content caused by the sample production can vary depending on the applied technique. For electrodeposited Ni, chemical analysis revealed predominantly metallic impurities coming from the anode material and S impurities because S is present as a bath additive in the production ⁵⁹. 3D atom probe of the same material has demonstrated that impurities are mostly present as solute atoms and only annealing showed a small tendency for segregation of impurities to GBs ⁵⁹. In case of ionic gas condensed Cu and magnetron sputtered Al impurities can be incorporated to the metal according to the conditions in the vacuum chamber used in both techniques. Gianola ⁵³ investigated the effects of a varying base pressure (see above) on nc Al thin films. He found out the impurity distribution is rather homogenous: No oxygen segregation at GBs was measured with EELS nor was there any "buried" O layers found using Auger depth profiling ⁶⁰.

1.2.2 Molecular dynamics simulations

MD simulations of fully three-dimensional nc metals have provided a lot of insight into deformation mechanisms and especially into details of dislocation/GB interactions in fcc metals

⁶¹⁻⁷². Based on these simulations, it is generally believed that the dislocations are nucleated from stress concentrations at GBs, propagate through the grain and are absorbed at the GBs. Atomistic simulations have also shown that the nucleation is usually accompanied by atomic shuffling and stress-assisted free volume migration ⁶⁷. Furthermore, it has been shown that dislocations which have been nucleated in GBs can be temporary pinned at GB ledges and their associated stress intensities during propagation ^{66, 70}. The time until a dislocation unpins is dependent on the simulation temperature. Instead of being pinned at stress concentrations it has also been observed that perfect screw dislocations circumvent these stress intensities by a mechanism called “cross-slip” ^{68, 72}. Cross-slip is found to be initiated by the stress signature of the local GB structure. With this, the dislocation propagates through the sample along a more favorable path and the dislocation can overcome potential pinning sites such as GB ledges or misfit regions using this mechanism. The dislocation propagation is a different process from dislocation nucleation however both nucleation and propagation are temperature dependent.

The described deformation mechanism for nc materials, based on GBs as sources and sinks for dislocations and strong interactions of local GB structures with propagating dislocations, gives a possible interpretation for the findings of the insitu X-ray-experiments in section 1.2.1: At room temperature, individual dislocations nucleate at GBs, travel through grains and are absorbed in neighboring GBs, which might also explain the lack of a dislocation network after deformation as it is observed for nc Ni ^{2, 47}. The residual dislocations which are mentioned in the case of the irreversible peak broadening after unloading at lower temperature could in fact be dislocations which are pinned at stress concentrations neighboring GB structure. The reversibility of the peak by heating the sample up can be interpreted by the temperature dependence of the pinning suggested by MD: The dislocations which are still pinned after unloading can unpin at higher temperature. Beside this detailed mechanism, MD simulations of fully three-dimensional nc samples also suggested the concept of the strongest size ⁷³. This means, a change in deformation mechanism is proposed on the basis of simulations on nc Cu samples ⁶². According to this concept, the deformation is characterized by dislocation plasticity in larger grains and more GB mediated process in smaller grains.

Although nc structures have contributed to many important results they have also disadvantages. It is e.g. “difficult to predict when and where dislocation activity will occur, which precludes a systematic study of the dislocation/GB interaction...” as Bitzek and co-workers write ⁶⁹. Alternative simulation structures are therefore used to study dislocation/GB interaction such as bicrystals ⁷⁴⁻⁸¹ or isolated grains from nc structures ⁷² especially for the study of dislocation propagation and cross-slip. The bicrystal simulation geometry neglects however important

details of polycrystals which can affect the resulting plasticity e.g. no triple junction lines are present which have a significant impact on the stability and on the slip accommodation in GBs.

The phenomenon of grain growth in nc metals has also been explored using MD simulations. It was shown that in nc Ni grains grow with a GB mobility which is linear in time⁸². It was further shown that the mobility of GBs is grain-size dependent and that more grain growth can be expected for smaller grains⁸². Additionally it was observed, that the growth process includes grain rotation and a reduction of GB energy. For simulations in columnar structures of Pd at a much higher temperature (800 K) it was seen that diffusion can be in concurrence with GB mobility and that triple junctions between grains are obstacles for the mobility of interfaces⁸³. In other simulations on nc Cu samples it was seen that grain growth is connected to dislocation emission into the grain⁸⁴. However, there is only little statistics on these events because only a few dislocations were emitted. The latter publications questioned, whether stress driven GB migration could be driving force for grain growth in nc metals. This has been verified by the work of Rupert and co-workers⁵⁷.

The MD simulations are not directly comparable to experiments. A first obvious difference is the time-scale issue. MD simulations can explore a time-frame of at most a few nanoseconds. For this reasons the observed processes and/or deformations have to happen in a very limited time-frame which leads to very high process and/or deformation rates. The second issue is, that MD simulations for nc metals are usually performed in monatomic systems. The effect of impurities on mechanical properties is hardly ever addressed. Only the role of impurities on the stabilization of grain growth is mentioned a few cases e.g. for dopants in GBs of fcc Cu⁸⁵⁻⁸⁸, or Fe in fcc Cu⁸⁹ or more recently Sb in nc Cu⁹⁰. The effect of these artificial particles or foreign atoms on the grain growth behavior is generally retardation. Publications on simulations of light elements in nc metals are very rare.

1.3 A method for oxygen impurities in aluminum

Impurities are present in nearly all pure metallic samples used in experiments at least as traces of foreign atoms. In a few cases, the impurity distribution and their effect have been explored^{59, 60}. For nc Al thin films it has been observed, that impurities can affect mechanical properties and/or the grain growth behavior⁵³. In contrast, MD simulations are performed in most cases on pure samples, only. Pure means here monatomic systems without any impurities and with no change in properties due to them. Especially simulations of dilute impurity concentrations of light elements are nearly not present in the literature maybe because of a lack of models for the description of impurities as Zhou⁹¹ assumes.

The MD simulation of polyatomic samples has to consider at least the difference in masses of the elements. Also the bonding nature between the elements is crucial and can be cumbersome if different bonding natures are present in one system. This is the case for dilute nonmetallic impurity concentrations in nc metals: The metallic matrix should be modeled using a metallic bonding and the model for the impurity-metal interactions has to account for the ionic nature of the bond due to the oxidation of matrix atoms around the impurities.

For the scenario of mixed interactions (metallic and ionic) only a few possible approaches exist. One example is bond order potentials which are used to model all kind of interactions (metallic, ionic or covalent) and can be used in simulations of mixed bonding conditions. It has been shown by Brenner⁹² that there is a relationship between bond order potentials and EAM potentials which are successfully used to model metals. The interaction in EAM potentials is determined by a pair function and an embedding function which determines the energy for inserting the atom into the local electron density at the atom's position. A modified embedded atom method (MEAM)⁹³⁻⁹⁵ is fitted for the interaction of many different impurities in metallic matrices. The method is based on embedded atom potentials with additional tensor treatment of the electron densities and a many-body "screening" procedure. In both methods, EAM and MEAM, the ionic nature of the systems is treated implicitly. To simulate ionic interactions e.g. in UO₂ for the research of nuclear materials, several potentials have been developed over the last decades^{96,97}. Usually they consist of sums of pair potentials e.g. a Buckingham potential⁹⁸ which is added to a Coulomb potential. The Coulomb part models the interactions between charges which are usually fixed in magnitude. Shell-model potentials^{99, 100} are developed to simulate ionic systems including polarization effects. In this shell-core approach, ions (with constant charges) are described as a mass less charged shell bound to a massive core (charge on spring). A drawback of the ionic methods mentioned above is that they are not flexible enough to handle the changing ionicity in case of dilute impurities in nc metals. Similar shell model potentials with fixed charges for each ion type can also be found for Al-O systems¹⁰¹. A large improvement can be found in the work of Streitz and Mintmire¹⁰², which fitted a potential for the metal/oxide interfaces or surfaces. This approach includes variable charges and was published for O in Al. The charges depend on the environment of each atom and are derived from an electronegativity equalization scheme. Using the feature of variable charges, the potential can be used to simulate the local change in bonding nature across the metallic/ionic interface and can calculate the energy, force and stress contributions, which come from the electrostatic interaction. Later the two approaches of bond orders and charge equilibration were merged in a new concept by Yasukawa^{103 104} which is called reactive force field (ReaxFF)^{105, 106}: The study of systems with metal/ionic and metal/covalent interfaces is then possible. A recent simulation technique for ionic systems is proposed by Zhou: the embedded ion method

(EIM) ⁹¹. It includes the charge transfer features with environmental dependence of the ionic bonding without solving the charges explicitly and was published for La-Br systems. This model promises access to the modeling of nonstoichiometric ionic systems and can be a future candidate for the simulation of impurities.

The method developed in this work is based on Streitz and Mintmire's approach which has successfully been used in many different contexts. Its description and a few examples can be found in section 2.3. As already mentioned Streitz and Mintmire's potential was developed for metal/oxide interfaces or surfaces, therefore modifications of the EAM potentials are necessary for the simulation of dilute O impurities in Al or nc Al. Additionally, an adaptation of the charge update procedure should increase the computational performance in the scenario of dilute O impurities in Al. Studying the effect of O in Al has several reasons: First the Streitz and Mintmire's potential is published for this system; second, a lot of experience on pure nc Al simulations is present in the Materials Science and Simulation group¹⁰⁷ which can be used for comparison and third, Gianola investigated nc Al thin films and showed interesting results for the effect of O impurities.

In the rest of this thesis the development of the method and its application are described and discussed. In the next chapter, existing methods are summarized: a glance at ab initio simulations and a detailed explanation of MD and the potential of Streitz and Mintmire will be given. Then, the major results, which are the development of the new simulation method and its applications, will be elaborated. After this, the method will be discussed. At the very end conclusions and an outlook will be provided.

2 Simulation methods

2.1 Ab initio

The method developed during this thesis is an addition to classical molecular dynamics. Ab initio calculations are used to produce reference structures for the fitting of empirical potentials. Therefore a brief introduction to ab initio, primarily density functional theory, is given here.

A calculation which is “ab initio” or “from first principle” relies on basic and established laws of nature without assuming empirical data. Hence, ab initio calculations in atomistic simulations investigate the quantum state of molecules, crystalline solids or other collections of atoms by solving the corresponding Schrödinger equation $H\psi = E\psi$ using basic laws, natural constants and assumptions. The motion and interactions of electrons and nuclei of a physical system are expressed by a Hamilton operator H which determines the temporal evolution of the state represented by the wave-function ψ and corresponding energy E . The Hamilton operator is a collection of terms which stand for kinetic and potential energies of nuclei and electrons. The Schrödinger equation is an Eigenvalue problem for the given Hamilton operator with Eigenstates (wave-functions ψ) and energies E as corresponding Eigenvalues. For the ground state problems considered here it is sufficient to solve the time-independent Schrödinger equation.

The exact solution of the many-body Schrödinger equation is not known even for the time-independent case. For this reason, further assumptions are made and numerical methods are developed to approximate its solution. The Born-Oppenheimer (also known as adiabatic) approximation decouples the nuclear and electronic motion due to large differences in mass which gives a clear separation of time-scales. Using Born-Oppenheimer, the electronic problem can be solved with the nuclear positions as parameters. As a result one obtains a Born-Oppenheimer energy surface which is determined by the electronic structure. Solving the electronic problem is the key issue in ab initio calculations. Different classes of methods exist, e.g. wave-function approaches based on the Hartree-Fock method. Another approach focuses more on the electron density ρ , where $\rho(r) = N \int \int \psi^*(r, \dots, r_N) \psi(r, \dots, r_N) dr_2 \cdots dr_N$. This approach is called “density functional theory” or short DFT and is very common in many fields. It will be explained in the section 2.1.1 as it is used in this work.

The electronic structure can be used to determine forces in an atomic configuration by applying the Hellmann-Feynman theorem. Nuclei can be moved to energetically more favorable positions. Consequently, the atomic structure can be optimized by moving nuclei to a

configuration where the forces between them vanish. This configuration is at least a stationary point of the Born-Oppenheimer energy surface. Thus the initial configuration of the system has to be sophisticated enough to find a minimum of interest. Alternatively one can use sampling techniques such as ab initio molecular dynamics to find energetically more favorable configurations. The Car-Parrinello method¹⁰⁸ is one popular example.

2.1.1 Density functional theory

The concept of DFT is based on two famous theorems by Hohenberg and Kohn¹⁰⁹. The first one claims that there exists an one-to-one mapping between the ground-state electron density ρ_0 and the ground-state wave-function ψ_0 of a many-particle system. The second one states that there exists a universal energy functional $E[\rho]$, whose minimum corresponds to the exact ground-state energy E_0 . The second Hohenberg-Kohn Theorem proves the existence of the functional $E[\rho]$ and a variation principle for the case of the known functional. What is missing is the exact form of the functionals. Many approximate functionals have been proposed. The accuracy, especially for the kinetic energy is for applications often not sufficient.

Kohn and Sham¹¹⁰ overcome this latter difficulty by recasting the problem via a variational approach into a Schrödinger-like problem. They described the system as a set of non-interacting electrons moving within an effective potential. For this problem it is possible to find the kinetic energy contributions to the total energy as they are exactly known from Hartree-Fock theory. The effective potential represents the external potential and the effects of the Coulomb interactions between the electrons, e.g. the exchange and the correlation interactions. The electronic interaction, the so-called exchange-correlation remains difficult and is approximated. Many empirical approximations for the exchange-correlation functionals have been suggested by now. However this is still a major source of errors as it is not possible to systematically improve this exchange-correlation functional. Different classes of approximate exchange-correlation functionals are used: local density approximation (LDA) or generalized gradient approximation (GGA) or hybrid functionals. In LDA the exchange-correlation depends solely on the electronic density at each point in space whereas in GGA the density and its gradient are taken into account. Hybrid functionals mix the exact Hartree-Fock exchange with LDA or GGA approximants. Expressions for the different exchange correlation functionals can be found in textbooks, e.g.^{111, 112}.

The description of the wave-functions, which are used to compute the electron density, is essential. Their choices together with the selection of the exchange-correlation functional and

the treatment of the core electrons determine the accuracy and efficiency of the calculations. In periodic systems e.g. in crystalline solids, the use of plane-waves is common as it leads to simple formulations of Kohn-Sham equations. The plane-wave representation of a one electron wave-function is given by Bloch's theorem, which states that a wave-function of an electron in a periodic potential can be written as a product of a lattice periodic part and a wavelike part. The wave-function is then represented as sum of plane-waves where the wave vector k can be related to the energy. An infinite number of plane-waves are necessary for an exact calculation. However, not all the plane-waves are of the same importance in the description of the kinetic energy. Therefore the number of plane-waves can be reduced by setting an energy cutoff, which determines the accuracy of the calculation. Plane-waves are weak in describing wave-functions with large curvature. In this case a large number of plane-waves is necessary. Therefore the core region, where the wave-function oscillates a lot and which is relatively unaffected by the chemical environment of an atom, can be modeled by using a pseudopotential approximation. The strong Coulomb potential and core electrons are replaced by an effective pseudopotential which is much weaker. The rapidly oscillating wave-functions in the core region are represented by pseudo-wave functions which vary smoothly in the core region. A further development of the pseudopotential concept is Blöchl's projector augmented wave method ¹¹³.

Using pseudopotentials, only the valence region is modeled as plane-waves. In case of real-space integration over infinitely extended periodic systems, a replacement by an integral in reciprocal-space over the confined first Brillouin zone can be found. In theory, still an infinite number of points in reciprocal space, i.e. k-points, are necessary for the calculation, however in practice, a finite number of k-points, i.e. points on a mesh, with a given distribution is normally sufficient. Often, the point group symmetry of atomic configurations is used to restrict the set of k-points to a smaller subset in the interest of computational efficiency. A plane-wave DFT calculation is characterized by the selection of an exchange-correlation functional, the choice of a pseudopotential, the number of k-points, their distribution and the energy cutoff used.

In case of systems with limited periodicity or symmetry (e.g. if there are defects) the precision and the efficiency of the plane-wave approach can be reduced if the number of k-points and the energy cutoff is not increased enough. The computational efficiency decreases significantly if the point group symmetries can not be exploit anymore.

During this work the VASP code ¹¹⁴⁻¹¹⁷ is used with projector augmented wave potentials ^{113, 118} using the PBE functional ^{119, 120}.

2.1.2 Limitations of ab initio methods

Ab initio methods are generally very limited in the number of atoms which can be simulated however they offer a more accurate description of the many-body system, e.g. a more accurate description of materials cohesion than empirical models. Systems are of the order of ten to one thousand atoms depending on the method and/or the accuracy.

DFT is useful to model groundstate properties or properties of a system in thermal equilibrium. Ab initio methods include approximations. In case of DFT this leads to errors in the calculated properties which are not predictable. The accuracy of a DFT calculation is not systematically improvable.

2.2 Molecular dynamics

2.2.1 Basics

Empirical molecular dynamics (MD) solves the classical many-body problem of N interacting particles. Systems, which can be simulated, range from atomic or molecular systems such as gases, liquids, condensed matter to non-atomic systems such as traffic scenarios with cars as entities. Textbooks are written on the method and on specific application dependent topics. References ¹²¹⁻¹²³ show a small selection which has been used during the PhD work. In what follows particles represent atoms since this is how the MD method is used here.

MD is an iterative method, which derives forces in Newton's equation of motion (equation 1) from an empirical potential for a static configuration of atoms and integrates the left hand side for a small time increment Δt using the previously calculated forces and numerical techniques.

$$m_i \frac{d^2 \vec{r}_i}{dt^2} = \vec{F}_i = - \frac{\partial V_{tot}}{\partial \vec{r}_i} \quad (1.)$$

The interaction potential is then characterized by a multi-atom energy function V_{tot} . Some important examples are described in sub-section 2.2.2. The knowledge on the positions and the velocities of the previous time-steps is used in the integration. As a result of the integration new positions and velocities are obtained. The new atomic configuration is used to calculate properties and to obtain new forces. Repeating the iteration of the update of forces and the integration of Newton's equation of motion (equation 1) many times gives trajectories for the

atomic motion. To make the method complete, MD requires a start configuration which consists of the atomic positions and velocities. The basic algorithm looks as Figure 2.1.

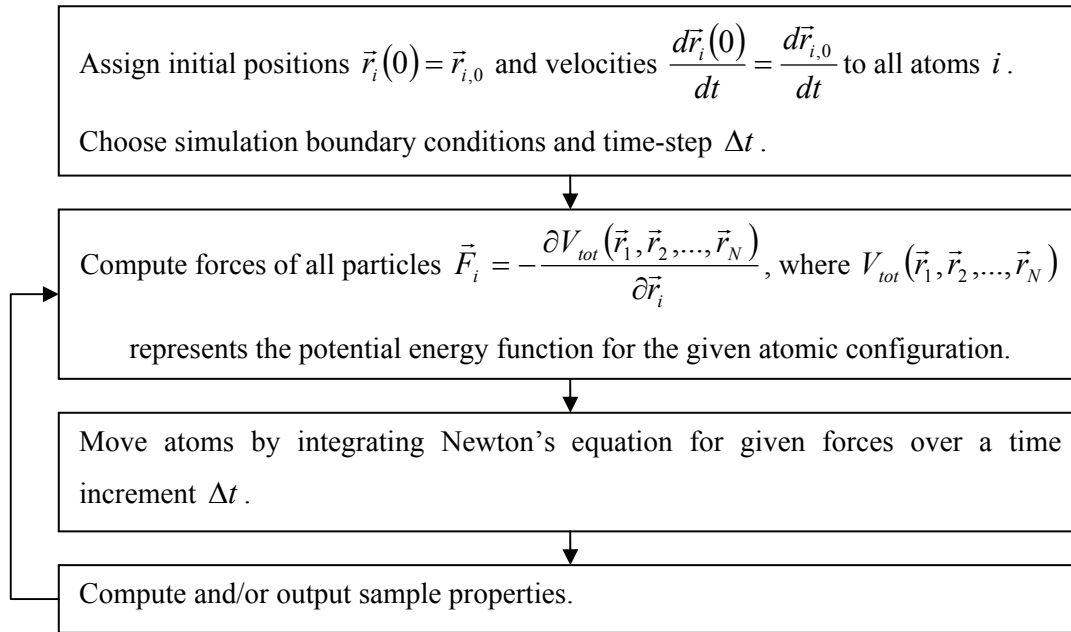


Figure 2.1 MD algorithm

Considering Figure 2.1, several explanations can be made: The box at the top of Figure 2.1 mentions the initial positions and velocities for all the atoms in the system. The initial particle distribution should be compatible with the simulation geometry of interest and determines the initial volume of the simulation sample. The initial velocities can be assigned to the atoms according to the initial temperature. A velocity distribution, in this work an uniform distribution, is used to assign each atom a random velocity. The equipartition theorem, which relates the system temperature with average system energies, can be used to determine the instantaneous temperature from the kinetic energy. A rescale of the atomic velocities, i.e. multiplying atomic velocities by a factor $\sqrt{T_{desired} / T_{actual}}$ to get the desired temperature ($T_{desired}$), can be used to match the desired temperature.

Furthermore simulation boundary conditions are mentioned: They can either be of geometrical or thermodynamical nature. The most important geometrical boundary treatment is the periodic boundary condition because a computer can simulate a limited amount of atoms only. Consequently, the size of the simulation samples is limited and the surface to volume ratio for such samples is rather high. Therefore surface effects can dominate simulations. To avoid this, the sample is periodically repeated in all directions (Figure 2.2). Under these so-called “periodic boundary conditions” a sample has no more free surface and represents a bulk-like simulations

specimen. If free surfaces are desired in the simulation it is possible to have periodic boundary conditions only in one or two dimensions. This leads to either bar or slab geometries. It is also possible to have not periodic boundary conditions at all. The limited sample sizes can also be enlarged by the usage of parallel computers. Different approaches are known for efficient parallel MD simulations ¹²⁴, e.g. domain or force decomposition.

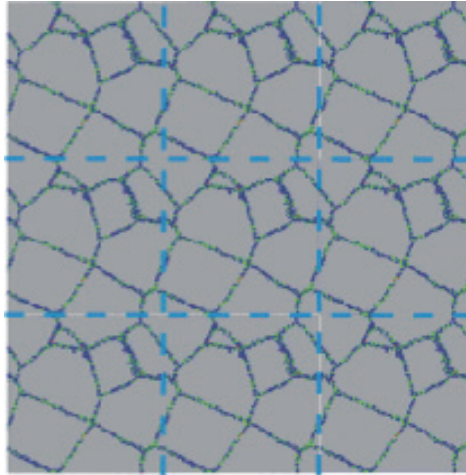


Figure 2.2 Periodic boundary conditions. The original simulation box (in the middle) is replicated in all the three (here two) dimensions. The GB network fulfills the periodicity. Taken from Ref. ¹²⁵.

The time-step, which can be chosen, has to be small enough to guarantee numerical stability and to be able to resolve the relevant processes in the considered system. In atomic systems, these are atomic vibrations. Therefore time-steps are usually of the order of one femtosecond (i.e. 10^{-15} s) for simulations at room temperature. If it is assumed that the execution of one entire MD step takes in the order of a second on an average computer, it is obvious that at most the nanosecond time-scale is accessible in a reasonable amount of simulation time, which is a major limitation of molecular dynamics simulation. The most common solution to access longer time-scales and with this access also less frequent events is the use of more sophisticated sampling techniques such as accelerated MD ^{126, 127}. However these methods are only efficiently applicable in systems with rather simple transitions between a limited number of states.

The second box in Figure 2.1 shows the force evaluation for each particle which is done by numerical evaluation of the negative gradient of the interaction potential at each particles position. The quality of the interatomic potential determines the accuracy of MD simulation considerably (see section 2.2.2). The evaluation of the forces can be a bottleneck for the computational efficiency if too many interactions have to be evaluated. As many interactions rapidly decay to zero with increasing distance between the atoms, force evaluation can be cut-off at a given distance: the so-called cutoff radius. So a restriction of the interactions to smaller

subsets of neighboring atoms can be made. The gain in efficiency by the introduction cutoff distances can be enhanced by using either a neighbor list or a link-cell list. In the third box in Figure 2.1, the integration scheme for Newton's equation of motion (equation 1) is mentioned. As already written, numerical methods are used to integrate the second order differential equation, for the given time increment Δt . Integration schemes are e.g. the Verlet integrator¹²⁸ or the Gear integrator also known as "Backward Differentiation Formula" BDF¹²⁹. Here, these integration schemes are used in a predictor corrector notation. As a result new positions and velocities are obtained. The instantaneous temperature of the simulation system can be modified by rescaling the velocities using the equipartition theorem for the kinetic energy.

The box at the bottom in Figure 2.1 mentions the computation and/or output of sample properties. These can simply be the atomic positions to follow trajectories of the atomic motion or properties which have to be calculated such as energies, stresses, atomic coordination or the local crystallinity class. The computation of some of these properties is explained in sub-section 2.2.3 and 2.2.4.

The iteration over the force computations and integration of Newton's equation of motion allows for sampling of ensembles. For energy conserving forces these ensembles are micro canonical (NVE = constant number of particles N , constant volume V and constant total energy E). However some effort has been spent to be able to sample other ensembles such as the canonical NVT, i.e. constant temperatures T or the isobaric NPE or NPT ensemble (constant pressure P). In this work velocity rescaling is applied to maintain the desired temperature and Parinello-Rahman method (see section 2.2.3) is used for pressure or stress constraints.

2.2.2 Interaction potentials

The interaction potentials V_{tot} which are empirical substitutes for the energy surface given by the adiabatic approximation of ab initio calculations are a key element of MD simulations. The quantum nature e.g. of the neglected electrons has to be considered in the description of the potential which is usually done by the form of its empirical description and/or by the choice of parameters. One or more equations represent usually the assumptions of the physical model using a set of adjustable parameters. These parameters have to be fitted to reproduce materials properties of interests by comparing to experiments or ab initio data. In the interest of energy conservation and efficiency the interactions should smoothly vanish at the defined cutoff distance which is of as short range as possible.

Depending on the approach the potential energy function can be modeled as a sum of sums which describe two-body, three-body, four-body ... interactions in an atomic system to which an atomic energy ($V_1(r_i)$) may be added.

$$V = \sum_i V_1(r_i) + \sum_i \sum_j V_2(r_i, r_j) + \sum_i \sum_j \sum_k V_3(r_i, r_j, r_k) + \dots \quad (2.)$$

where V is the total potential energy of the system. The difference between the potential energy of an atom (V/N) and its atomic energy ($V_1(r_i)$) is its cohesive energy.

In the closed shell system (e.g. for noble gases) without much influence of the electrons on bonding a two-body potential is sufficient to describe the interactions. Normally only the long-range Van der Waals force and short-range repulsive forces due to Pauli repulsion are modeled. A well-known two body potentials is the Lennard-Jones potential ¹³⁰:

$$V = \sum_i \sum_{j>i} 4\varepsilon \left[\left(\frac{\sigma}{r_{ij}} \right)^{12} - \left(\frac{\sigma}{r_{ij}} \right)^6 \right] \quad (3.)$$

For this potential, the first term represents the short range repulsion and the second term describes the long range attraction. The parameter ε represents the depth of the potential well and σ describes the finite distance at which the potential is zero. Parameters are known for more materials than just noble gases. However, the Lennard-Jones potential can not model the directional nature of metallic bonding ¹³¹. In fact, the Lennard-Jones potential is not capable to correctly reproduce the Cauchy relationship of the elastic constants, vacancy formation energies or surface relaxation ¹³² for a cubic system because of the simple pair potential interactions ^{131, 132}.

In case of the metallic bonding the interaction model must combine a screened ion-ion type interaction (pair term) and an electronic band-energy term. This band term can be represented by a square root of bond overlap integrals between neighboring atoms. This approach is usually called “2nd moment tight binding method” ^{133, 134}. In 1983, Daw and Baskes ¹³⁵ introduced a more general type of potential which also solves the problem of the elastic constants in cubic systems. The theoretical foundation of the method has its origin in DFT. This model is called “embedded atom model” (short EAM) and has got the following form

$$V = \frac{1}{2} \sum_i \sum_j \varphi(r_{ij}) + \sum_i F(\rho_i) \quad (4.)$$

The function φ is a pair potential for the short range interaction between atom i and j , ρ_i represents the local electron density at atom i and is constructed from contributions of surrounding atoms $\rho_i = \sum_j \rho(r_{ij})$ and F is the embedding function which represents the change in energy of inserting atom i into the electron density at its position given by ρ_i . In the case of the 2nd moment tight binding model, e.g. the Finnis-Sinclair potential, F is simply a negative square root function. With the additions of $F(\rho)$ a non-zero Cauchy pressure is possible.

For the simulation of monometallic systems, the functions φ , ρ and F have to be described. They are defined in an analytical description based on parameters or by a spline fit which reproduces the properties of interest. EAM potentials for a lot of materials can be found in the literature. In case of binary systems the potential has obviously to be extended from three to seven functions: three functions for the pair interaction, two electron density functions and two embedding functions¹³⁶.

2.2.3 Additional simulation techniques

Molecular statics

The method of molecular statics (MS) can be used to relax the atomic positions to a local minimum of the potential energy. Atoms without initial velocities are displaced according to the forces which act on them at the given positions. Integrating Newtons equations of motion (equation 1) in an iterative way analogously to MD simulations leads to increasing atomic velocities. These velocities are from time to time removed in the simulation which is called “quenching”. This is done according to a quench condition. In the existing MS code, a local and a global quenching condition are implemented. The global condition, i.e. simultaneous removal of all the velocities in the system, is fulfilled when a maximum in kinetic energy is reached. The local condition, where the velocity of a single atom is removed, is true if the dot product between the atoms velocity and acceleration vectors is negative.

The size of the integration step controls the displacement of the atoms and with this the convergence rate of the method. In addition to the final relaxed structure one obtains a series of intermediate configurations which are connected through a causal series of physical events.

With this, it is possible to follow the processes of the relaxation. If a quench condition would be applied in every step a steepest decent minimization of the potential energy is obtained.

Parrinello-Rahman method

In some simulations it is required that system shape and/or size can adapt to the applied conditions such as temperature or stress. The key method for these simulations is the “Parrinello-Rahman” method^{137, 138} which is used to maintain isobaric simulation conditions. For the application of the method the periodic system with box vectors \vec{b}^x , \vec{b}^y and \vec{b}^z has to be transferred to internal coordinates (ξ_i, η_i, ζ_i) . The position vector \vec{r}_i is then equal to

$$\vec{r}_i = \xi_i \vec{b}^x + \eta_i \vec{b}^y + \zeta_i \vec{b}^z \quad (5.)$$

In the internal representation of the system the coordinates have to fulfill $-0.5 < \xi_i, \eta_i, \zeta_i < 0.5$. Parrinello and Rahman introduced a Lagrangian which contains the internal coordinates, the interatomic potential, the external stress state as well as a term which determines the motion of the MD box. This Lagrangian is solved for the internal coordinates, which gives the equations of motion and analogously the box coordinates which gives the change in box volume or shape.

An uniaxial deformation of rectangular MD sample at a given strain-rate can be done by straining one box vector and using the internal coordinates given by equation 5. To adapt the box length in the directions perpendicular to the tensile direction, the Parrinello-Rahman method is used to obtain a zero stress-state in these directions. The stress in the deformed direction can be recorded to plot stress-strain data.

Static atoms

For some purposes, e.g. the relaxation of a structure with a fixed interstitial at a given site or to simulate free surfaces which maintain the simulation geometry, it is useful to freeze the motion of some atoms in. The frozen atoms are then called static atoms. Making the atoms static is achieved by not assigning them an initial velocity and by removing the force acting on the corresponding atom in each time-step of the MD scheme. Although static atoms do not move, they interact with neighboring atoms. The calculation of global system properties in a system with static and unstatic atoms has to account for the fact that the number of degree of freedoms is reduced. So for global properties such as kinetic energy, temperature or global stresses, only mobile atoms have to be taken into account.

Instead of freezing the motion of atoms completely it is also possible to freeze only some degrees of freedom of atoms. For example, an atom at the surface can be allowed to move only parallel to the surface but not perpendicular to it. Also here, the calculation of system properties has to be adjusted to the number of global degrees of freedom.

2.2.4 Atomic properties and visualization

Atomic coordination

The coordination of an atom can be obtained by counting neighboring atoms which are closer than a predefined distance. This distance corresponds to a value between the first and second nearest neighbor spacing in the perfect lattice. This measure can identify additional atoms in the lattice, e.g. interstitials, or high energetic distortions in GBs. However the coordination of a lot of atoms in GB regions and atoms in stacking faults (i.e. hcp atoms) are not different from atoms in the regular fcc crystal because it is twelve in all cases. So, identifications of GB regions or dislocations is difficult using atomic coordinations.

Local crystalline order

This method examines the type of local crystallinity for each atom using the topological analysis developed by Honeycutt and Andersen¹³⁹. According to the method the local environment of a pair of atoms is characterized by four indices i, j, k and l . The index i denotes the bond relation of two atoms. Two atoms are bonded if $i = 1$ and not bonded if $i = 2$. Index j indicates the number of common nearest neighbors between the two bonding atoms. Index k provides the number of bonds among the common nearest neighbor atoms. The last index l indicates the number of bonds in the longest continuous path that goes through the common neighbors. This procedure provides a distinction between fcc and hcp structures, taking only the nearest-neighbor pairs into account. For example, an arbitrary atom in the perfect fcc structure forms only 1421-type quadru-pairs with its twelve nearest-neighbor atoms, while in the case of the hcp lattice six 1421 and six 1422 quadru-pairs are found (Figure 2.3).

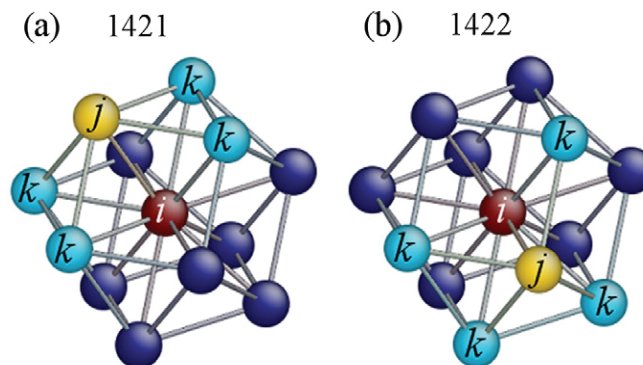


Figure 2.3: Examples of the 1421 (a) and the 1422 (b) quadru-pairs. Image taken from Ref.¹⁴⁰

Using this analysis, one can assign each atom a class of local crystallinity and color them accordingly. The standard color-code used here is grey for fcc, red for hcp, green for other 12-coordinated atoms and blue for non-12-coordinated atoms. This coloring is useful to identify defects in visual inspection of simulation data. The perfect fcc lattice appears as grey atoms whereas GBs are usually mixtures of blue and green atom with some randomly distributed red (hcp) atoms. For dislocations, the core atoms in the leading and the trailing partial are colored blue and green, the stacking fault between leading and trailing is red (see Figure 2.4).

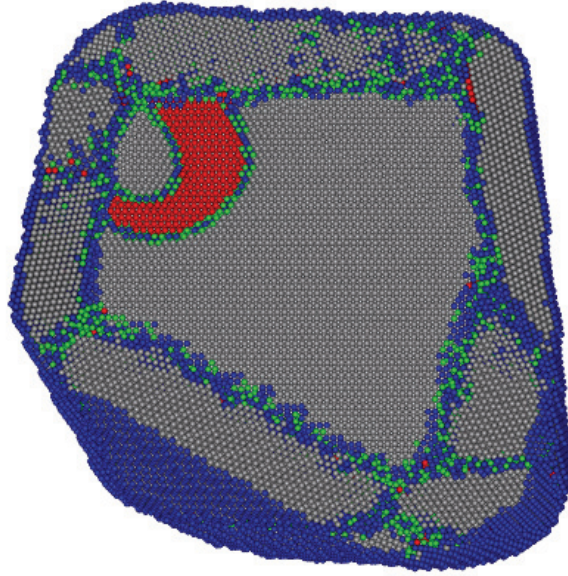


Figure 2.4 A grain with neighboring atoms containing a perfect dislocation. Using the color-code in the text one sees the fcc grain interior (grey), the GB consisting largely of non-12-coordinated (blue) and other 12-coordinated atoms (green) as well as the dislocation with the hcp atoms (red) in the stacking fault.

Pressure and stress calculations

For the investigation of the global pressure the expression 6 found in the MD textbook¹²² can be used.

$$P = \left\langle \frac{1}{3V} \sum_i \left(m\vec{v}_i^2 + \frac{1}{2} \sum_{\langle j \rangle} \vec{F}(r_{ij}) \cdot \vec{r}_{ij} \right) \right\rangle. \quad (6.)$$

In equation 6 the summation is over all atoms in the volume V which is usually the simulation box volume. $\langle \cdot \rangle$ represents an ensemble average or a long enough time average. In the thermodynamic limit of large enough volumes V , the expression represents the true bulk

homogeneous hydrostatic pressure. Analogously, an expression for the local pressure (equation 7) can be obtained by changing the global volume V into a representative mean atomic volume Ω ($\Omega = V / N$ where N is the number of atoms in the system).

$$P_i = \left\langle \frac{1}{3\Omega} \left(m\bar{v}_i^2 + \frac{1}{2} \sum_{\langle j \rangle} \vec{F}(r_{ij}) \cdot \vec{r}_{ij} \right) \right\rangle. \quad (7.)$$

Instead of computing pressures it is also possible to compute the stress tensor σ^{st} for a given reference coordinate-system where s and t represent the coordinate directions (e.g. x, y and z).

$$\sigma_i^{st} = \left\langle \frac{1}{3\Omega} \left(mv_i^s v_i^t + \frac{1}{2} \sum_{\langle j \rangle} F(r_{ij}) r_{ij}^s r_{ij}^t \right) \right\rangle. \quad (8.)$$

In equation 8, it is important to note that $F(r_{ij})$ is the scalar force magnitude which depends on the interatomic distance r_{ij} and is also used to compute the force vector \vec{F} by multiplying each directional position difference r_{ij}^s to it.

Equations 6 to 8 are valid for the central face model only. It is known that the volumetric partition of the pressure in equation 7 lacks of momentum conservation across its corresponding surfaces¹⁴¹. This can lead to non-negligible artifacts such as oscillatory behavior or strongly inhomogeneous behavior when one goes to small volumes, e.g. atomic volumes in equations 7 and 8. However these atomic calculations can still be used to estimate the spatial pressure or stress variation. The alternative, is to use another scheme¹⁴² which can represent the local pressure (or stress) more accurately via

$$P_\Omega = \frac{1}{3\Omega} \left\langle \sum_i \left(m\bar{v}_i^2 \Lambda_i + \frac{1}{2} \sum_{\langle j \rangle} \vec{F}(r_{ij}) \cdot \vec{r}_{ij} l_{ij} \right) \right\rangle \quad (9.)$$

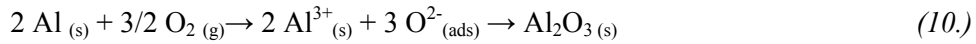
In equation 9, Ω represents a volume of a region of interest, Λ_i is unity if atom i is within the volume element and zero otherwise, and l_{ij} is the fraction of the length of the bond between atoms i and j that lies within the volume element Ω . This method can now rigorously satisfy conservation of linear moments for a chosen volume, e.g. a sphere centered at each atom (atomic pressure equals pressure of the local sphere). The disadvantage of the present method is

that the local atomic stress/pressure does not necessarily have to sum up to the global stress/pressure. This follows from the partitioning of the global volume into volume elements which is non-volume conservative. In this case this is not required. Additionally, problems for the convergence of the local pressure to the correct thermodynamic grain pressure exist. These two weaknesses are not present in the previous method described by equations 7 and 8. A comparison of the methods in use can be found in ¹⁴³.

In this work the methods described by equations 6 to 8 are used to visualize simulation data. It accentuates the presence of crystalline defects such as impurities, dislocations or grain-boundaries. As it is explained above the magnitudes of stress should generally be understood as qualitative and not as quantitative measure.

2.3 Molecular dynamics with charged atoms

If different metallic and nonmetallic atoms appear in the same system oxidation happens and ionic bonds are formed which means that electrons migrate from the electron donating metal to the electron accepting nonmetal. If the stoichiometric ratio of metallic to nonmetallic atoms is optimal both elements are in the end in the closed shell configuration. Alumina in the corundum structure consists for example of forty atomic percents three times positively (+3e) charged Al ions and sixty atomic percents twice negatively (-2e) charged O ions.



If the mixture of atomic species is non-stoichiometric or inhomogeneous oxidation and with this the charge transfer will happen only in a limited extend. Partial atomic charges can occur which depend on the local environment of each atom. Only a few methods can determine and simulate such variable charges within the framework of MD (see introduction). Streit and Mintmire's method ¹⁰² is one successful approach. It is developed to simulate metal-oxide interfaces and the underlying assumption is that the atomic charges are not unique in the bulk metal, in a metal-oxide or in the interface. Variable charges in the context of Streit and Mintmire's work means that atomic charges are updated according to environment of each atom during an MD simulation to obtain the charge transfer between anions and cations. In what follows Streit and Mintmire's approach for variable charges is explained in detail.

2.3.1 Streit and Mintmire's potential

Streit and Mintmire's method assumes a classical electrostatic energy E_{es} for a set of interacting atoms with atomic charges q_i and positions r_i which is represented as a sum of atomic energies E_i , and the electrostatic interaction energies $V_{ij}(r_{ij}; q_i, q_j)$ between all pairs of atoms,

$$E_{es} = \sum_{i=1}^N E_i(q_i) + \frac{1}{2} \sum_{i \neq j}^N V_{ij}(r_{ij}; q_i, q_j) \quad (11.)$$

The atomic energy $E_i(q_i)$ is given by the Taylor series expansion of the neutral atom i 's energy where the first derivative is traditionally denoted as the electronegativity χ_i^0 ^{144, 145} and the second derivative is called atomic hardness¹⁴⁵ or self-Coulomb repulsion¹⁴⁶ J_i^0 :

$$E_i(q_i) = E_i(0) + E_i'(0)q_i + \frac{1}{2} E_i''(0)q_i^2 = E_i(0) + \chi_i^0 q_i + \frac{1}{2} J_i^0 q_i^2. \quad (12.)$$

The classical electrostatic interaction energy $V_{ij}(r_{ij}; q_i, q_j)$ between the pairs of atoms can be written as

$$V_{ij}(r_{ij}; q_i, q_j) = \iint d^3 r_1 d^3 r_2 \frac{\rho_i(r_1; q_i) \rho_j(r_2; q_j)}{r_{12}}, \quad (13.)$$

where $\rho_j(r; q_j)$ stands for the charge density around atom i at r with the total charge q_i . There are several possible charge distributions such as point charges or spherically symmetric Slater-type orbitals. Streit and Mintmire are using the latter type according to the suggestion of Rappe and Goddard¹⁴⁶. The atomic charge density looks like

$$\rho_j(r; q_j) = Z_i \delta(r - r_i) + (q_i - Z_i) f_i(r - r_i) \quad (14.)$$

and is linear in atomic charge q_i . The first term represents the effective core charge as a point charge, where $0 < Z_i < Z_i$, with Z_i the total nuclear charge of the atom. The second term describes the valence charge distribution where f_i represents its spatial extend. Streit and

Mintmire use for “mathematical convenience” a simple exponential which can be constructed from Slater 1s orbitals. $f_i(|r - r_i|) = \frac{\xi_i^3}{\pi} \exp(-2\xi_i|r - r_i|)$. However Streit and Mintmire point out that “more complicated (and perhaps more realistic) distribution functions” could be used for the formulation of the model.

If one inserts the atomic charge densities into the formula for the electrostatic interaction one obtains

$$E_{es} = \sum_{i=1}^N E_i(q_i) + \frac{1}{2} \sum_{i \neq j}^N \{q_i q_j [f_i | f_j] + q_i Z_j ([j | f_i] - [f_i | f_j]) + q_i Z_j ([j | f_i] - [f_i | f_j])\} \quad (15.)$$

If the terms are summarized according to the multiplicity of the charges q_i one obtains

$$E_{es} = E_0 + \sum_{i=1}^N q_i \chi_i + \frac{1}{2} \sum_{i,j=1}^N q_i q_j V_{ij}, \quad (16.)$$

where

$$E_0 = \sum_{i=1}^N E_i(0) + \frac{1}{2} \sum_{i \neq j}^N Z_i Z_j ([f_i | f_j] - [j | f_i] - [i | f_j] + 1/r_{ij}),$$

$$\chi_i = \chi_i^0 + \sum_{j=1}^N Z_j ([j | f_i] - [f_i | f_j]), \quad (17.)$$

$$V_{ij} = J_i^0 \delta_{ij} + [f_i | f_j].$$

The notation $[\rho_a | \rho_b]$ and $[a | \rho_b]$ stand for the Coulomb interaction integral between charge densities ρ_a and ρ_b and the nuclear-attraction integral, respectively. Using Roothaan’s calculations¹⁴⁷ yields the following results for the 1s charge density:

$$\begin{aligned}
[\rho_a | \rho_b] &= \iint d^3 r_1 d^3 r_2 \frac{\rho_a(r_1)\rho_b(r_2)}{r_{12}} = \frac{1}{r_{ab}} \left[1 - (1 - \kappa)^2 \left\{ \frac{1}{4}(2 + \kappa) + \frac{1}{4}\rho_a \right\} \right. \\
&\quad \left. \exp(-2\rho_a) - (1 + \kappa)^2 \left\{ \frac{1}{4}(2 - \kappa) + \frac{1}{4}\rho_b \right\} \exp(-2\rho_b) \right] \quad (18.) \\
[a | \rho_b] &= \int d^3 r \frac{\rho_a(r)}{|r - r_a|} = \frac{1}{r_{ab}} \{ 1 - (1 + \rho_b) \exp(-2\rho_b) \},
\end{aligned}$$

where $\kappa = (\xi_a^2 + \xi_b^2) / (\xi_a^2 - \xi_b^2)$.

E_o in equations 16 and 17 is independent of atomic charges q_i . E_o depends on the nuclear coordinates only and behaves as a sum of pair potentials. The expression for E_o as well as the others derived so far are based on classical electrostatics only and can not be used for the description of electronic contribution to bonding. Streit and Mintmire propose to implicitly incorporate the E_o term in the non-electrostatic potential (i.e. an EAM potential) which is described further down and to exclude it from the electrostatic interaction.

Using equations 18 derived from Roothaan¹⁴⁷ it is obvious that the leading term is of order $1/r_{ij}$. Consequently one has to take long-range interactions into account and one has to use an appropriate numerical scheme to achieve a reasonable computational efficiency. Streit and Mintmire have chosen Ewald summation as a long-range method.

To determine the atomic charges q_i , the classical electrostatic energy E_{es} is minimized under the constraint of global charge neutrality since a well-defined minimum should exist for “well-behaved” parameters J_i^0 and functions $f_i(r)$. This approach is algebraically equivalent to the equalization of the electronegativity which means that electrostatic chemical potentials μ_i can be introduced which are identical to the global chemical potential μ and it holds

$$\mu = \mu_i \equiv \frac{\partial E_{es}}{\partial q_i}. \quad (19.)$$

If equation 19 is plugged into expression 16 and one rearranges the expression the following can be obtained:

$$\sum_j^N V_{ij} q_j = \mu - \chi_i \quad (20.)$$

The solution of this set of equation is not straight forward. Streit and Mintmire suggest that one should use the inverse V_{ij}^{-1} of matrix V_{ij} so that one can solve for atomic charges q_i and the chemical potential μ :

$$q_i = \sum_j^N V_{ij}^{-1} (\mu - \chi_j)$$

$$\mu = \frac{\sum_{i,j}^N V_{ij}^{-1} \chi_j}{\sum_{i,j}^N V_{ij}^{-1}} \quad (21.)$$

Note that Streit and Mintmire original approach all the atoms are allowed to be ionized. Consequently all the atoms are involved in this charge optimization procedure.

As pointed out above, an empirical potential is necessary to simulate the core-core interactions. To maintain a physically reasonable internuclear distance Streit and Mintmire propose a potential of their own which is fitted together with the electrostatic interactions. Moreover, Streit and Mintmire found out, that strictly pair-wise potentials for the non-electrostatic interactions can lead to unphysical behavior near the oxide surface which means surface atoms with a different coordination are too weakly bound due to the insensitivity on coordination of pair potentials. Streit and Mintmire write further that except from the facts mentioned above, any standard empirical potential can be used to model the non-electrostatic interaction. They use an embedded-atom method (EAM) approach as described in section 2.2.2. As pointed out there, EAM interatomic potentials are especially well suited to model metallic bonding.

The total energy of the ionic system should be understood as a sum of the electrostatic energy and the contribution of the EAM potential energy

$$E_{eam} = \sum_i^N F_i[\rho_i] + \frac{1}{2} \sum_{i,j}^N \phi_{ij}(r_{ij}) \quad (22.)$$

The formulas for the embedding energy $F_i[\rho_i]$, the local atomic density ρ_i and the pair potential $\phi_{ij}(r)$ as they are used by Streit and Mintmire are given here:

$$\begin{aligned}
F_i[\rho_i] &= -A_i \sqrt{\frac{\rho_i}{\xi_i}}, \\
\rho_i(r) &= \sum_{i \neq j}^N \xi_j \exp[-\beta_j(r - r_j^*)], \\
\phi_{ij}(r) &= 2B_{ij} \exp\left[-\frac{\beta_{ij}}{2}(r - r_{ij}^*)\right] - C_{ij} [1 + \alpha(r - r_{ij}^*)] \exp[-\alpha(r - r_{ij}^*)]
\end{aligned} \tag{23.}$$

Some comments on this potential:

1. The potential is of Finnis-Sinclair¹³³ form.
2. The charge density ρ_i given in equation 23 is different from the charge densities used in the electrostatic formulation. So, there is no unique charge density explaining the whole metal or ionic system.
3. The form of $\phi_{ij}(r)$ should fulfill that the system behaves as a universal equation of state plus an electrostatic term.

The parameters for the whole Streitz and Mintmire formalism have been produced by fitting a range of structural parameters of Al and α -alumina, i.e. the cohesive energy, lattice parameters, elastic constants for both species, as well as surface energies. The parameters found by Streitz and Mintmire are given in Table 2.1.

Atomic parameters						
	χ (eV)	J (eV)	ζ (Ang. ⁻¹)	Z	A (eV)	ξ
Al	0.000000	10.328655	0.968438	0.746759	0.7638905	0.147699
O	5.484763	14.035715	2.143957	0.000000	2.116850	1.000000
Pair parameters						
	r^* (Å)	α (Ang. ⁻¹)	β (Ang. ⁻¹)	B (eV)	C (eV)	
Al-Al	3.365875	1.767488	2.017519	0.075016	0.159472	
O-O	2.005092	8.389842	6.871329	1.693145	1.865072	
Al-O	2.358570	4.233670	4.507976	0.154548	0.094594	

Table 2.1 Parameters for Streitz and Mintmire's potential (ES and EAM) according to Ref.¹⁰².

2.3.2 Ewald summation

As mentioned above the Streitz and Mintmire method¹⁰² involves partially charged atoms. This has some severe implications as the interaction of charges can be of long-range nature.

Considering the simplest form of Coulomb potentials between a charge q_i at position r_i and charge q_j at position r_j and the corresponding potential energy

$$V(q_j, r_{ij}) = \frac{1}{4\pi\epsilon_0} \frac{q_j}{r_{ij}} \quad (24.)$$

$$U(q_i, q_j, r_{ij}) = \frac{1}{4\pi\epsilon_0} \frac{q_i q_j}{r_{ij}} \quad (25.)$$

The interaction energy decays with one over the distance r_{ij} where $r_{ij} = r_j - r_i$.

In a many body system the computation of properties which depend on pair terms requires $N \times (N - 1)$ operations. Although one can reduce this to half the amount of operations due to symmetry it is still an asymptotically $O(N^2)$ scaling. As it is explained in the MD section (2.1.1) one usually introduces cutoff distances which give a linear scaling. In the case of long-range interactions this is hardly possible, because the interactions are even for long distances not negligible.

Since the beginning of the 1980s several ways have been found to incorporate long-range effects at a more reasonable computational effort which means scaling of $O(N^{3/2})$ down to $O(N)$ have been achieved. Here the Ewald summation method is explained because it is suggested by Streit and Mintmire's publication. More details on Ewald summation and other (faster) methods, e.g. particle-particle particle-mesh method or fast multipole methods can be found in MD textbooks such as ¹²¹ and ¹²², in the comprehensive article of the John von Neumann Institute for Computing in Juelich, Germany ¹⁴⁸ or in the survey on Ewald summation techniques by Toukmaji and Board ¹⁴⁹.

The key idea of Ewald summation is to recast the sum with unpleasant converging behavior into two rapidly converging series: a real-space sum and another one in the reciprocal-space plus a self-energy term. This looks like:

$$\frac{1}{2} \sum_{i \neq j} \frac{q_i q_j}{r_{ij}} = \frac{1}{2} \sum_{i \neq j} \frac{q_i q_j}{r_{ij}} \operatorname{erfc}(\alpha r_{ij}) + \frac{1}{2\Omega} \sum_{\vec{k}} \frac{4\pi}{k^2} \exp\left(\frac{-k^2}{4\alpha^2}\right) \left| \sum_i q_i \exp(i\vec{k} \cdot \vec{r}_i) \right|^2 - \frac{\alpha}{\sqrt{\pi}} \sum_i q_i^2 \quad (26.)$$

For the separation into real- and reciprocal space the following facts are exploited:

1. The error function $\operatorname{erf}(x)$ and its complimentary $\operatorname{erfc}(x)$ sum up to one.
2. The product of the function with the error function and its complementary is made. Then, the product with the complementary converges quickly in the real-space.
3. The error function term which slowly converges in the real-space is Fourier transformed to the reciprocal-space, where it also converges quickly.
4. A self-energy term is needed to correct for self-interaction which are implicit in the reciprocal space summation.

All the convergence and scaling properties are dependent of the parameter α which determines the width of the Gaussian distribution in the error functions. Furthermore the real-space and the reciprocal-space cutoff play a major role. They are interdependent and correlated to the α parameter for a given error tolerance. A wide discussion on the choice of these parameters can be found in the literature ^{149, 150}. The scaling of Ewald summation is in the best case $O(N^{3/2})$.

2.3.3 Application and improvements of Streitz and Mintmire's method

Streitz and Mintmire's potential ¹⁰² is more than one hundred times cited. It is applied mainly in the context of oxidation and growth of oxide scales ¹⁵¹⁻¹⁵⁵. Nevertheless, the method has some limitations, e.g. the restriction to Al and its oxide and in terms of computational efficiency a rather long cutoff for the EAM potentials or long-range treatment (Ewald summation). The original method has been further developed. First, the method itself was improved in the sense of computational efficiency: parallelization, application of preconditioners in the solution of the linear systems of equations ¹⁵⁶ and fast multipole codes ¹⁵⁷ were implemented. Then the method is transferred to other element such as Ti ¹⁵⁸ or Zr ¹⁵⁹ and to nc composites such as fcc Al+ α Fe₂O₃ ¹⁶⁰, and even non-metallic systems such as Si/SiO₂ ¹⁶¹. Among the groups which apply the method still on Al and its oxide several reparameterizations can be found, e.g. in references ^{159, 162} and ¹⁶⁰. Often these works aim for potentials which are more transferable, i.e. applicable for a wider range of simulation geometries than metal/oxide interfaces or surfaces, or computationally more efficient.

The group based around Vashishta, Nakano, Campell and Kalia are using the Streitz and Mintmire framework the most. They developed the fast multipole method, the preconditioned conjugate gradient methods and heavily parallel codes. In the year 2000 the group presented a work where they simulated more than one million atoms ¹⁶³ using variable charge MD with all sorts of computational improvements. The link between this group and this work is Dr. Olivier Politano from the Interdisciplinary laboratory Carnot de Bourgogne (ICB) at the Burgundy university in Dijon, who spent three months with the Vashishta group to develop his own variable charge MD code in 2002. This implementation is the basis for the present implementation of Streitz and Mintmire's method at the Paul Scherrer Institut.

Also Zhou and Wadley developed Streitz and Mintmire's pioneering work further. They wanted to generalize the model to use more than one metallic element at the time (i.e. in the simulation of interfaces between different metal alloy oxides). However this is not straightforward with the original version of the variable charge method because it produces charge fluctuations in a purely metallic alloy. Additionally, instabilities in the charges can prevent the variable charge model from being combined with other existing EAM potentials (for Al or other elements). In the analysis of the problems, the authors show that the absolute values of the charges on neighboring anions and cations increase without any limitations when the distance between them is reduced. In fact, this produces enormous attractive Coulomb forces between ions with opposite charge which reduces the distance further. The solution proposed by Zhou and Wadley is the introduction of lower and upper bounds on atomic charges. This is achieved by adding penalty terms to the electrostatic energy which keep the charge for a given weight between the barriers. Unfortunately the linear nature of the derivate of the electrostatic energy with respect to the charges breaks down with this. Obtaining the charges cannot be done any more by solving linear systems of equations but has to be done by algorithms for non-linear systems. Zhou and coworkers suggest applying a Newton-Raphson method ¹⁶⁴. The computational effort increases in this case quadratically with the number of charges whereas the solution of linear systems scales linearly. Zhou and coworkers have also published a potential for Zr and ZrO. More recently they published potentials for many different metal elements such as Al, Co, Ni, Fe in combination with O ¹⁶². The work of Zhou and coworkers is also applied in the context of oxidation, especially for field enhanced oxidation of Al and Zr ^{165, 166}.

3 Results on developments

3.1 Development I - Local chemical potential approach

3.1.1 Motivation

Streitz and Mintmire's approach presented in section 2.3.1 has been developed to study the interface between Al and its oxide where mainly the α -Al₂O₃ state of oxidation has been considered. It produces average charges for the corundum structure which are for the O ions -1.9 e and for the Al ion about +2.85 e. This is within the range of literature values which predict cation charges between +1.09 and +3.0 e in the corundum structure¹⁶⁷⁻¹⁷¹.

Although the charges for the corundum structure are well reproduced the method has some drawbacks e.g. artificially high charges in case of small interatomic distances and interactions with large cutoffs. The major limitation considering the charge update is the fact that all atoms in the simulation sample are assumed to be ionizable which means, that all of them are included in the charge optimization procedure. However it is clear that Al atoms in the bulk metallic region far enough away from the interface or surface do not carry any charge as it can be seen from a simulation of oxidation of an Al surface¹⁵³ where the Al/AlO interface is visible (Figure 3.1).

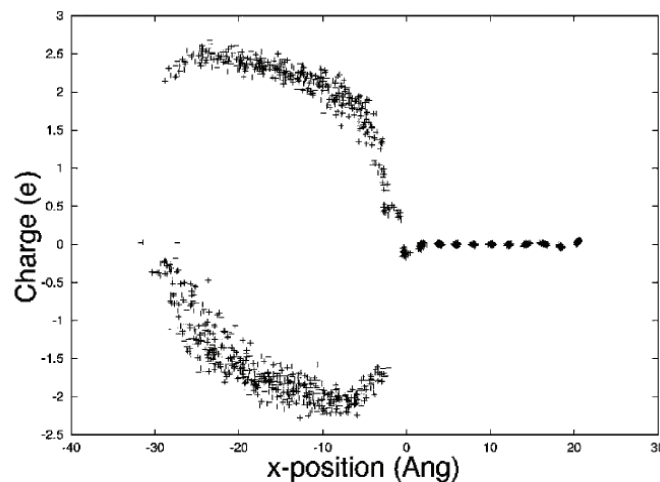


Figure 3.1 Charges in distance of an alumina/Al interface. Positive charges represent Al and negative charges O atoms where the charges are given in atomic charges units e. Source: Ref. ¹⁵³.

Small fluctuations due to positional changes can also be represented by bond order potentials or EAM potentials. Still, charges on all atoms especially also on neutral metallic atoms are time intensively computed. This becomes worse in the case of dilute O impurity distributions where the large majority of atoms are Al atoms. In this case only a few Al atoms close to the O

impurities are oxidized. Only those atoms and the impurities themselves are significantly ionized. This fact can be seen in Figure 3.2 which shows the radial charge distribution with increasing distance from a single substitutional O atom in bulk fcc Al relaxed with Streitz and Mintmire’s potential¹⁰². Nonetheless, Streitz and Mintmire’s approach computes charges for all the atoms also in this scenario.

The situations of isolated O atoms or clusters of O atoms in bulk fcc Al are more likely scenarios for dilute concentrations of O impurities which are simulated here. Consequently, charges have to be calculated in local environments of these O impurities only. A large fraction of Al atoms can be treated as neutrally charged which allows for excluding them from the charge optimization procedure. This promises an improvement of the performance. Around the O impurities a lot of small neutrally charged regions are formed for the charge update. All of these regions have their own local chemical potential. So, the approach developed for this purpose is called “local chemical potential approach” and is described in this section.

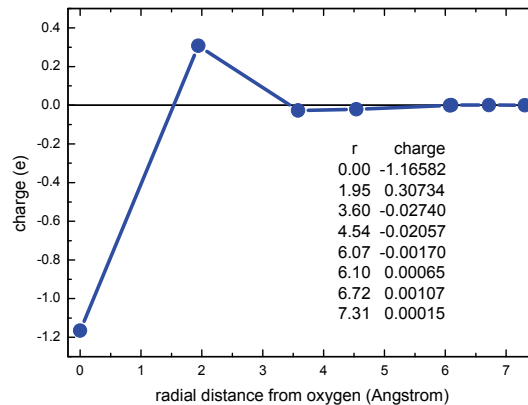


Figure 3.2 Charges with increasing distance from an isolated O atom in fcc Al. The charge at distance 0 represents the O atom’s charge.

3.1.2 Streitz and Mintmire’s approach reconsidered

Streitz and Mintmire’s charge optimization problem minimizes the electrostatic energy under the constraint of global charge neutrality using a electronegativity equalization scheme. Since the electrostatic energy is a quadratic expression in the charges and the problem deals with one linear constraint, this is a so-called “quadratic program”. (Quadratic programs are a class of optimization problems with a quadratic objective function and linear constraints.)

$$\begin{aligned} \min E_{es} &= \min \sum_{i,j}^N q_i \chi_i + \frac{1}{2} \sum_{i,j}^N q_i q_j V_{ij} \\ \text{subject to } &\sum_i^N q_i = 0 \end{aligned} \quad (27.)$$

In mathematics, quadratic programs are solved by using a Lagrange multiplier approach.

$$\min_{q_i, \mu} \left(\sum_{i,j}^N q_i \chi_i + \frac{1}{2} \sum_{i,j}^N q_i q_j V_{ij} + \mu \left(\sum_i^N q_i - 0 \right) \right) \quad (28.)$$

The Lagrange multiplier μ in equation 28 corresponds exactly to the global chemical potential in the previous solution (see section 2.3.1 equation 19) which is necessary to achieve the electronegativity equalization. The solution of the Lagrange approach is usually obtained by minimizing the modified objective function (expression 28) using partial derivatives for the variables (here q_i) and for the Lagrange multipliers (here μ) and equating the set of derivatives with zero. The equations can be arranged in a linear system of equations. In block notation it looks like expression 29.

$$\begin{pmatrix} \tilde{V} & \vec{C} \\ \vec{C}^T & 0 \end{pmatrix} \begin{pmatrix} \vec{q} \\ \mu \end{pmatrix} = \begin{pmatrix} \vec{\chi} \\ 0 \end{pmatrix} \quad (29.)$$

The \tilde{V} matrix contains the element for the pair interactions V_{ij} in expression 17. The vectors \vec{q} and $\vec{\chi}$ contain the atomic charges or electro-negativities as elements. The vector \vec{C} contains all ones and is necessary to obtain the equivalent system as the one given by the derivation of equation 28. The solution of the system is straight-forward and many numerical tools exist to solve such linear systems of equations. However, the system contains a fully occupied (dense) matrix as all atoms are considered in the charge optimization and interact via a long-range terms. The dense matrix gives serious limitations in terms of computational efficiency and memory usage.

3.1.3 Charge optimization for the dilute oxygen limit

The strategy of solving the quadratic program with one linear constraint through Lagrange multipliers and linear systems of equations offers new possibilities for the situation of dilute O in Al described in the beginning of the chapter. As it is shown in section 3.1.1 in case of a single

O in a bulk Al matrix only a few Al atoms in the neighborhood of this O atom are charged significantly differently from zero. In other words it is sufficient to solve the charge optimization problem for those atoms only. Instead of using one constraint for charge neutrality which holds for the whole system it is assumed that each sub-region around an isolated O atom or around a cluster of O atoms is neutrally charged. A neutrality constraint is assigned to each sub-region: the local chemical potentials. Following this idea, one can classify each atom in one of three categories:

1. Atoms which are closer to the O atom than a certain cutoff distance (including the O atoms) have to get a charge and need to be charge optimized under a constraint of local charge neutrality. (Green atoms in Figure 3.3)
2. Atoms which are far enough away from all the O atoms are completely neglected in the charge optimization and a fixed value of 0 e is assumed for their charge. (Grey atoms in Figure 3.3)
3. Between class 1 and class 2 atoms there lies the third class of atoms. They form buffer regions for the charges in the optimization processes. This is required because of the artificial interface at the cutoff distance. As these atoms lay outside of the main cutoff for charge optimization their charge in absolute value should be as small as possible. Therefore these atoms are included in the charge optimization however their charge is constrained to zero. (Red atoms in Figure 3.3)

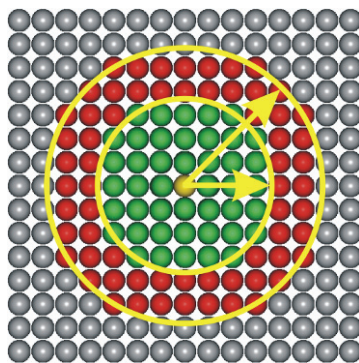


Figure 3.3 Optimization regions around a single O atom (yellow). Green atoms in the inner circle are chargeable and therefore fully optimized. Red atoms are considered in the optimization, however their charge is constrained to zero. Grey atoms outside the outer sphere are not considered in the charge optimization.

In practice atoms are classified into the three groups via two cutoff radii. The smaller cutoff is used for the region of full charge optimization and the larger cutoff is used for the separation between constrained and neglected atomic charges. In case of several impurities more than one neutral region can be formed. If two or more O atoms are closer than the larger cutoff the

regions around them are merged to one neutral region. If the distance between the O atoms exceeds the larger cutoff, separate neutral regions are formed. In both cases each of these neutral regions has got its own charge neutrality constraint.

The classification of the atoms is done by mapping the O positions into a graph, i.e. a construction used in computer science which consists of vertices and edges. Here, each O atom is assigned to a vertex and edges are drawn in the graph if two O atoms are closer than twice the larger cutoff distance. A depth-first search algorithm can be used to determine the connected subgraphs which represent the merged neutral sub-regions. By the determination of the subgraphs each O atom can be assigned to its sub-region. Al atoms can be labeled as chargeable, constrained or neutral, depending on the distance to the closest O atoms. In case of chargeable or constrained Al atoms the sub-region-label corresponds to the label of the closest O atom and is assigned accordingly.

The charge optimization problem turns into a solution of a minimization problem which has got now fewer variables, because in the ideal case a lot of atoms should be neglected from the charge optimization. Simultaneously, a lot more constraints have to be fulfilled, i.e. one for each region (charge neutrality) and one for each constrained atom (atomic charge equal to zero). All these constraints are still linear. So the problem is still a quadratic program with this time multiple linear constraints. The solution is analogous to the solution discussed above: 1) Introduction of Lagrange multiplier; 2) Minimization for both charges and Lagrange multipliers which leads to the solution of the following system of linear equations:

$$\begin{pmatrix} \tilde{V} & \tilde{C}_0 & \tilde{C}_b \\ \tilde{C}_0^T & 0 & 0 \\ \tilde{C}_b^T & 0 & 0 \end{pmatrix} \begin{pmatrix} \vec{q} \\ \vec{\mu} \\ \vec{\lambda} \end{pmatrix} = \begin{pmatrix} \vec{\chi} \\ 0 \\ 0 \end{pmatrix} \quad (30.)$$

Here the block matrix \tilde{V} represents the pair interaction V_{ij} between charges equivalently to expression for V_{ij} in expression 20. The rank of quadratic matrix \tilde{V} is equal to N' the number of atoms which are considered in the optimization procedure, i.e. the number of chargeable and constrained atoms. Hence this is also the rank of the vector \vec{q} . The number of disconnected neutrally charged regions N_0 determines the size of the matrix of the local charge neutrality constraints \tilde{C}_0 ($N \times N_0$) and the rank of the vector $\vec{\mu}$. The matrix \tilde{C}_0 contains zero and one elements to link the atoms to the corresponding neutral region. Finally, the matrix \tilde{C}_b which is

the key for constrained charges on atoms is of size $N' \times N_b$ where N_b stands for the number of constrained atomic charges. This matrix contains at most one non-zero element per column and row which is then equal to unity and fixes the constraint.

The final system of linear equations which has to be solved is of the order $N' + N_0 + N_b$. To improve the speed of the solution of the system this sum has to be much smaller than the number of atoms in the system. So, in the dilute O limit it should hold, $N' + N_0 + N_b \ll N$ (N is the total number of atoms).

3.1.4 Optimization of long-range interaction

As explained in section 2.3.2, long-range interactions are in the nature of systems with atomic charges. They affect the energy evaluation which is used to determine the charges as well as the final electrostatic properties (energy, forces and stresses). In the previous section it is the pair-interaction determined by the \tilde{V} matrix which has to be treated with the Ewald summation method.

As described in section 2.3.2 the Ewald summation or its accuracy and convergence behavior is determined by three interdependent parameters: The real-space cutoff r_c , the reciprocal-space cutoff k_c and the Ewald convergence parameter α . Ultimately, the two cutoff values are connected to the α parameter and the speed of convergence of the whole summation is controlled with this. An increase of the real-space cutoff for a given α value decreases the contribution of the reciprocal space significantly. For the Al simulations containing O an α value of 0.25 is assumed. If the O concentration is dilute, e.g. a few O atoms in bulk Al, and a large enough real-space cutoff (bigger than 13 angstroms) is chosen the contribution of the reciprocal-space to the energy is smaller than a percent. In other words the real-space summation and the self-energy correction give the major contributions to the Ewald summation. This leads to the idea, to neglect the reciprocal-space summation in scenarios of dilute charges. However, this is unneeded and therefore it makes more sense to go back to the direct summation.

The fact that it is possible to compute charges in the dilute regime without any long-range method can be understood in two ways. First, there is no repeating charge distribution in the configuration which causes a conditional convergence as reported in section 2.3.2. The second fact is that the multipole expansion of the charge distribution of such a neutral region has got no $1/r$ -contribution since the monopole vanishes in this case. As at most terms of order $1/r^3$ are

present in the expansion all functions should decay rapidly to zero. This makes the long-range treatment negligible.

To verify these considerations, a test sample containing two separated, neutrally charged sub-regions with one and three O atoms (Figure 3.4) is charge optimized using four different approaches and the local chemical potential approach in every case. The charges for the atoms a, b, c and d as well as the electrostatic energies are given in Table 3.1

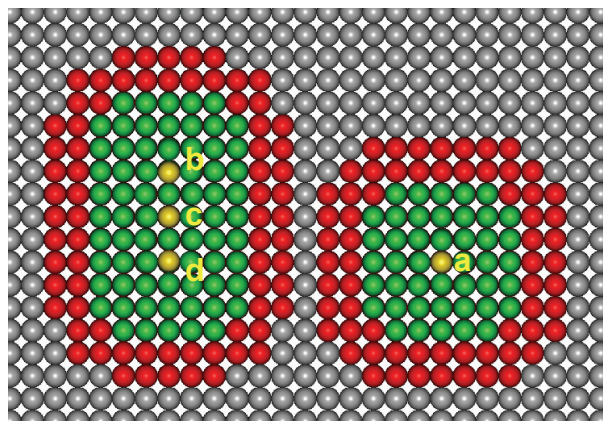


Figure 3.4 Sample with two separated, neutrally charged sub-regions with three or one O atoms, respectively.

The four different approaches are:

1. Full Ewald summation with real- and reciprocal-space contributions. The α value is set to 0.25.
2. Same as “1.” without the reciprocal-space contribution
3. Direct real-space summation which includes all Coulomb interactions between atoms within the simulation cell and its nearest neighbors.
4. Same as “3.” however only Coulomb interactions within each neutral region are considered.

	Approach 1	Approach 2	Approach 3	Approach 4
Charge a	-1.1643	-1.1658	-1.1641	-1.1643
Charge b	-1.2105	-1.2128	-1.2105	-1.2105
Charge c	-1.2533	-1.2562	-1.2532	-1.2533
Charge d	-1.2105	-1.2128	-1.2105	-1.2105
Electrostatic Energy	-15.393	-15.425	-15.392	-15.393

Table 3.1 Values of converged charges on O atoms and the total electrostatic energy for the system considered in Figure 3.4. The unit of the charge is e, the energy is in electron volts (eV).

As a consequence of this result one can think of optimizing all the charges in a direct summation within each neutrally charged sub-region separately. As there are no more interactions between the sub-regions (fourth approach) a large part of the electrostatic pair-interaction matrix \tilde{V} is equal to zero. In other words, the system of equations which has to be solved to obtain the charges in the local chemical potential approach is sparse. Solving sparse matrix problems is a rather standard problem, which has two major advantages: First it is less memory consuming and second it is much more efficiently doable in the sense of time. As the problem of solving a sparse linear system of equations is so frequently used and well studied, there exist different advanced software packages. To improve the charge optimization in this project, the direct solver UMFPACK¹⁷²⁻¹⁷⁵ is implemented as a library.

3.1.5 Timing of the approach

To illustrate the power of the local chemical potential approach as well as the huge saving in time which comes from the modification of the long-range computation, four samples are tested. The samples contained 500, 4000 or 13500 Al atoms and one O atom. In case of the sample with 13500 Al atoms the four O atoms distribution presented in the previous example is added (Figure 3.4). For each of the systems the charges are optimized using Streit and Mintmire original technique including Ewald summation, the local chemical potential approach using still the full Ewald summation (LCP1), equivalent to approach 1 in the previous section, and the local chemical potential using direct summation (LCP2), which refers to approach 4. All the calculations are done on the same machine. Time is given in Table 3.2 in seconds.

	Streitz and Mintmire	LCP1	LCP2
500 Al + 1 O	0.78	1.37	0.10
4000 Al + 1 O	85.47	8.27	0.17
13500 Al + 1 O	1357.23	26.06	0.32
13500 Al + 4 O	1350.49	232.16	1.52

Table 3.2 Wall-clock time in seconds for the charge update for four fcc Al systems with interstitial O atoms. Streit and Mintmire is the original method, the version LCP1 is the one discussed in section 3.1.3 (analogous to approach 1 in Table 3.1) and the LCP2 version contains direct summation and the UMFPACK¹⁷²⁻¹⁷⁵ solver (analogous approach 4 in Table 3.1).

As one can see from Table 3.2 the local chemical potential approach is in this dilute O regime several orders of magnitudes faster than the original approach. However there are some interesting aspects: The Streit and Mintmire approach is competing with LCP1 when the system is rather small. LCP1 loses some time in the determination of the atomic labels (chargeable, constrained or neutral). Furthermore it happens for too small systems that all atoms

are included in the optimization scheme, which again gives no improvement compared to Streit and Mintmire or even increases the effort due to the additional variables in the optimization. The other interesting aspect is the nearly linearly increasing time in LCP2 for systems containing one O atom: Here the time is increasing also because more atoms have to be considered in the determination of the neutral regions. Additionally, one sees that the time for the charge optimization with four O atoms is five times bigger than in the case with one O atom which fits to a linear increase in the computational costs.

3.1.6 Implementation

The serial implementation is introduced in the standard MD code used in the Materials Science and Simulation group¹⁰⁷ at Paul Scherrer Institut which is based on the program Moldy¹⁷⁶. Additional subroutines are added for the determination of the neutrally charged sub-regions, for the determination of the electronegativity, for the build up of the V -matrix, for the solution of the system of equations using UMFPAK¹⁷²⁻¹⁷⁵ as a library and for separated energy, force and stress calculations for the electrostatic contributions. To improve the computational efficiency, the possibility of updating the charge not in every step is implemented into the code. Like this, the still time-consuming charge update can be done in every n^{th} step where n is an integer number bigger than zero. The size of n as well as the cutoffs described in Figure 3.3 for the determination of the neutral charged regions can be adjusted before a run to have a good balance between energy conservation and computational efficiency. Usually n is chosen between 1 and 10 and the cutoffs are set to values between 8 and 10 angstroms for the inner and to values between 12 and 16 angstroms for the corresponding outer cutoff. The smaller radii were used for tests with single O impurities in bulk fcc Al environment. For waste majority of the simulations the larger cutoffs of 10 angstroms for the inner and 16 angstroms for the outer are used. Beside these cutoffs for the charge optimization, a cutoff for the electrostatic force and stress calculation is used. This cutoff is set to 13 angstroms which is the same value as Streit and Mintmire's cutoff for the real-space interaction.

To apply the local chemical potential in parallel simulations a good load distribution between computing instances has to be found without increasing communication costs too much. For the parallel implementation it is assumed that a dilute O concentration is present. This means that many small neutral sub-regions around O atoms are present in the sample. These neutral regions are isolated and not interacting with each other. Under this assumption, the charge optimization is distributed by assigning neutral sub-regions to threads. In the beginning of each charge optimization, every thread sends the positions of all its O atoms to the root process. Here the clustering for the O atoms according to the graph theory procedure above is performed. Afterwards each neutral region is assigned to a single core. The data of all the atoms within the

neutral region are sent directly to the corresponding core. Charges are found by using the same solver as in the serial case (UMFPACK) for each thread separately. Before the charges are sent back to the core of origin of each atom, electrostatic properties such as energies, forces and stresses are calculated for all the charged atoms on the charge optimization cores. The computing cores for the charge optimization are the same as the cores for the execution of the rest of the MD code.

3.2 Development II - First potential

3.2.1 Motivation

Streitz and Mintmire delivered a full potential for the simulation of Al and AlO interfaces: All the electrostatic interactions are included in the functions used in the variable charge method. All non-electrostatic interactions, i.e. interactions independent from charges, are included in a potential of Finnis-Sinclair type.

The Streitz and Mintmire potential uses a rather long cutoff (about 13 angstroms) and is therefore not very efficient. It can even give serious limitations if one wants to simulate larger samples. This is also reported by Tomar and Zhou¹⁶⁰ who refitted for different reasons the EAM potentials including this point of large cutoffs using the software package GULP¹⁷⁷.

Another issue is the specific simulation of dilute O impurities. As it is described in section 2.3.1 Streitz and Mintmire's EAM potential is fitted to bulk properties of fcc Al and α -Al₂O₃, i.e. the corundum structure. Both are very regular crystalline structures. However little attention is given to isolated O defects which have to be considered, when it comes to dilute O impurities in bulk Al.

The third reason to change the EAM potential is the comparison to existing work. Particularly, this is work published by Prof. Yuri Mishin and Dr. Vladimir Ivanov³¹ from George Mason University in Fairfax VA which is subject of section 4.3. For this purpose it is required that the Al-Al interactions can be simulated using Mishin and Farkas Al potential¹⁷⁸. Consequently a new potential is developed with a given Al-Al interaction and Al-O and O-O interactions which have to be defined and fitted.

3.2.2 Simulation of defect structures

In order to fit the new atomic potential, dilute O in Al structures and corresponding energies are searched in the literature. Unfortunately, it has not been possible to find any data on isolated O

defects in a perfect fcc Al matrix at the time. So, a small database containing O defects in the fcc Al is produced by ab initio calculations using the software package VASP¹¹⁴⁻¹¹⁷.

In these ab initio simulations, the aim is not to generate energies which are of highest quality as empirical potentials, for which the data is used, are anyway limited in accuracy. The goal is more to have an optimized atomic structure around the defect and a moderate energy estimate for the given structure, which can be reproduced by the fitting. As high quality ab initio results are not an aim, it is possible to handle configurations which contain more than one hundred atoms. The rather large simulation samples have the advantage that interactions between defects in the configuration and its periodic replicas are reduced. As an initial, pure configuration an fcc Al lattice containing 108 atoms is used. This corresponds to $3 \times 3 \times 3$ fcc unit cells containing four atoms each. In this fully periodic reference lattice, O defects are placed by inserting O atoms or substituting Al to O atoms. The following geometries are generated:

1. The pure structure containing 108 Al atoms.
2. A substitutional structure where exactly one atom is substituted by an O.
3. An interstitial structure where the O is placed in the octahedral position between the Al atoms.
4. An interstitial structure where the O is placed in the tetrahedral position between the O atoms.
5. An interstitial structure where one Al is slightly moved and the O is then placed in a [100]-dumbbell situation.
6. The same structure as 5. where the slightly moved Al atom is additionally substituted by an O atom.
7. A structure containing two substitutions on neighboring lattice sites. The distance between them is $\sqrt{2}a_0 / 2$.
8. A structure containing two substitutions with the distance of one lattice constant (a_0) between them.
9. A structure where four atoms forming a tetrahedron are substituted by O atoms. The edge length of the tetrahedron is $\sqrt{2}a_0 / 2$.
10. A structure where the six face center atoms of the fcc primitive cell are substituted by O atoms.
11. A structure where the eight corner atoms of the fcc primitive cell are substituted by O atoms.
12. A structure where the same atoms as in 10. and 11. are substituted by totally 14 O atoms.

All these structures are ionically relaxed, i.e. structure optimized, by VASP ¹¹⁴⁻¹¹⁷ and for each system the energy is determined. VASP is used with projector augmented wave pseudopotentials ^{113, 118} using the PBE functional ^{119, 120}: PAW_PBE_Al for Al and PAW_PBE_Os_pv for O. As an energy cutoff 320 eV and 10 k-points per direction are chosen using a Monkhorst distribution. These selections are made according to a series of test runs to obtain reasonable energy values which give the aforementioned compromise between efficiency and accuracy (~ 0.1 eV).

The comparison of absolute energy coming from ab initio calculations with empirical data is unnecessary since empirical potentials are usually determined with respect to their cohesive energy. Therefore relative energies or energy differences which can be reproduced by the fitting procedure are calculated as results of the ab initio simulations. To keep things simple defect energies $\Delta E_{Abinitio}$ are defined by subtracting the total energy of the pure Al structure (1.) of the total energy of each defect structure. The energy of the solid O ($E_c = 2.558$ eV according to Baskes ¹⁷⁹) is not taken into account in the calculation of the defect energies. Table 3.3 summarizes information on the structures, number of atoms and defect energies.

Configuration	Al Atoms	O Atoms	Tot Atoms	$\Delta E_{Abinitio}$ eV
1. Pure	108	0	108	0
2. Substitutional	107	1	108	-8.61
3. Octahedral	108	1	109	-10.22
4. Tetrahedral	108	1	109	-8.54
5. [100]-Dumbbell	108	1	109	-10.76
6. Sub 2 O 1 st NN	106	2	108	-17.23
7. Sub 2 O 2 nd NN	106	2	108	-17.18
8. Dbl and Sub	107	2	109	-19.55
9. Sub 4 O	104	4	108	-33.24
10. Sub 6 O	102	6	108	-49.51
11. Sub 8 O	100	8	108	-66.79
12. Sub 14 O	94	14	108	-112.62

Table 3.3 Configurations used in the fitting including number of atoms and energy differences.

3.2.3 Fitting procedure

As described in section 3.2.1 the main idea for the new AIO potential is to fit Al-O and O-O EAM interactions to a given potential for Al-Al interactions¹⁷⁸. In the ideal case, the electrostatic interaction should be included in the fitting procedure. The first strategy for the fitting is to use the AIO defect structures described in 3.2.2. The energy differences given in Table 3.3 have to be reproduced as good as possible and the forces should vanish for all the given defect structures, as they are structure-optimized by ionic relaxation in the ab initio calculation. A further aim is that the new potential should have a cutoff distance which is of the same range as Mishin and Farkas Al potential: 6.78 angstroms.

In the fitting, the pair interaction function between Al-O and O-O as well as the O electron density are modeled as sums of cubic knot functions which give for each function the form

$$V(r) = \sum_{i=1}^N a_i (r_i - r)^3 \Theta(r - r_i) \quad (31.)$$

Here, the number of knot functions is N and Θ stands for the Heaviside step function^{180, 181}. The parameters to be found are the knot values a_i as well as the knot points r_i . For the embedding function it is assumed that it is the negative square root of the given electron density which gives no additional parameters in the fitting. Additionally, the modification of electrostatic parameter via the fitting program is done by changing the existing parameter in the given framework of Streitz and Mintmire using the local chemical potential approach.

To optimize the existing parameters an objective function representing a weighted measure between fit and targeted properties is calculated. For this purpose, the squared difference between fitted and target energy as well as a residual force norm for each structure are calculated, multiplied with a weight of choice and summed up. The objective is to minimize the value of the sum. The minimization of the objective function in the fitting is done either by a simulated annealing¹⁸² procedure or by a downhill simplex like algorithm¹⁸³. Usually simulated annealing is used to obtain a first guess for the knot points r_i for given knot values a_i . Then the results obtained by simulated annealing are refined using the more flexible downhill simplex method by simultaneously freeing up also the knot values. This allows for more accessible minima in the optimization and which improves the potentials. To have reasonable values for the fitting parameters they can be varied either in fixed bounds or in a range which is defined relatively to the actual value. Usually a change in fixed bounds is preferred in the fitting.

During the fitting it turns out that a modification of the electrostatic parameters slows down the procedure tremendously. So, in the beginning the electrostatic part of Streit and Mintmire¹⁰² is kept unchanged (including all the electrostatic parameters). This allows for computing all the electrostatic interactions (energies and forces) only once in the beginning of the execution of the fitting program and using those values in each iteration of the optimization.

The fitting of the defect structures shows that no embedding contribution for the O is necessary. So, no electron density is fitted for O atoms. However, it is rather difficult to reproduce the defect energies and the vanishing forces in the different structures in a reasonable accuracy. Considering again, Streit and Mintmire's work makes clear that the usage of all 1s orbital functions describing the delocalized valence electron distribution in the electrostatic part can be substituted by any other orbital function. To make the model more physical and to have more flexibility in the fitting procedure, 2s orbitals for O atoms and 3s orbitals for Al atoms are implemented. This needs a recalculation and reimplementation of the Coulomb interaction between these valence orbitals with each other and with the cores. According to Roothaan's work¹⁴⁷ it is found that one has to implement the following interaction terms into the electrostatic part. For the core-valence case integral $[a | f_b]$ one obtains the expressions 32 and 33.

$$[a | 2S_b] = \frac{1}{r_{ab}} \left[1 - \left(1 + \frac{4}{3} \xi_b r_{ab} + \frac{2}{3} (\xi_b r_{ab})^2 \right) \exp(-2\xi_b r_{ab}) \right] \quad (32.)$$

and

$$[a | 3S_b] = \frac{1}{r_{ab}} \left[1 - \left(1 + \frac{3}{2} \xi_b r_{ab} + (\xi_b r_{ab})^2 + \frac{1}{3} (\xi_b r_{ab})^3 \right) \exp(-2\xi_b r_{ab}) \right] \quad (33.)$$

In equations 32 and 33, ξ_b is a parameter which controls the spread of the electron distribution. For the valence-valence Coulomb integral three different cases of interactions are possible: Al-Al, O-O and Al-O. In the case of equal interaction partners the index $\xi = \xi_a = \xi_b$ is unique. So for the Al-Al and O-O interaction the terms given in equations 34 and 35 are obtained.

$$[3S_a | 3S_b] = \frac{1}{r_{ab}} \left[1 - \left(1 + \frac{419}{256} \xi r_{ab} + \frac{163}{128} (\xi r_{ab})^2 + \frac{119}{192} (\xi r_{ab})^3 + \frac{5}{24} (\xi r_{ab})^4 + \frac{1}{20} (\xi r_{ab})^5 + \frac{1}{120} (\xi r_{ab})^6 + \frac{1}{1260} (\xi r_{ab})^7 \right) \exp(-2\xi r_{ab}) \right] \quad (34.)$$

$$[2S_a | 2S_b] = \frac{1}{r_{ab}} \left[1 - \left(1 + \frac{37}{24} \xi r_{ab} + \frac{13}{12} (\xi r_{ab})^2 + \frac{4}{9} (\xi r_{ab})^3 + \frac{1}{9} (\xi r_{ab})^4 + \frac{2}{135} (\xi r_{ab})^5 \right) \exp(-2\xi r_{ab}) \right] \quad (35.)$$

For the Al-O interaction it holds $\xi_a \neq \xi_b$ and the valence-valence Coulomb integral looks like expression 36.

$$[2S_a | 3S_b] = \frac{1}{r_{ab}} \left[1 - (1 - \kappa)^3 \left\{ \frac{1}{48} (11 - 19\kappa - 44\kappa^2 - 20\kappa^3) + \frac{1}{12} (1 - 5\kappa - 4\kappa^2) \xi_a r_{ab} - \frac{1}{12} \kappa (\xi_a r_{ab})^2 \right\} \exp(-2\xi_a r_{ab}) - (1 + \kappa)^2 \left\{ \frac{1}{48} (37 - 22\kappa - 39\kappa^2 + 56\kappa^3 - 20\kappa^4) + \frac{1}{8} (6 + \kappa - 8\kappa^2 + 4\kappa^3) \xi_b r_{ab} + \frac{1}{4} (1 + \kappa - \kappa^2) (\xi_b r_{ab})^2 + \frac{1}{36} (1 + 2\kappa) (\xi_b r_{ab})^3 \right\} \exp(-2\xi_b r_{ab}) \right] \quad (36.)$$

In this equation 36, the abbreviation κ is equal to $\kappa = \frac{\xi_a^2 + \xi_b^2}{\xi_a^2 - \xi_b^2}$. All the expressions 32 to 36

are implemented into the code to obtain according electronegativities χ_i and pair interactions V_{ij} . With the given implementation the fitting is continued without changing the electrostatic parameters given in Streit and Mintmire's publication. Nevertheless, changing the orbital functions makes the fitting of the potential a lot easier.

3.2.4 Results

The newly fitted version of the potential is described by four knot functions for the Al-O interaction, four knot functions for the O-O interactions and the parameters listed in Table 3.4 which gives then the potential energy curves in Figure 3.5. The cutoff radius of the new potential is 6.78 angstroms which corresponds to the position of biggest distance of a knot point and to the cutoff of the underlying Al potential¹⁷⁸.

Knot function I	$V_{\text{Al-O}}$		$V_{\text{O-O}}$	
	r_i Ang.	a_i eV/Ang. ³	r_i Ang.	a_i eV/Ang. ³
1	1.74	-8.772	2.95	2.600
2	5.96	0.107	4.21	-0.580
3	6.73	0.644	4.77	0.423
4	6.78	-0.682	6.33	-0.047

Table 3.4 Positions of the knot functions and their coefficients for the Al-O and O-O pair potentials.

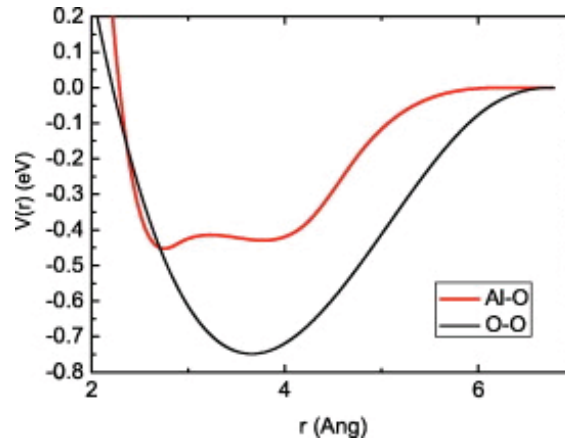


Figure 3.5 Radial energy functions for the pair potential between Al-O (red) and O-O (blue).

To have an idea about the quality of the fit the predicted energies of the ab initio code and the values achieved by the fit are compared in Table 3.5.

Many reasonable candidate potentials are tested. For this purpose, MS simulations using structures which contain the unrelaxed defects are produced. The expected result is a structure around impurities which is congruent with the structure obtained from the ionic relaxation in ab initio and an energy difference with respect to the perfect structure which are similar to the predicted values. For the potential presented here, these simulations show that the substitutional and the [100]-dumbbell interstitial O atoms can be reproduced very well. Also the energy differences are well reproduced. Figure 3.6 shows different properties of the substitutional defect produced with the new potential. However, for the other two interstitials (octahedral and tetrahedral) it is observed that also the O atom is moving during the relaxation. Interestingly, in both cases the atoms rearrange in [100]-dumbbell structures. This is a reasonable result when one considers the numerical instability of the defect atom in MS as no point group symmetries are exploited unlike the VASP calculations. Additionally the [100]-dumbbell is the lower energy configuration than the octahedral or tetrahedral. The changes in interstitial configurations happen for all the tested potential candidates.

Configuration	$\Delta E_{\text{Ab initio}}$ eV	$\Delta E_{\text{Fitting}}$ eV	$\Sigma \ F_{\text{Fitting}}\ ^2$ (eV/Ang.) ²
Pure	0	0	0
Substitutional	-8.61	-8.67	0.059
Octahedral	-10.22	-10.23	0.105
Tetrahedral	-8.54	-8.54	0.081
[100]-Dumbbell	-10.76	-10.63	0.108
Sub 2 O 1 st NN	-17.23	-17.19	0.125
Sub 2 O 2 nd NN	-17.18	-17.20	0.133
Dbl and Sub	-19.55	-19.62	0.177
Sub 4 O	-33.24	-33.35	0.269
Sub 6 O	-49.51	-49.72	0.389
Sub 8 O	-66.79	-66.84	0.484
Sub 14 O	-112.62	-112.45	0.608

Table 3.5 Comparison between energy differences from ab initio calculations and the values produced by the fitting. The last column contains the force norms produced by the fitting.

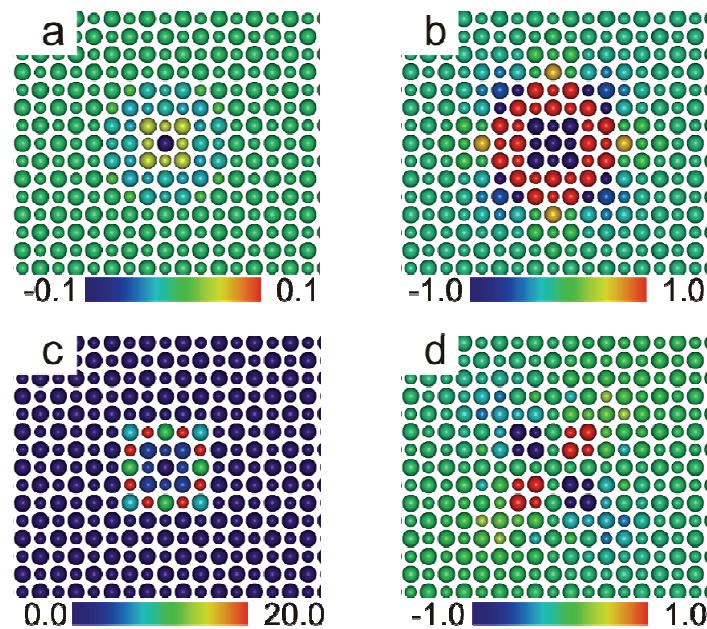


Figure 3.6 Substitutional O impurity (center atom) in FCC Al in which atoms are colored according to (a) converged charges, (b) hydrostatic pressure, (c) deviatoric stress* and (d) xy shear stress. Charges are given in multitudes of the elementary charges e and stresses are displayed in GPa.

* The deviatoric stress tensor is the difference between the full stress tensor and the hydrostatic stress tensor, and its second scalar invariant gives a measure of the maximum shear stress.

3.3 Development III – Second potential

3.3.1 Motivation

A second potential is presented which takes in the fitting the properties of the Al_2O_3 α -corundum structure (Figure 3.7) into account. The corundum structure is the most common form of alumina however it is not included in the fitting of the first EAM potential. Therefore the corundum description of the first potential is rather poor (see sections 3.3.2 and 3.3.4).

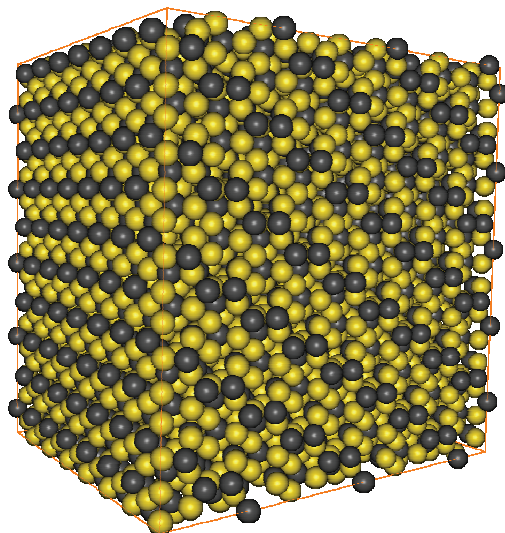


Figure 3.7 The α -corundum structure of Al_2O_3 . Grey spheres represent Al and yellow O atoms.

The corundum structure has a rhombohedral (trigonal) primitive unit cell and is determined via two internal parameters. These internal parameters are not relevant to maintain the symmetry but more relevant for the bonding. The description of corundum's basis vectors is given in Appendix A.

The corundum structure is important for the description of locally elevated O densities which could form oxide clusters or for the simulation of corundum precipitates in fcc Al. The aim in the fitting is an empirical potential which is able to reproduce properties of impurities, i.e. dilute O clusters and corundum properties simultaneously. The result should be a transferable potential. Therefore a compromise between the fitting of impurity properties and the reproduction of the corundum structure has to be found. In the interest of transferability, the values in the fitting are tried to be reproduced in a qualitative way. Transferability is a measure for the value of potentials.

3.3.2 Fitting procedure

Basically, the same fitting procedure as described in section 3.2.3 is applied. All the defect structures are included in the fitting with modified weights and data of the corundum structure is added as new target properties. For this purpose a small corundum sample (Figure 3.7) is generated according to geometrical data provided by Appendix A to compute its properties.

As during the fitting of the first potential the electrostatic interaction i.e. the description of the orbitals has been changed from all 1s to 3s for Al and 2s for O, the charges for the corundum structure are tested first. It is found, that the charges do not match the expected values of -2 e for O and +3 e for Al. So, the electrostatic parameters are modified to obtain the same values for Al and O charges as Streitz and Mintimire (-1.9 e and +2.85 e). Mainly the free parameter ξ_i which determines the spread of the orbital is adapted. In fact there is a whole set of pairs (one for Al and one for O) of parameters which produce reasonable charges in the corundum structure. Among these pairs, the one presented in Table 3.6 is selected according to the reproduction of Streitz and Mintmire's value for the electrostatic energy.

A change in the electronegativity χ_i with a constant difference between the values for both atom types does not affect the charges. The only value which changes under the new electronegativities is the chemical potential used in the charge determination. The self-Coulomb repulsions J_i and effective core charge Z_i are left unchanged as it is assumed that these values are given by Streitz and Mintmire due to a physical motivation. Old and new values for the electrostatic parameters are given in Table 3.6.

Potential	Atom	ξ	χ	J	Z
Old	Al	0.968438	0	10.38655	0.74679
	O	2.143957	5.484763	14.035715	0
New	Al	1.5679	-3.484763	10.38655	0.74679
	O	2.6665	2	14.035715	0

Table 3.6 New electrostatic parameters to use with the 2s and 3s orbitals.

Using constant electrostatic parameters implies that charges, the electrostatic energies, forces and stresses can not change, either. After the new parameters have been set they are incorporated into the fitting: Charges, electrostatic forces and energies for all the defect structures in section 3.2 are recalculated and adjusted to be used as precalculated, tabulated

values. Furthermore similar precalculations of energies and forces for the corundum structure are added to the fitting program.

In the case of corundum, the new EAM potential has to be fitted to reproduce the total energy given by Streitz and Mintmire's work ¹⁰² using the given electrostatic energy. The non-electrostatic forces and stresses calculated from the EAM potential have to compensate the given electrostatic forces and stresses as good as possible to obtain a force- and stress-free parameterization for the corundum structure. Simultaneously, the reproduction of the defect data in section 3.2 is desired. Fitting considering all the constraints given by the corundum structure and the defect structures is hardly feasible. So, a higher weight is given to the corundum structure and to the defect structures with only one O atom.

As soon as a reasonable candidate for a new potential has been found it is used to relax the corundum structure in a MS run. Unfortunately it is never observed that the morphology of the sample remains unchanged. As already described in the motivation of this section, the atomic positions in the corundum structure are determined up to two internal parameters. Changing these parameters gives again a symmetric structure with a different bonding nature. So, during the relaxation it is observed that all atoms move in a collective way to another "corundum" structure which can be described with different internal parameters.

The instabilities above can not be removed without including corundum's elastic constants in the fitting. However incorporating the elastic constants of corundum in the fitting is more tedious than using elastic constants of an fcc metal as Al. The α -corundum structure is trigonal and has six independent elastic constants (C_{11} , C_{12} , C_{13} , C_{33} , C_{14} and C_{44}) unlike cubic systems with three elastic constants (C_{11} , C_{12} , and C_{44}). To reproduce these six elastic constants in a qualitative manner the quadratic equations given in table IV of Ref. ¹⁸⁴ are used[†]. Consequently, a small corundum configuration is twice deformed according the deformations described in table IV of Ref. ¹⁸⁴ and the two deformed configurations for each deformation mode are directly stored in the fitting program. For each guess of parameters in the fitting energies are calculated for the undeformed and the two predeformed samples. The three parameters of the quadratic functions are analytically calculated. For this the three datapoints and in some cases already calculated elastic constants are used. Using this, the quadratic function given in Ref. ¹⁸⁴ can be

[†] In table IV of Ref. ¹⁸⁴ M. M. Ossowski, L. L. Boyer, M. J. Mehl, et al., Physical Review B **66**, 224302 (2002). the energy expression for strain 7 is in error and should be replaced by:

$$\Delta E / V = \frac{1}{8} V (5C_{11} - 4C_{12} + C_{33} - 2C_{13} + 4C_{44} + 12C_{14}) \eta^2.$$

approximated in a crude way. In the fitting mainly the sign of the elastic constants and a rough estimate of the value is tried to be reproduced.

Using these elastic constants made the fitting not easier because more constraints are added to the system. There is always a tradeoff between the reproduction of elastic constants and the accurate description of the principal stress components in the corundum structure. Also other objective values suffered from the incorporation of the additional terms in the objective function. During the fitting it turns out that for the description of the properties an electron density for O is necessary.

Different candidates are tested in MS runs. The good news is that positions of the atoms in the corundum structure do not anymore change for a fixed volume. Also the relaxation of the single O defect structures using MS shows plausible results. Therefore one of the candidates, which gives the best results in terms of defect structures and which produces a stable corundum structure, is chosen to be the next potential.

3.3.3 Results

The final version of the potential which models O-O and Al-O interactions in the full EAM form and which is applied in MD and MS simulations uses the parameters given in Table 3.7. The curves for the corresponding pair energies are displayed in Figure 3.8. The cutoff radius of the new potential is 6.45 angstroms which is slightly smaller than the cutoff of the underlying Al potential¹⁷⁸. However in practice, the values for the Al potential (6.78 angstroms) are used for all pair interactions.

Knot function <i>I</i>	V_{Al-O}		V_{O-O}		ϕ_O	
	r_i Ang.	a_i eV/Ang. ³	r_i Ang.	a_i eV/Ang. ³	r_i Ang.	a_i eV/Ang. ³
1	2.24	30.164	2.18	-1.796	1.34	1.491
2	4.69	2.051	2.22	11.680	2.44	2.919
3	4.73	-1.436	6.04	0.364	2.15	0.754
4	5.07	-0.300	6.45	-0.250		

Table 3.7 Positions of the knot functions and their coefficients for the Al-O and O-O pair functions and the O electron density of the second potential/

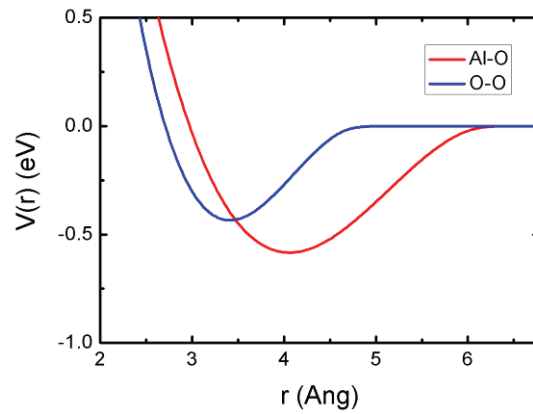


Figure 3.8 Radial energy functions for the pair potential between Al-O (red) and O-O (blue) for the second version of the potential

Using three or four knot functions is rather little but using more does not improve the fitting. For the pure Al system the same atomic cohesive energy (3.36 eV) is obtained as it is obtained from Mishin and Farkas Al potential ¹⁷⁸ since the pure Al interaction is not affected by the new potential. The fitting focused on the corundum structure and the single O defects. In Table 3.8 there is a summary of results obtained by the fitting and values for the application of the potential in a MS relaxation using the same defect structures in unrelaxed fcc Al. The elastic constants obtained for the corundum structure are given in Table 3.9.

System	Reference	Fitting	MS
Defect energies [eV]			
Substitution	-8.61	-8.70	-10.84
Tetrahedral	-8.54	-10.09	-11.56
Octrahedral	-10.22	-10.55	-11.56
100-Dumbell	-10.76	-9.57	-11.64
110-Dumbell	-9.34	N/A	N/A
Corundum			
Energy [eV]	-31.8	-31.95	-31.95
Pressure [GPa]	0.00	0.02	0.04

Table 3.8 Defect energies for the second potential. For corundum also the pressure in the sample is fitted and calculated.

	C_{11}	C_{12}	C_{13}	C_{33}	C_{14}	C_{44}
	[GPa]	[GPa]	[GPa]	[GPa]	[GPa]	[GPa]
Reference	497	164	111	498	-24	147
Fitting	452	82	206	406	-61	-302

Table 3.9 Elastic constants for the corundum structure. The reference values are taken from Ref. 102.

It is observed that the tetrahedral and the octahedral defects move into a [110]-dumbbell configuration upon MS relaxation. The properties displayed in Table 3.8 are rather poor especially for the single O defects. The stability of the structures is reduced compared the previous potential and an even more unfavorable structures appear. Still this is the best which has been obtained under the constraint of a stable corundum structure.

Another weakness of this potential is that the principal stress components in the corundum structure do not vanish. This means, that a corundum sample changes its shape as soon as the volume is allowed to adapt to pressure (NPE or NPT ensembles). This weakness affects also the behavior of the corundum at finite temperature. Unfortunately, fits with a better description of the interior stresses in corundum are not stable in the sense of the internal parameterization of the structure.

3.3.4 Comparison to first potential

The first obvious difference between the two potentials is the formal description of them. In case of the first potential no electron density and embedding function is fitted for the O. This means O-O interactions are modeled only via a pair potential. The second potential uses the full EAM framework for both elements, Al and O. Additionally the first EAM potential has two minima for the Al-O pair potential whereas the second potential has only one. This is a result of the fitting and the direct effect on properties is not yet known.

In terms of properties, the first potential reproduces ab initio data for the defect structures better than the second potential. This is also observed if O impurities in the bulk fcc Al matrix are relaxed using molecular statics. The first potential is able to stably relax the substitutional and the [100]-dumbbell interstitial. The octahedral and tetrahedral interstitials decay to [100]-dumbbells which is according to ab initio the most favorable interstitial site for the O in Al. For the second potential again the substitutional and [100]-dumbbell interstitial are stable. Octahedral and tetrahedral interstitials decay to [110]-dumbbells which are known to be less favorable considering the energies according to the ab initio calculation (see Table 3.8).

The major drawback of the first potential is the inability to reproduce the properties of the corundum structure. Firstly, the charges are not correctly reproduced due to a pair of electrostatic parameters which has not been adjusted when the orbital functions have been exchanged. Consequently the whole parameterization is not appropriate to simulate the corundum configuration. This can be observed during relaxation of the corundum structure, where all atoms move in the collective manner to a different “corundum” structure.

Comparing the two potentials in terms of possible influence on other defects, i.e. the perturbation of the lattice due to their presence via the stress field of the substitutional and the interstitial defect in the fcc lattice it can be seen that the distortion produced by the second potential is more compact but stronger (Figure 3.9).

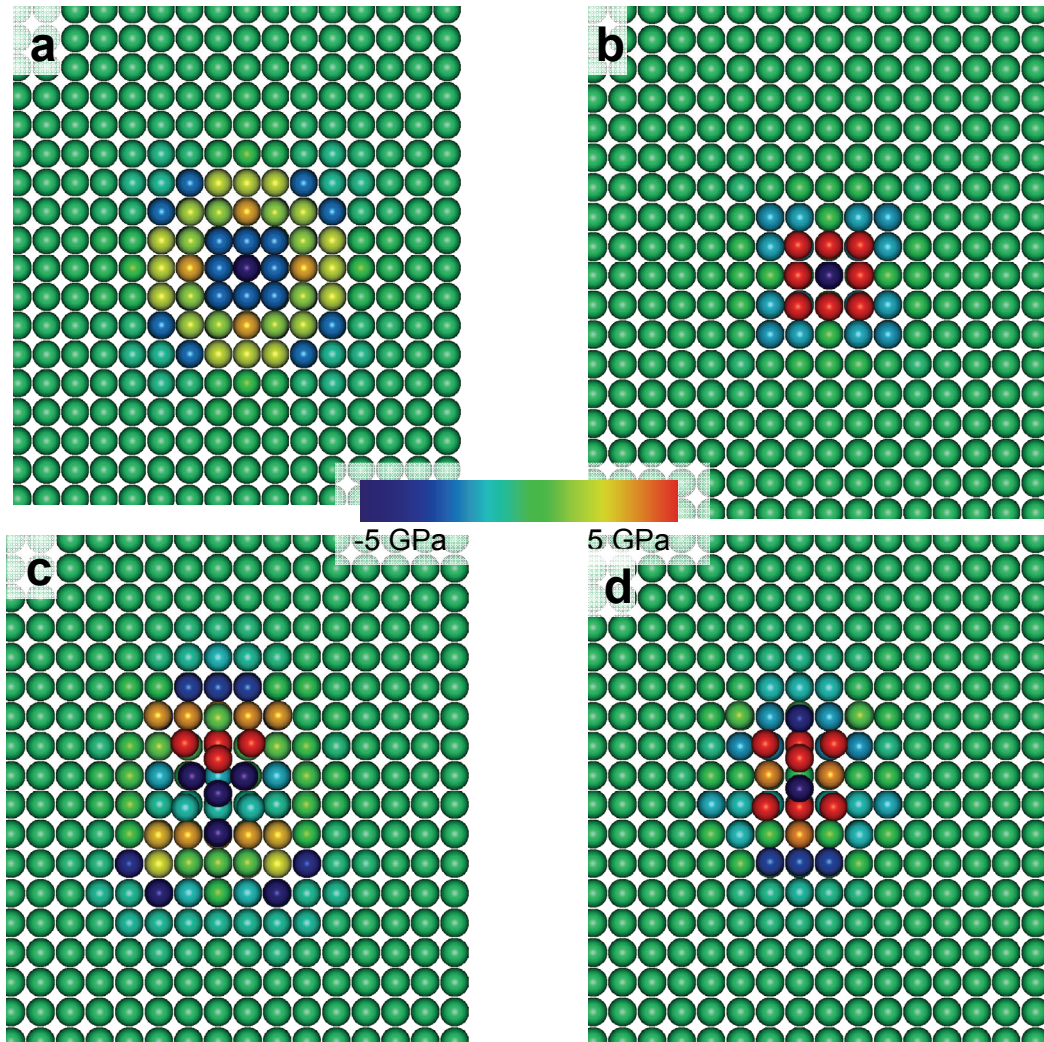


Figure 3.9 Pressure field of the substitutional (a and b) and the [100]-dumbbell interstitial (c and d) for the first (a and c) and the second (b and d) potential.

4 Results on applications

4.1 Application I - Nanocrystalline structures

4.1.1 Motivation

The Materials Science and Simulation group at Paul Scherrer Institut¹⁰⁷ is well known for their work on MD simulations of fully three-dimensional nc metals. These structures have provided insight into deformation mechanisms and especially into details of dislocation/GB interactions in fcc metals⁶¹⁻⁷² as it is mentioned in the introduction (section 1.2.2). Important here is the fact, that dislocations which have been nucleated in GBs can be temporary pinned at GB ledges and their associated stress intensities during propagation^{66, 70} which also changes the macroscopically observable stress-strain behavior.

In this section, impurities are incorporated to three-dimensional nc structures to model the nc samples in a more realistic way. The local chemical potential approach and the first EAM potential described in chapter 3 are applied to simulate a dilute O concentration in GBs of nc samples. From experimental data it is expected that a difference in the macroscopic stress-strain behavior would be observed. In the microstructure a change in the dislocation propagation behavior, e.g. an additional pinning due to O impurities in GBs is expected.

4.1.2 Sample description and simulation details

Two nc Al samples containing 15 grains are used as pure initial structures. Both samples are produced using the Voronoi technique, MS relaxations and a room temperature equilibration procedure according to Ref.¹⁸⁵. The smaller sample consists of 101384 Al atoms and has 15 grains with 5nm mean size. It is called “test sample” as it is used to perform test runs for the larger MD simulation. The larger sample consists of 1223250 Al atoms and has 15 grains with a mean size of 12 nm. The impure version of this sample is the main focus of interest and is therefore called “main sample”. The pure version of the 12 nm grain sizes sample serves as a reference for the impure simulation, consequently it is called “reference sample”. The test sample is deformed under uniaxial tension with a strain rate of 10^9 s^{-1} to provide information for the preparation of the large sample in a rapid way. All the simulations for test or reference purposes and the final simulation of the main sample are performed at 300 K temperature using the first EAM potential described in section 3.2.

To study the effect of the impurities, two distributions of O atoms are inserted into the test sample by substituting Al by O atoms. In the first distribution the O atoms are arranged as small clusters in triple junction lines between GBs. The distance between the clusters is chosen

sufficiently large to avoid interaction between the neutrally charged sub-regions during the charge update procedure. The selection of triple junction lines for the insertion of O is made on a random basis. In total 95 Al atoms are substituted by O atoms. This new impure sample is called “impure 1”. During the subsequent deformation of the “impure 1” sample the green stress-strain curve shown in Figure 4.1 is obtained. It coincidences with the curve for the pure test sample (Figure 4.1: the red curve) at strains smaller than 5% and higher than 10%. For the interval from 5% to 10% strain, there is some divergence between the curves.

It is known from former simulations⁶⁶ that the reference sample with a mean grain size of 12 nm will plastically deform by the propagation of dislocations which nucleate from the GBs. To enhance the effect of the impurities, a second O distribution is implemented to the test sample with the intention to affect the dislocation activity present in the test sample. For this purpose the simulation of the pure test sample is analyzed with a particular interest in the dislocation activity. To get a second sample with a more effective O distribution, O atoms are placed into the undeformed test sample by substituting clusters of Al atoms by O atoms in those triple junction lines which are either close to nucleation sites of dislocations or where dislocations pass during their propagation in the pure sample. In total 37 Al atoms are substituted by O atoms. The sample is called “impure 2”. The deformation of the “impure 2” sample revealed that the global stress-strain behavior (see Figure 4.1: blue curve) can be modified using this approach.

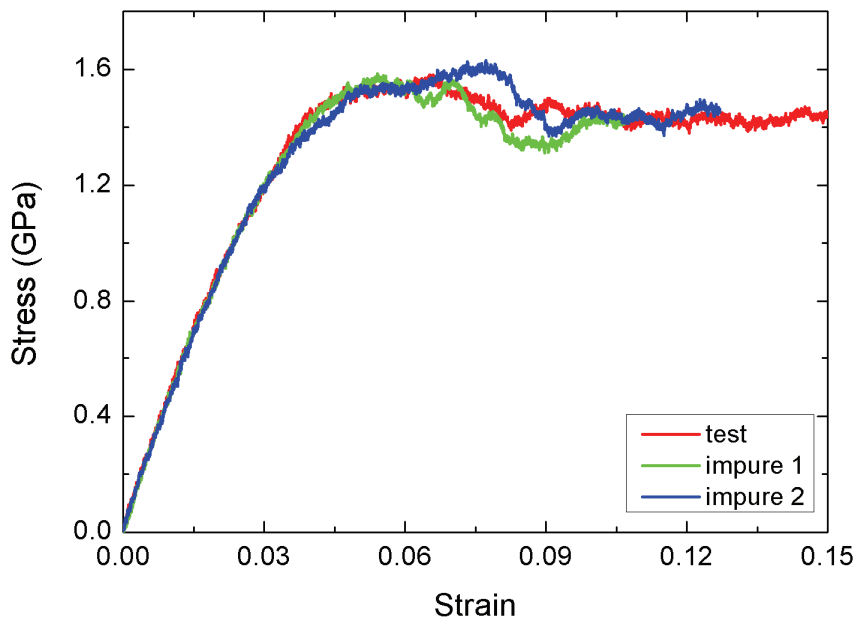


Figure 4.1 Stress-strain curves for the test sample (red) and the two impure cases: “impure 1” with 95 randomly distributed O atoms (green) and “impure 2” 37 O impurities distributed with knowledge of the dislocation behavior in the test sample (blue).

Before O atoms are added to the pure (reference) sample to create the main sample, again the pure sample is deformed using the potential published in Physical Review B ¹⁷⁸ to create a reference. The reference sample is deformed at the same strain rate as the main sample: 10^8 s^{-1} . After a total elongation of 16% the simulation is stopped. As previously mentioned, the simulation temperature is 300 K. Visual inspection of configurations of the reference simulation are used to insert O atoms at the triple junctions with “higher dislocation activity” analogously to the “impure 2” sample. O atoms are introduced in the undeformed sample by substituting Al atoms in clusters of 1 to 17 atoms. During the substitution of Al atoms, care is taken that the groups of O atoms have distances between each other which are larger than twice the cutoff of the constrained region in the charge optimization. The reason for this is that regions which are closer than this limit count as one in the cluster algorithm of the charge determination (see section 3.1.6 on the implementation of the local chemical potential approach). If the distances are maintained, the largest profit from distributing neutrally charged sub-regions to different nodes of the parallel computer can be made. The main sample contains totally 179 O atoms. After production, the sample is relaxed using MS and then equilibrated at 300 K using MD. A section through the sample is displayed in Figure 4.2.

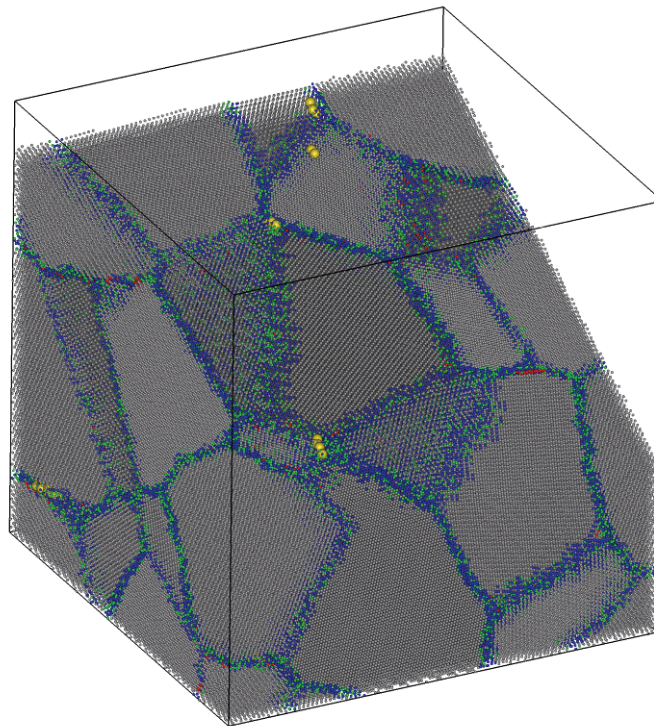


Figure 4.2 Section through the large simulation sample. The local crystallinity coloring is used to visualize the grains and the GB. Yellow spheres indicated O atoms.

After the preparation procedure, the main sample is deformed at a strain-rate of 10^8 s^{-1} to approximately 6.5% strain. At this strain the simulation is stopped because of two atoms which

moved to close to each other. If two atoms are closer than a certain threshold the charge update automatically stops the simulation. This threshold is typically much smaller than the average distance between atoms in the fcc arrangement. Apparently for two atoms it is possible to move closer than this threshold due to the randomness in the atomic structure of the triple junction and probably due to weaknesses in the description of the atomic interaction with the given potential: The first potential described in section 3.2. This could be avoided by modifying the short-range interaction of the potential by adding a strongly repulsive term.

4.1.3 Results

4.1.3.1 Deformation of the sample: Global response

The comparison between the stress-strain curves (Figure 4.3) for the uniaxial deformation of the pure “reference” and the impure “main sample” shows some divergence. In both cases discrete stress drops are visible. They match with plastic events in the microstructure, i.e. propagating dislocations. Remarkable is the fact that the stress at 6% strain is significantly higher in the impure case than in the pure case. In the visual inspection of the samples it is seen that in the main sample there is dislocation activity around 5.7% strain which causes the large drop. Before 6% strain the dislocation activity disappears with the exception of to slip events at 6.1% and 6.4% strain. The stress-strain curve shows the corresponding behavior: the stress increases for the strain interval without dislocation activity and shows two discrete drops for the mentioned slip events. In the reference sample, the dislocation activity is different and various slip-events are observed between 5.7% strain and 6.2% strain: The stress is more or less continuously decreasing in this range of strain. After this no more dislocation activity is observed and the stress increases. So the difference between the stress-strain curves can be rationalized by differences in the dislocation activity. However it is difficult to correlate the dislocation activity or its absence to the presence of impurities. For this purpose, two dislocations which appear at similar strains in the same grain are compared. This is described in section 4.1.3.2. Connected to the sudden stop of the simulation due to atoms which inhibit further charge update, it remains unclear whether the flow stresses at higher strains would be of the same value.

Although dislocation activity is a rather stochastic process in these nc samples, at the onset of plasticity dislocations appear for both cases in the same grains. These “early” dislocations use slip planes which are parallel and they even nucleated in the same GB regions. In the continuation of the deformation of the samples it becomes more difficult to compare internal processes. This can also be seen from the stress-strain curves which clearly diverge above 5.9% strain. As described above more and more slip-events are observed only in one of the two samples. Each event, e.g. nucleation or propagation of dislocations, causes changes in the

microstructure. Summing up these changes during the continuation of the simulation, the samples become more and more different from each other and less comparison based on local processes is possible.

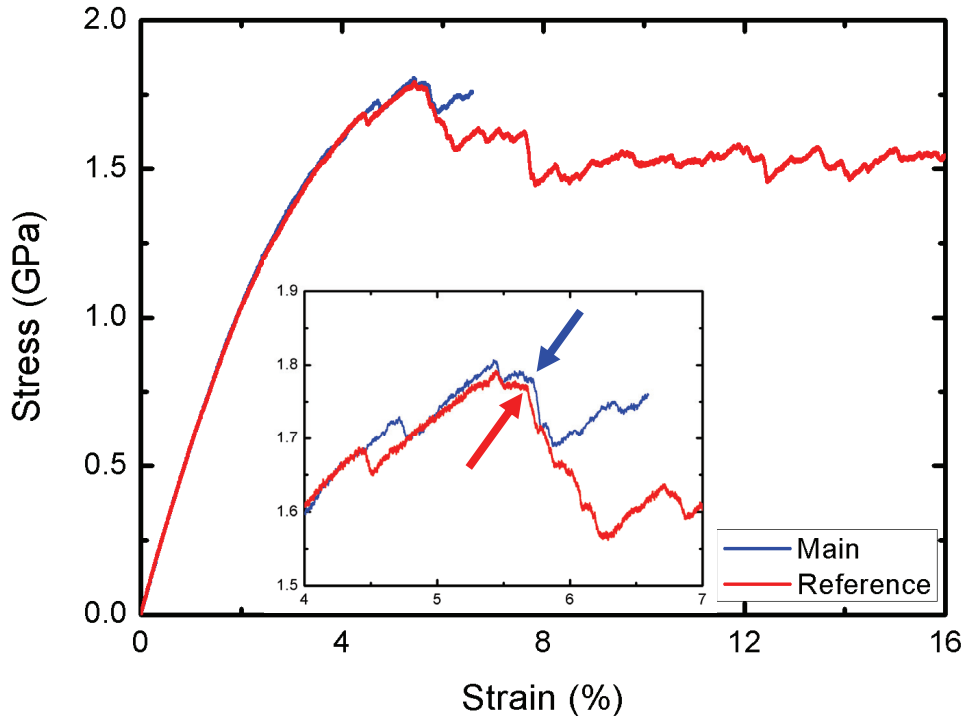


Figure 4.3 Stress-strain curves for the large simulation samples: The reference sample (red) and main sample with 179 substitutional O impurities (blue). The red and the blue arrow mark the position in the stress strain curve where the dislocation analyzed in 4.1.3.2 nucleates.

For a deformation around 6% strain, hardly any grain growth is visible in the samples. Therefore it is impossible to study the effect of the impurities on the grain growth in the main sample.

4.1.3.2 Difference in dislocation behavior

A difference between the reference and the main simulation is observed for a dislocation which exists in both samples in the same grain. In both cases the leading partial nucleates at about 5.7% strain.

Pure case

The process described here is visualized in Figure 4.4: In the reference sample the leading partial nucleates rapidly where the red arrow is drawn in the stress-strain curve (Figure 4.3). The leading partial is propagating through the grain in about five picoseconds simulation time. As soon as the leading partial has reached the opposite GB a new partial dislocation nucleates in the same GB region as the previous on an adjacent plane. With the propagation of the second partial

a micro-twin is formed. With increasing deformation of the reference sample more partial dislocations propagate through the sample and the twin migrates. The twin fault remains in the sample until the end of the simulation.

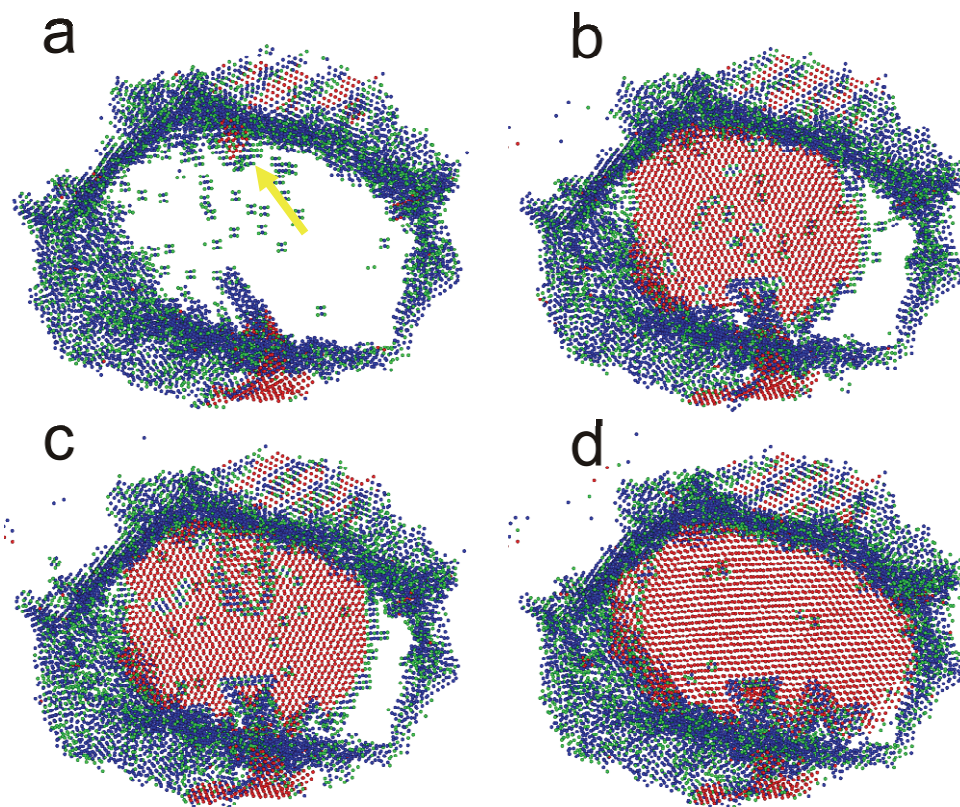


Figure 4.4 Dislocation propagation in the reference sample. Atoms are displayed in local crystallinity classes without displaying fcc atoms. The arrow in the image (a) points to the nucleation site of the leading partial dislocation. The leading partial propagates through the grain (b), a second partial dislocation nucleates at nearly the same position as the first (c). This creates a twin fault which remains in the sample (d) and increases in size during the simulation. The whole process described here happens in less than 10 ps.

Impure case

In the main sample three clusters of O impurities are distributed in triple junctions facing the grain of interest (Figure 4.5a). It is observed that the nucleation of the leading partial dislocation is more difficult: During 30 ps, the leading partial dislocation tries in several attempts to detach from the GB to propagate through the sample. After propagating away from the nucleation site, the leading partial dislocation is stopped, i.e. pinned at an O cluster sitting in the neighboring triple junction line, for about 50 ps. After unpinning the leading partial propagates through the entire grain. During the propagation time a twin fault starts to be nucleate at about the nucleation site of the previous partial dislocation. As soon as, the first leading partial dislocation

reaches the GB at the opposite side of the grain a trailing partial is formed in this GB. This trailing partial sweeps away the entire dislocation and the twin fault.

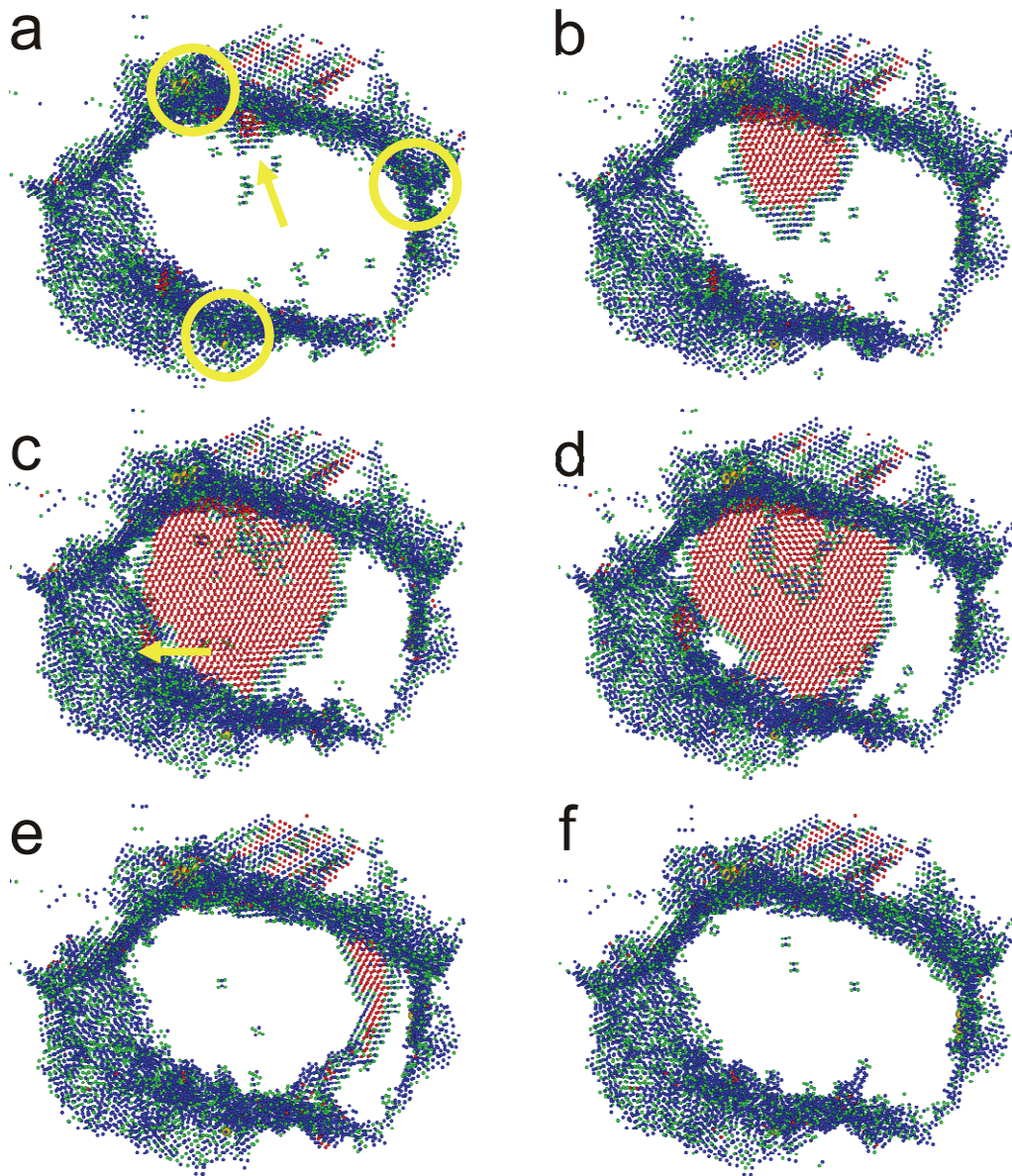


Figure 4.5 Dislocation propagation in the main sample (impure case). Atoms are displayed in local crystallinity classes without displaying fcc atoms. Yellow circles indicate the position of the O clusters in the GB. The arrow in (a) indicates the nucleation site of the leading partial dislocation. It takes about 30 ps until the leading partial dislocation starts to propagate. Afterwards the leading partial requires additional 25 ps to pass one of the O clusters (b). In (c) the nucleation of a second dislocation is seen which creates a twin fault. Additionally a trailing partial is nucleated at position indicated by the yellow arrow. The trailing partial sweeps away the stacking fault and the twin fault (d + e). After all, the whole dislocation is removed in the sample (f). The entire processes starting from the first nucleation attempts until the dislocation completely disappears, takes about 70 ps.

Comparison

Two main differences are observed: Firstly, the dislocation (Figure 4.5) nucleates and propagates in the main sample (impure) much slower than in the reference sample (pure) (Figure 4.4) and secondly, the dislocation is entirely absorbed in the surrounding GB of the main sample whereas it remains in the grain as a micro-twin in the reference sample.

There are different aspects which complicate the picture and have not been considered yet:

1. The dislocations in the two cases are sliding on parallel slip planes however one is two atomic layers above the other. Consequently, both dislocations will interact with different structures in the neighboring GBs.
2. Other dislocations have nucleated and propagated in both cases before the discussed dislocations appear. Actually, there is a dislocation in the pure case (reference) which uses the very same slip plane as the one in the impure case (main sample). This dislocation nucleates at 5% strain, propagates very quickly and disappears in the opposite GB 10 ps later.
3. In both cases the interactions of the dislocations with the neighboring GB structures are complicated. Stair-rod dislocations are observed at the GB region where the trailing partial nucleates. This might be linked to attempts for cross-slipping.
4. The competing mechanisms, twin fault vs. propagation of the trailing partial, in the impure case complicates the situation additionally.

In summary, there are differences between the pure and the impure sample, such as the speed of dislocation nucleation and/or propagation and the stability of the twin fault. It is however difficult to pin down the exact role of the O impurities because there are other differences e.g. the different history of the two samples or the different slip plane which impede a direct comparison between pure and impure cases.

4.1.4 Discussion

The results in section 4.1 show that the difference in the global response to the deformation is rather small. No significant changes in the mechanical properties due to the O impurities have yet been observed. Especially, the magnitude of change is different from experiments e.g. the one reported by Gianola in Ref. ⁵³. Maybe the approach of putting the O atoms into triple junctions between GB regions where dislocation activity is seen in the reference sample is not powerful enough to influence the dislocation nucleation and mobility in a significant way. However test simulations performed on the smaller sample (5 nm grain size) at a ten times higher strain rate show that completely random O insertion gives a smaller effect than using a distribution based on the knowledge of the dislocation activity in the pure case (see Figure 4.1).

The nc samples are the most complex systems studied here. Determining the influence of the O impurities in them is difficult. First of all, the effects arising from the impurities have to be separated of other sources of differences. Especially the thermal noise has to be filtered to obtain a meaningful comparison between pure and impure cases as all the atoms have slightly different trajectories in the two cases due to the finite temperature. Instead of separating effects for single events, a comparison on a statistical basis could be envisioned. As soon as many simulations with varying O content in the GB are available, it is possible to find qualitative models which link the mechanical behavior and also dislocation activity with the impurity content. Alternatively, simulation of larger samples with many grains could also increase the number of observed events to produce statistical trends. However, the production of many or larger samples, their simulation and analysis is demanding.

4.2 Application II – Dislocation propagation

4.2.1 Motivation

The computational burden of an nc simulation is very large. Therefore only one distribution of impurities has been simulated in the large sample with more than a million Al atoms. A smarter simulation geometry where several impurity distributions can be tested should give access to the effect of impurities on dislocation pinning, propagation and absorption. For this purpose, a sample which contains a grain with one well-defined dislocation is several times tested under shear deformation by introducing different O impurity distributions.

4.2.2 Sample description and simulation details

The simulation sample (Figure 4.6) was produced by Christian Brandl who isolated a single grain with a surrounding buffer of atoms from a large nc simulation by cooling it down to 0 K using a MS relaxation. The isolated grain contains a perfectly nucleated dislocation which is pinned at both ends at the GB. Some atoms of the buffer around the grain are fixed because of the free surface. During the construction of the sample, the local coordinate system was aligned with the Burgers vector of the dislocation parallel to the x axis and the slip plane of the dislocation as a xy plane (perpendicular to the z axis).

Christian Brandl shear deformed such samples to determine the athermal stress barrier for dislocation pinning. The loading of the sample was done in discrete increments of shear strain with relaxations in between. The stepwise shear deformation was applied in xz direction using affine transformations. Brandl used a fast conjugate gradient scheme for the intermediate relaxation. Here, the loading is performed in the same direction. The increments of shear strain

are 0.1% until the dislocation unpins and propagates for the first time through the sample. Then, the last stable configuration is shear deformed by an increment which is one magnitude smaller (0.01%) and the procedure is repeated. The smallest increments of shear deformation, which are applied, are 0.001%. For the relaxation, the more time consuming MS relaxations is used, because the variable charge method has not yet been implemented into the conjugate gradient code. A benefit of the MS method is the physical trajectory of atomic motion which is tractable during the energy minimization process.

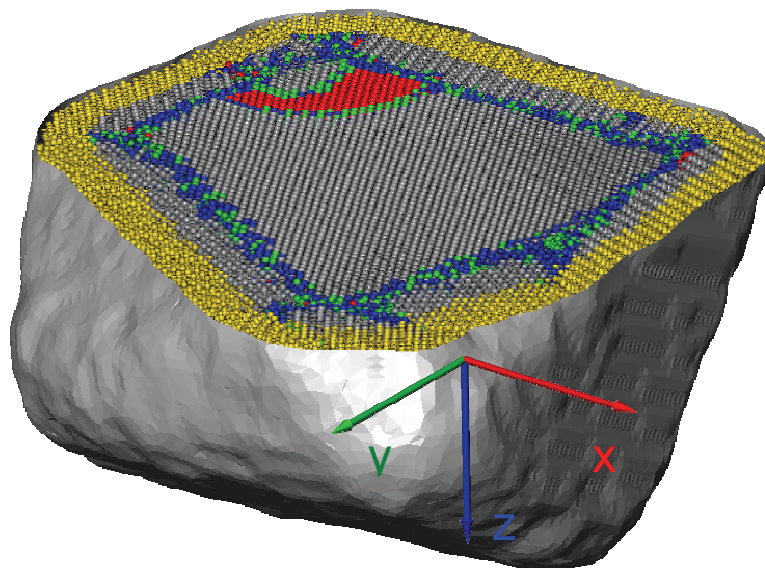


Figure 4.6 Cut through the initial sample produced by Christian Brandl. The free atoms are colored according to their local crystallinity class. The yellow atoms are static (and not O atoms) during the relaxation. The coordinate system is aligned in the following way: x axis (red) parallel to the Burgers vector, z axis (blue) normal to the slip plane and y axis accordingly to form a right system. Image produced by Christian Brandl.

Boundary conditions and simulation parameters during each relaxation and among the different O distributions remain unchanged. The sample is always simulated with free surfaces and a static shell of atoms (yellow atoms in Figure 4.6). The static atoms are used to maintain the sample geometry and the external load. The time-step in the MS integration is kept at 1 fs and charge update is done in every step. During the molecular static relaxation the global quench condition is used which means that the velocities of the atoms are removed as soon as the kinetic energy in the system decreases. As interatomic potential both versions described in section 3.2 (**First potential**) and 3.3 (**Second potential**) are applied. This means, the Al-Al interaction is simulated with the spline version of Mishin and Farkas potential ¹⁷⁸, which is different from Brandl, who used the analytical version of Mishin and Farkas potential ¹⁸⁶. Therefore, prior to the first deformation a MS run is performed to relax the pure configuration

because of the different potentials. MS simulations are terminated when the kinetic energy curve shows only statistical fluctuations which are of order 10^{-14} eV.

Several impure configurations are produced to investigate the influence of O impurities. They will be described in the results part. For each impure sample there is MS relaxation after its production, i.e. before it is deformed for the first time.

4.2.3 Results

4.2.3.1 Pure

First potential

Using the first potentials for the shear deformation of the pure sample the following results are obtained: The pure sample (Figure 4.7) can be sheared up to 0.35% additional strain without unpinning of the dislocation.

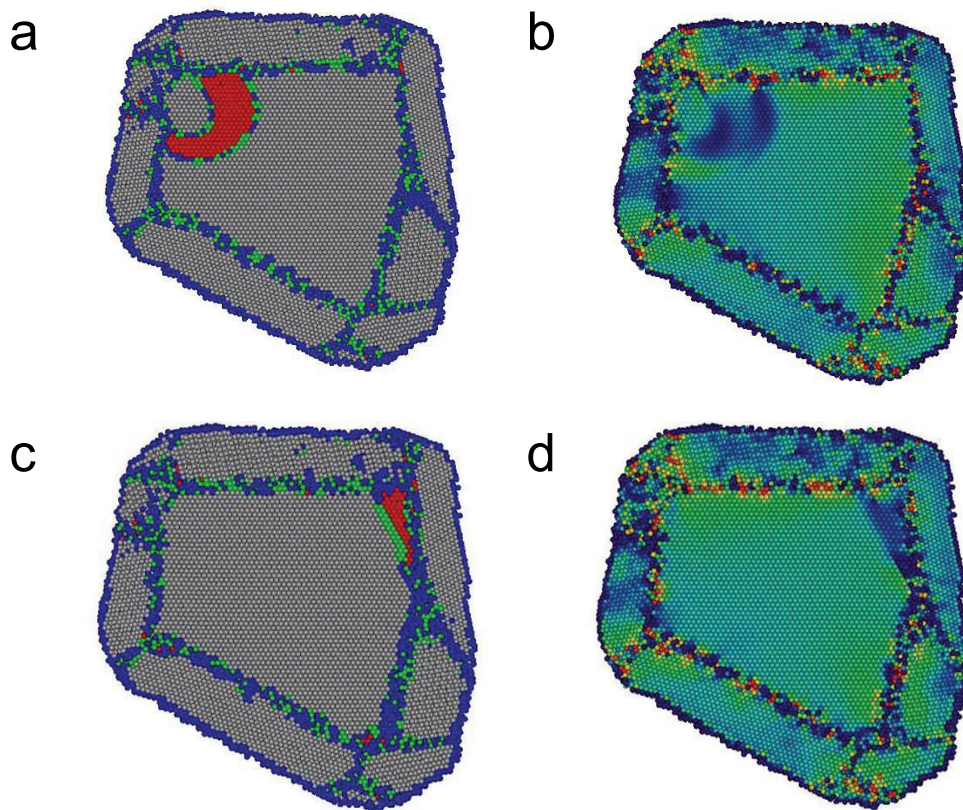


Figure 4.7 Cut through the pure sample in the initial (a) and (b) and in the final (c) and (d) configuration. (a) and (c) show the local crystallinity class coloring and (b) and (d) show the hydrostatic atomic pressure. Colors are between -1 GPa (tensile) in blue up to +1 GPa (compressive) in red according to Figure 3.6b. The dislocation is pinned at two pinning points: the upper pins the edge segment and the lower the screw segment.

During the deformation in discrete increments the dislocation curvature is increased with increasing strain. Up to strain of 0.35%, the shear stress is linearly increasing to a value of 232 MPa (Figure 4.13). If the shear strain is increased further, the dislocation unpins simultaneously at both pinning points (edge and screw side), propagates through the entire sample and is absorbed in the neighboring GB network. After the propagation, only a small left over of the dislocation is visible in one corner of the grain (see Figure 4.7c). Visual inspection of a series of configurations outputted during the relaxation shows no more obvious pinning points during the propagation with the exception of the final structure.

The evolution of the kinetic energy during the relaxation (Figure 4.8) reveals that atoms start to be mobile after unpinning which can be seen in the increase of the kinetic energy. At a certain point the kinetic energy drops to zero. At this point the global quench condition is fulfilled. The system is at a stationary point and has to “climb up hill” in terms of potential energy if the displacement direction of the atoms is not changed. The drops in kinetic energy are also noticeable in the shear-stress evolution curve in the form of kinks. The final shear stress after the relaxation is found to be 122 MPa. The effect of the “global quenching” is discussed within the general discussion on the method chapter 5 (see section 5.1.1.2).

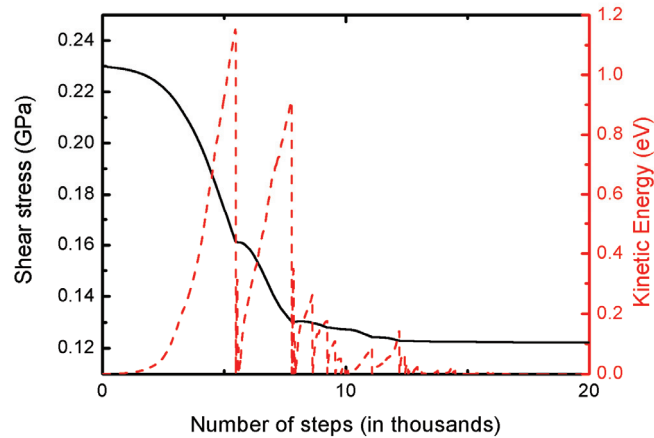


Figure 4.8 Evolution of the kinetic energy (red, dashed) and the shear-stress (black, solid) during the molecular static relaxation.

Second potential

The same things are observed when the second potential is used because the Al-Al interaction does not change between the two potentials (for both potentials Mishin Farkas Al potential¹⁷⁸ is used). The dislocation is pinned up to 0.35% strain. Up to this point it bows out more and more with increasing strain. Finally, it unpins at 0.351% strain. It is observed that the dislocation unpins at both pinning sites (edge and screw component) simultaneously. During the visible

inspection no change in the propagation behavior, e.g. a drag, can be seen. In the end the major part of the dislocation is absorbed in the GB as Figure 4.7 has already shown. The propagation behavior of the dislocation in terms of kinetic energy and shear stress evolution is identical with the one displayed in Figure 4.8.

4.2.3.2 Oxygen substitutions in the grain boundary

First potential

In four cases a few Al atoms are substituted by O atoms. The different structures are shown in Figure 4.9. The O substitutions are always done in or around the slip plane of the dislocation. The O impurities are substituted in the pure sample which has been deformed to 0.3% additional strain. After this all the samples are relaxed at the given strain using MS and then shear strained by another 0.1%.

During the relaxation at 0.1% additional strain the dislocation unpinned and propagated through the entire grain. In the visible inspection, the pure configuration has not shown much interaction between the propagating dislocation and neighboring GBs. The same is true for all cases with substitutions in GBs. Only in one case (GB-S3), it is observed that the trailing partial of the edge segment of the dislocation is slightly dragged by the impurities (Figure 4.11). Still, the dislocation overcomes the clusters of O atoms with ease in any of these cases. To quantify the effect of the drag at O impurities the evolution of the shear stress during the relaxation is compared to the pure case (Figure 4.10).

In case GB-S1, the shear stress drop curve diverges from other impure and pure cases. The deviation from the other curves indicates that the quench condition is fulfilled earlier than in the other cases. This can mean that a pinning at an obstacle such as a cluster of O in the GBs is present. However it is not possible to find visual evidences which prove this speculation as too few configurations are outputted during the run to resolve this possible pinning event.

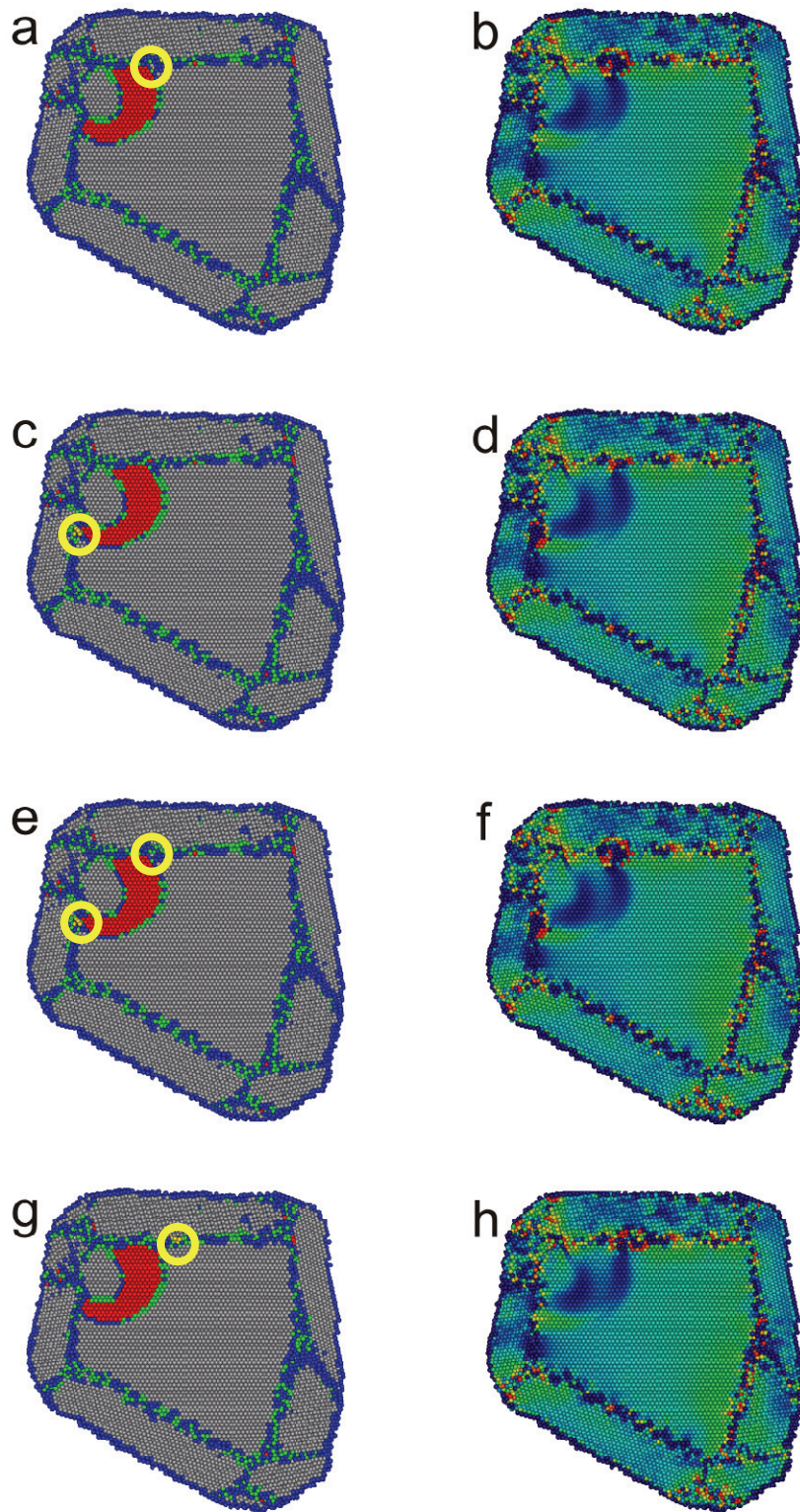


Figure 4.9 The four cases with substantial O impurities in the GB. Left hand column shows the local crystallinity class and the right hand picture shows the pressure field according to Figure 4.7. Number of O impurities is 10 in case “GB-S1” (a+b), 7 in case “GB-S2” (c+d), 17 in case “GB-S3” (e+f) and 6 in case “GB-S4” (g+h). The yellow circles indicated the position of the O substitutions.

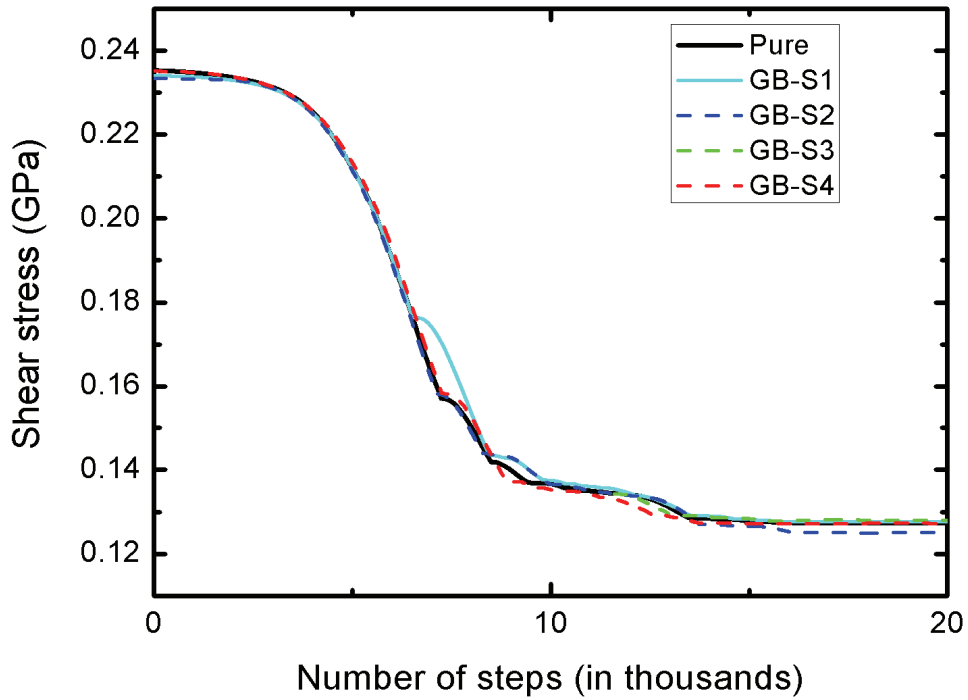


Figure 4.10 Shear stress evolution during propagation of the dislocation in the pure and the four impure cases described in Figure 4.9. The curves are shifted along the step axis to have the onset of the propagation at the origin. The onset of the drop in shear stress is shown until a plateau is reached again. This corresponds with the number of steps required of the propagation of the dislocation.

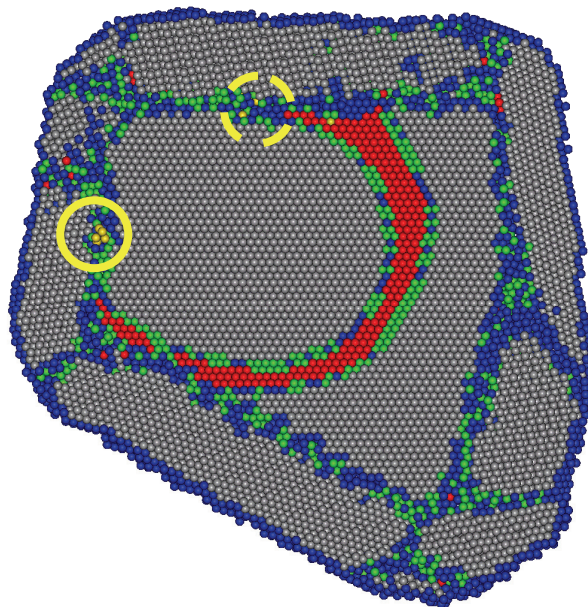


Figure 4.11 Propagation in case GB-S3: the trailing partial of the edge segment of the dislocation is dragged by an O cluster in the grain boundary (dashed circle). The screw segment entirely passed the cluster near its original pinning point (solid circle).

4.2.3.3 Interstitial oxygen in the grain boundary (edge part)

First potential

To emphasize the effect of impurities, a larger number of O atoms are tested as interstitials in the GB. For this purpose, 28 O atoms are added near the pinning site at the edge segment of the dislocation. The O atoms are inserted close to the dislocation and ahead of it so that the propagating dislocation has to overcome all these atoms to reach the GB in which it is absorbed. The O atoms are not only added to the slip plane but also few atomic planes above and below of it predominantly around the existing ledge structure in the GB.

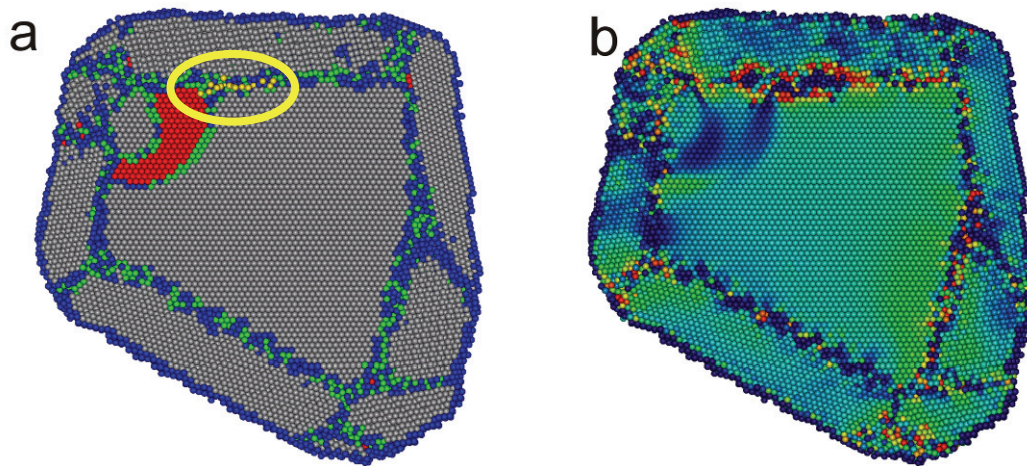


Figure 4.12 The initial sample “GB-Ie1’ with the 28 O impurities as additional atoms in the GB.

For the deformation of the impure sample it is remarkable, that the dislocation is still pinned at a shear strain of 0.4%, where the dislocation has propagated in all structures investigated, so far. After a few more runs it turns out that the dislocation is pinned up to a shear strain of 0.55%. The critical shear stress needed to unpin the dislocation increases from 232 MPa to 244 MPa (see Figure 4.13).

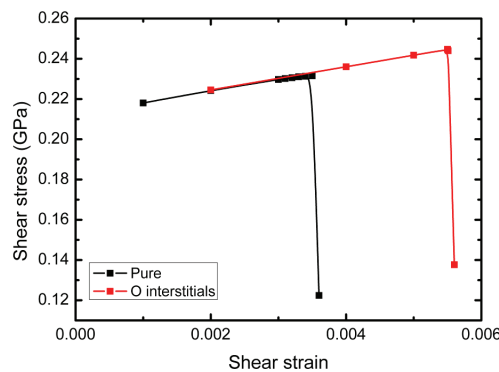


Figure 4.13 Shear strain-stress curves for the pure case (black) and the case of 28 O impurities additionally inserted to the GB (red).

Second potential

Different O arrangements in the GB are tested using also the second potential. Three clusters of dilutely distributed O atoms are inserted near the edge segment of the dislocation. In all cases the O impurities are added in the undeformed pure sample. The configurations are presented in Figure 4.14.

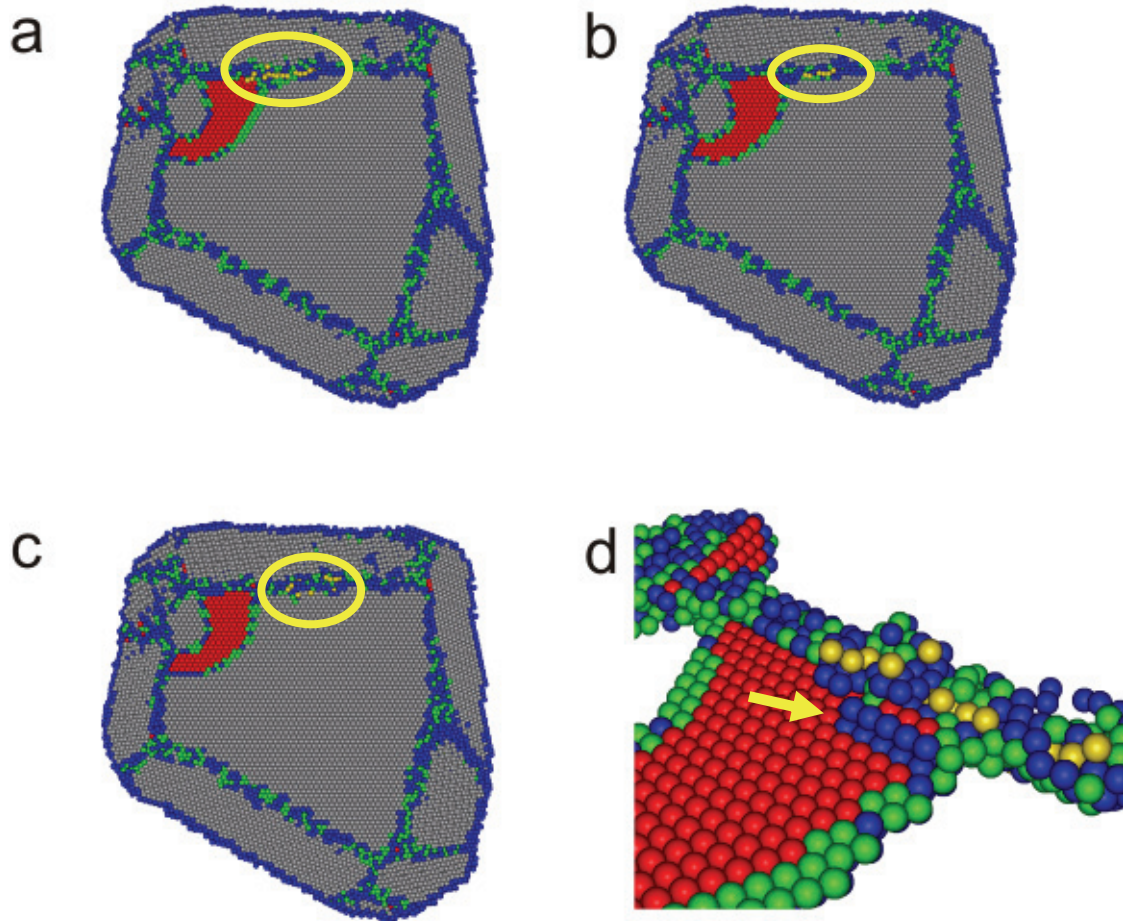


Figure 4.14 Initial structures with a dilute O distribution as interstitial atoms in the GB at the edge segment of the dislocation. The number O atoms is 28 in case “GB-Ie1” (a), 11 in case “GB-Ie2” (b), 15 in case “GB-Ie3”. (d) shows a magnification of the dislocation at the impurities in case “GB-Ie1” without displaying fcc atoms. After the relaxation, the dislocation has a step structure (yellow arrow) at the impurities. The local crystallinity color-code is used.

The structure in Figure 4.14a (GB-Ie1) is the same as the one in Figure 4.12. The pressure field due to the O impurities changes to more compression if the potential is changed from the first to the second (see Figure 4.15). The highly compressive pressure in case of the second potential could be a reason why the dislocation has a step structure (Figure 4.14d) at the impurities after the first relaxation without any deformation of the sample. This step structure consists of a few atoms at the GB which are one atomic layer higher than the initial slip-plane. The mechanism

which creates this step is unclear. The dislocation propagates in the same way as in the previous cases however the steps structure at GB remains and propagates with the dislocation.

The O atoms simulated in GB-Ie2 (Figure 4.14b) are a subset of the O atoms simulated in GB-Ie1.

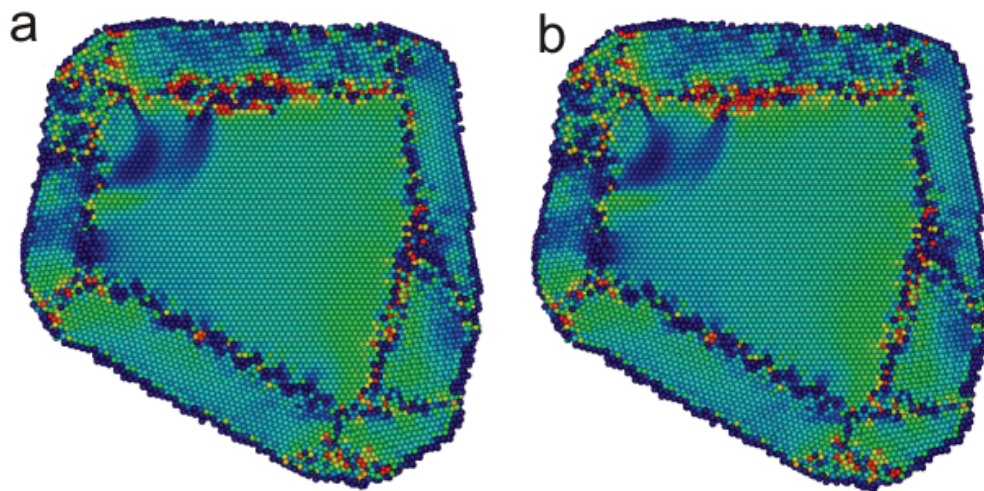


Figure 4.15 Pressure field of “GB-Ie1” for the first (a) and the second (b) potential.

All the three samples are stepwise deformed according to the procedure described in section 4.2.2 to obtain a critical value for the strength of the pinning points under the presence of impurities in the sample. Table 4.1 lists the values of critical shear strains and stresses. The strains are those of the last stable structures before the dislocation unpins with further strain increment.

Case	# O impurities	Critical shear strain	Critical shear stress
Pure	0	0.350%	232 MPa
GB-Ie1	28	0.012%	220 MPa
GB-Ie2	11	<0.2%	235 MPa
GB-Ie3	15	0.340%	232 MPa

Table 4.1 Samples according to Figure 4.14: The number of O impurities and the critical shear strains and stresses for which the dislocation is still pinned are shown.

The dislocation in GB-Ie1 unpins after little additional shearing using the second potential. This fact can be rationalized by the step structure of the dislocation near the impurities. Also in case GB-Ie2 where the impurity atoms are a subset of those in GB-Ie1 the dislocation unpins at a much smaller strain as in the pure case, i.e. less than 0.2%. If the O impurities are placed a bit

further away (GB-Ie3) the critical shear strain increases to 0.34%. Although this is a higher value than in cases GB-Ie1 and GB-Ie2 it is not as high as the one of the pure case (0.35%). In summary, all the three cases show less dislocation pinning than the pure case, using the second potential. This is different from the first potential where the case GB-Ie1 shows significantly more pinning than the pure case.

4.2.3.4 Interstitial oxygen in the grain boundary (screw part)

Second potential

In this section, O interstitials are tested in the GB near the other segment of the dislocation, which is of predominantly screw character (Figure 4.16).

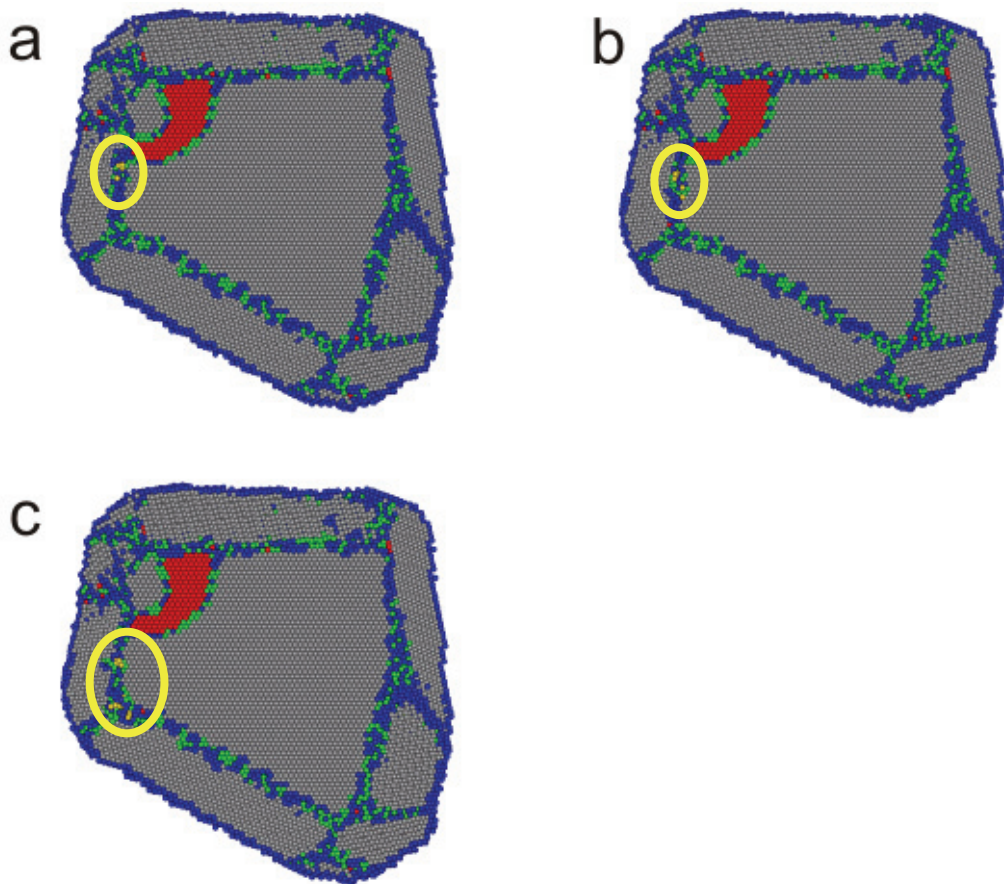


Figure 4.16 Initial structures with a dilute O distribution as interstitial atoms in the GB at the screw segment of the dislocation. The number O atoms is 4 in case “GB-Is1” (a), 6 in case “GB-Is2” (b), 15 in case “GB-Is3”. The local crystallinity color-code is used.

Shear deformation analogous to previous cases yields the critical shear strains and stresses given in Table 4.2.

Case	# O impurities	Critical shear strain	Critical shear stress
Pure	0	0.350%	232 MPa
GB-Is1	4	0.340%	231 MPa
GB-Is2	6	0.362%	232 MPa
GB-Is3	15	0.363%	231 MPa

Table 4.2 Samples according to Figure 4.16: The number of O impurities and the critical shear strains and stresses for which the dislocation is still pinned are shown.

The critical shear strain is again smaller (even smaller than the pure case) if the impurities are inserted too close to the dislocation. In case of a bigger distance to the existing pinning point the critical shear strains are increased. The corresponding critical shear stresses are 231 MPa for GB-Is1 and 232 MPa for GB-Is2 which is about the same as in the pure case. Obviously, those values are not significantly changed by the presence of the impurities and depend mainly on the critical shear strain which can be achieved before the dislocation unpins.

The propagation behavior of the dislocation, especially the drag effect due to O impurities is analyzed using the visual inspection of the series of configurations outputted during the run (see e.g. Figure 4.17). A drag can be seen in case GB-Is2 where the edge segment of the dislocation unpins of the ledge structure in the GB and the screw segment remains pinned for about 3000 MS steps longer at the O impurities (Figure 4.17). None of the cases shows cross-slip although the impurities interact with the screw segment of the dislocation.

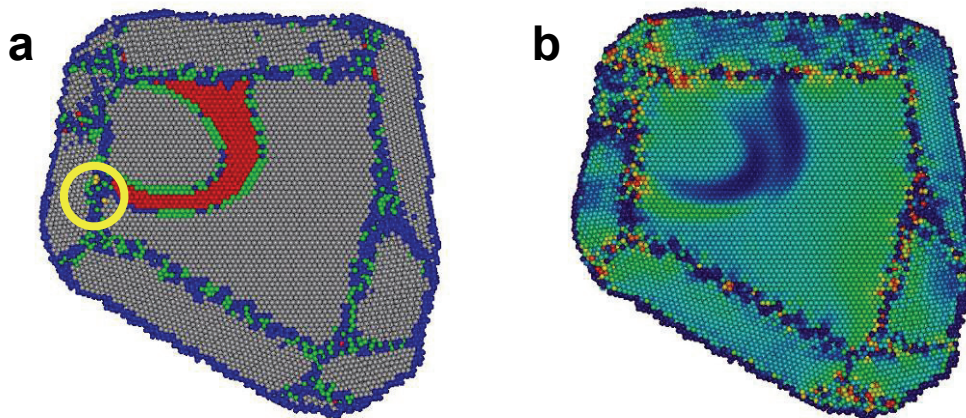


Figure 4.17 Case “GB-Is2” at 0.363% strain. The dislocation unpins at the edge part and remains pinned at the O impurities (yellow circle. (a) Local crystallinity class and (b) pressure field.

4.2.3.5 Interstitial oxygen in the grain boundary (absorption part)

Second potential

To check possible changes in the absorption behavior of the dislocation due to the O impurities, clusters of dilute interstitials are added to the GB at the absorption side of the sample according to Figure 4.18. For both cases a critical shear strain of 0.354% and a critical shear stress of 232 MPa are obtained which means that the dislocation is pinned longer at the existing pinning points than in the pure case.

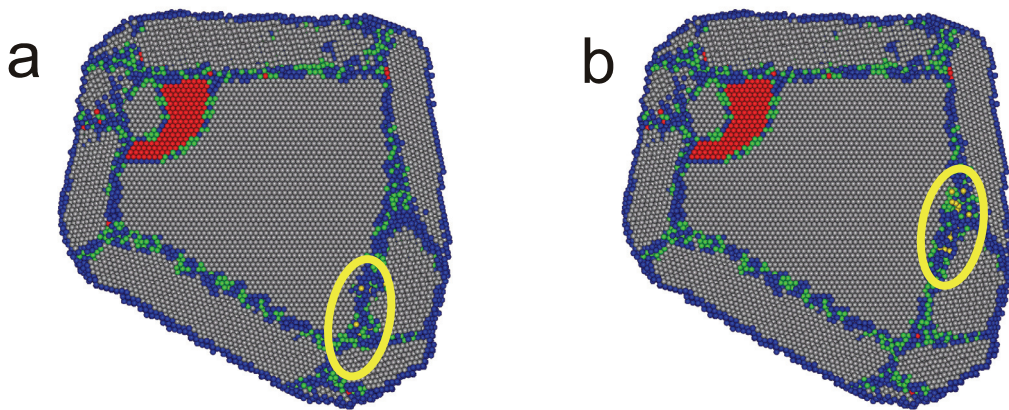


Figure 4.18 Initial structures with a dilute O distribution as interstitial atoms in the GB at the part where the dislocation is absorbed. The number O atoms is 10 in case “GB-Ia1” (a), 14 in case “GB-Ia2” (b). The local crystallinity color-code is used.

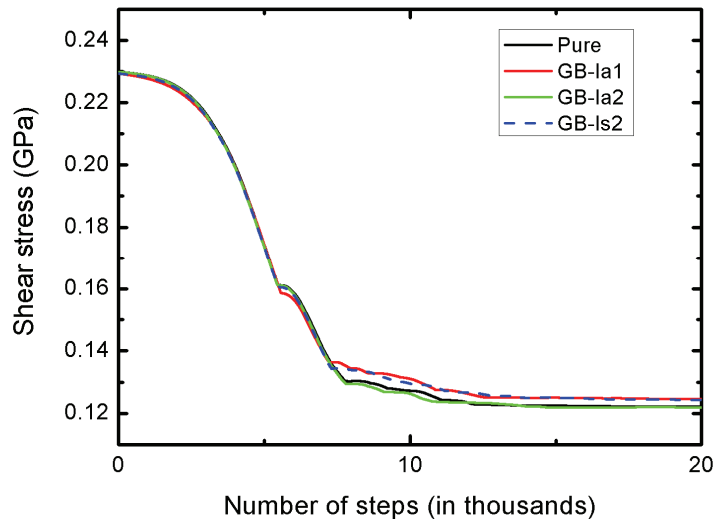


Figure 4.19 The drop in shear stress is followed for the pure and the three impure cases GB-Ia1, GB-Ia2 and GB-Is2. The curves are shifted along the step axis to have the onset of the propagation at the origin. More or less the onset of the drops is shown until a plateau is reached again. This corresponds with the number of steps required for the propagation of the dislocation.

The propagation and absorption behavior for both cases is visually found to be comparable to the pure case. This is also suggested by Figure 4.19 which shows the shear stress evolution during the propagation. However different levels of shear stress are obtained for the final structures. The difference is smaller than 5 MPa and is also found for other impure cases such as GB-Is2.

4.2.3.6 Al₂O₃ precipitates in the grain boundary

Second potential

Here, corundum precipitates in GBs are study in terms of pinning strength and dislocation propagation behavior. Six different samples are tested (see Figure 4.20). Al₂O₃ precipitates of diameter three angstroms are introduced by cutting out a sphere of the same diameter in the pure sample and inserting a commensurate spherical cutout of a larger corundum sample. In one case a larger precipitate of five angstroms diameter is introduced in the same way.

The shear deformation of the samples analogous to the aforementioned procedure yields the critical shear strains and stresses presented in Table 4.3.

Case	# O impurities	Critical shear strain	Critical shear stress
Pure	0	0.350%	232 MPa
GB-Ce1	7	0.316%	228 MPa
GB-Ce2	7	0.340%	231 MPa
GB-Cs1	7	0.266%	226 MPa
GB-Cs2	7	0.352%	231 MPa
GB-Cs3	36	0.323%	228 MPa
GB-Cb1	14	0.351%	231 MPa

Table 4.3 Samples according to Figure 4.20: The number of O impurities and the critical shear strains and stresses for which the dislocation is still pinned are shown.

It is observed that the critical shear strains are reduced if the precipitates are too close of the existing pinning points. E.g. cases GB-Ce1, GB-Cs1 and GB-Cs3 are lower in critical shear strain than the pure case. Moving the impurities further away leads to more pinning. Also, the trend that the pinning decreases more, if impurities are put into the GB at the edge segment, is maintained. In case of GB-Cs2 a slightly higher pinning than in the pure case is obtained. The larger corundum sphere (GB-Cs3) improves the small pinning strength of GB-Cs1 a bit. Obviously, there is more compressive stress due to the larger precipitate (see Figure 4.21).

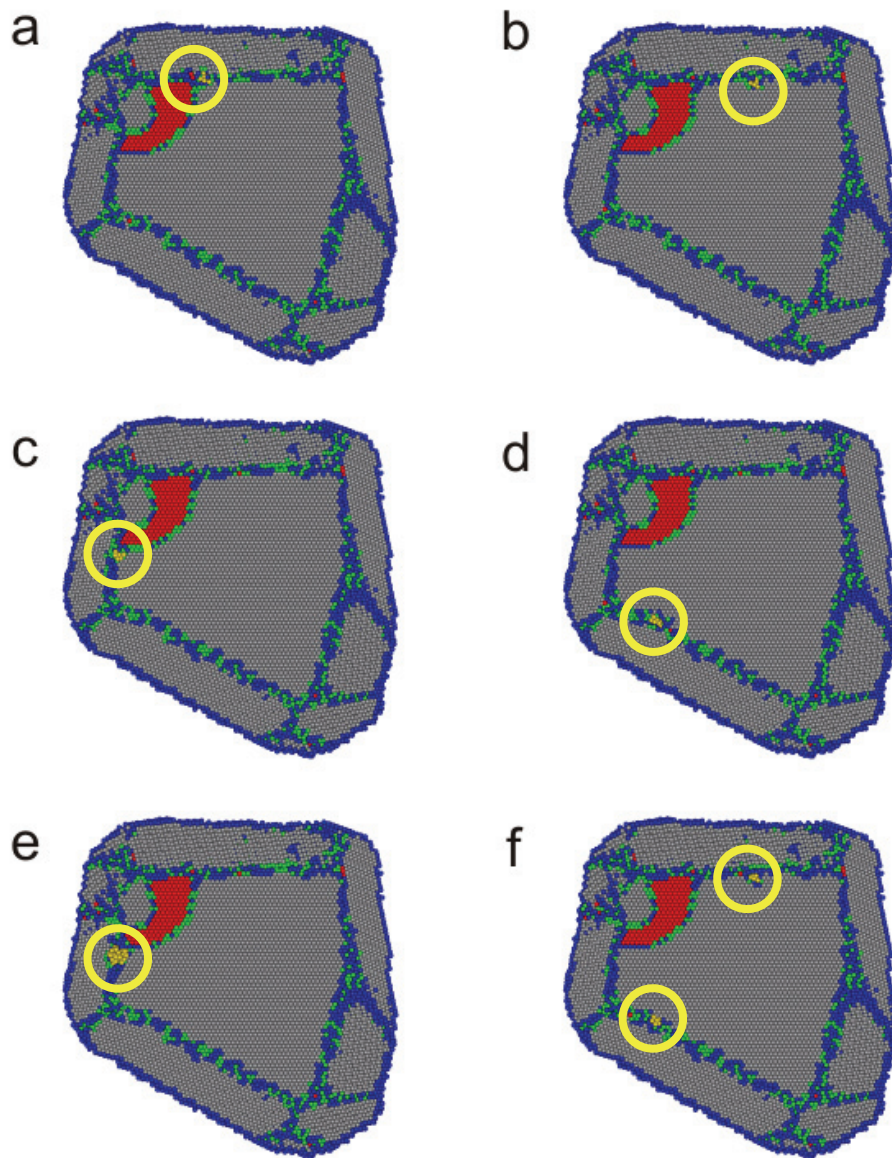


Figure 4.20 Structures with corundum precipitates. The number of O atoms is 7 in cases “GB-Ce1” (a), “GB-Ce2” (b), “GB-Cs1” (c) and “GB-Cs2” (d). In case of the large precipitate “GB-Cs3” (e) 36 O atoms are present and in the case of two precipitates (one at each side of the dislocation) “GB-Cb1” (f) twice 7 O atoms are present. The local crystallinity coloring is used.

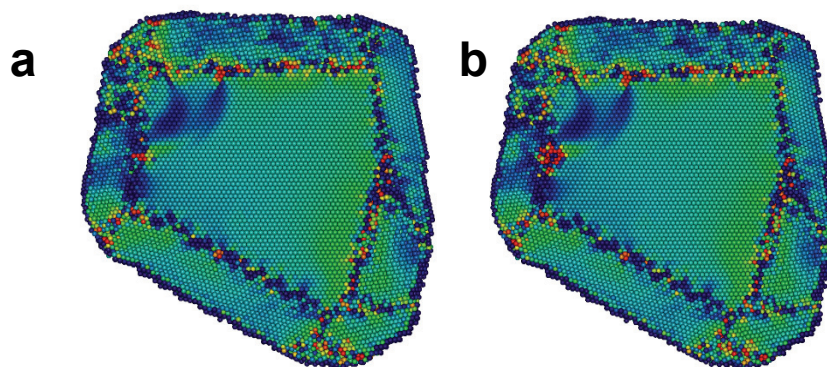


Figure 4.21 Pressure field of the corundum precipitates of cases GB-Cs1 (a) and GB-Cs3 (b).

The shear stress drop curves (Figure 4.22) reveal that there are changes in the propagation behavior. The difference is most pronounced in GB-Ce2. There, two kinks in the shear stress drop curve are visible where there is only one for the other cases. Visual inspections of samples reveal that the new kink is the first one and it is produced by an interaction between the dislocation and the corundum precipitate. This interaction event happens at a lower stress (i.e. after more steps) which means that the mobility of the dislocation is reduced. After the shear stress drops further a second kink is visible, which is the same as the one in the pure case. This kink emerges from the interaction with the GB.

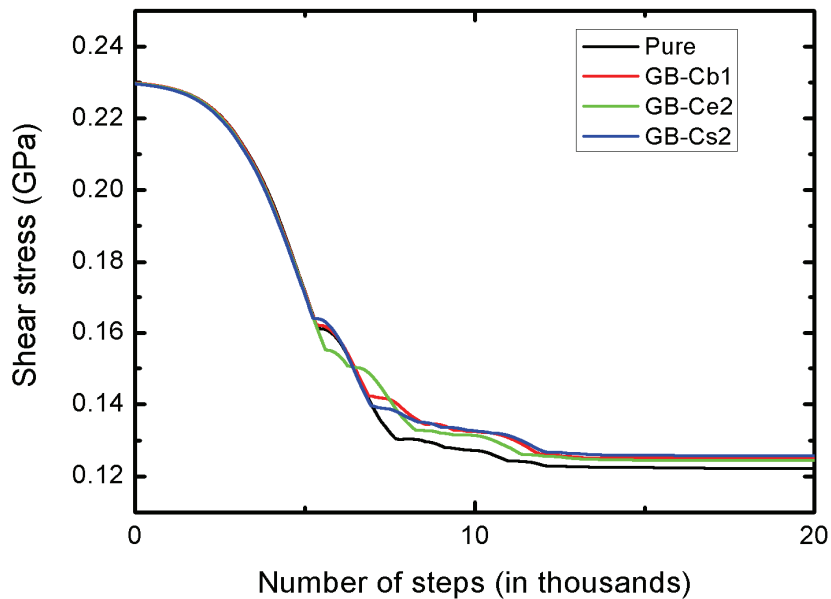


Figure 4.22 The drop in shear stress is followed for the pure and the three impure cases GB-Cb1, GB-Ce2 and GB-Cs2. The curves are shifted along the step axis to have the onset of the propagation at the origin. More or less the onset of the drops is shown until a plateau is reached again. This corresponds with the number of steps required of the propagation of the dislocation.

The short pinning at the corundum precipitate is also visible in the series of configuration outputted during the run. In the impure case the dislocation is pinned at the corundum precipitate and bows with a large curvature whereas in the pure case, it continues the propagation as it is visible in the Figure 4.23 for the case GB-Ce2.

In all the samples with corundum spheres the absorption of the dislocation is slowed down. This can be seen from visual inspections of carefully selected configurations outputted during the run and from the shear-stress evolution during the run shown in Figure 4.22. The most pronounced difference is observed for GB-Cs2 (Figure 4.24).

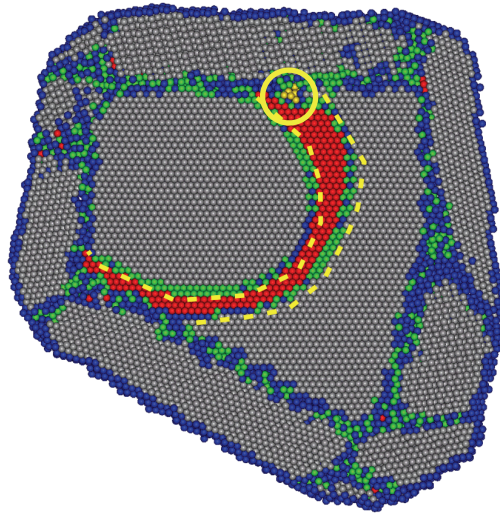


Figure 4.23 Dislocation pinned at a corundum cluster in the GB. The image is taken from GB-Ce2. The dashed yellow line represents the position of the leading and the trailing partials in the pure case after the same amount of relaxation steps.

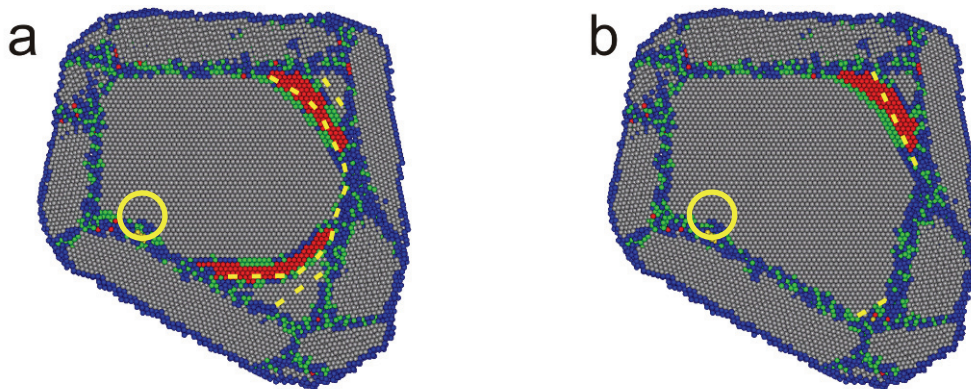


Figure 4.24 Difference in the absorption behavior of the dislocation. The sample “GB-Cs2” is displayed in local crystallinity coloring. The yellow dashed line indicates the position of the dislocation in the pure case at corresponding relaxation steps. (a) shows an intermediate step and (b) the final configurations where in the pure case only the trailing partial dislocation is visible.

4.2.3.7 Oxygen impurities in the grain

Second potential

Different samples with either a dilute distribution of O impurities, with a cluster of dilute impurities or with one corundum precipitate modeled as a sphere of 3.7 angstroms diameter placed in the grain interior are analyzed in this section. All the samples are first relaxed, than once deformed to 0.35% of shear strain and then relaxed again. During the second relaxation the dislocation unpins from the existing pinning points in all the samples. These are ideal conditions to compare the propagation of the dislocation in different samples.

In IG-I1 where one single O atom is placed in the grain, there is a visually noticeable effect: The dislocation bows around the foreign atom as Figure 4.27a shows. After further relaxation the dislocation overcomes the atom. Also in the shear stress drop curve (Figure 4.26) the drag effect due to this single O interstitial is visible. The broadening of the curve should be understood as evidence that the shear stress drops in more MS steps (i.e. "slower") than in the pure case.

The change in shear stress drop curves (Figure 4.26) is a lot bigger in IG-I2 and IG-I3 as the larger numbers of impurities influence the dislocation propagation more. In IG-I2, the dislocation is trapped by impurities soon after unpinning from the existing pinning points (Figure 4.27c). The second kink in the shear stress drop curve (Figure 4.26: green curve) represents an interaction event with the neighboring GB which is also present in the pure case.

In IG-I3 the impurities are placed at a future position of the leading partial dislocation during propagation in the pure case. Consequently, the propagating dislocation should hit all the obstacles more or less simultaneously. The simulation shows that the dislocation propagates towards the obstacles and passes them rather easily. The main exception is the second group of non fcc atoms on which the yellow arrow in Figure 4.25c points. In fact, this is not a single O impurity but two interstitials rather closely placed. The effect on the dislocation is that it changes its slip plane at this obstacle. So, this slightly bigger defect provokes a cross-slip of the dislocation (Figure 4.27d). Cross-slip is also observed at the screw part of the dislocation (Figure 4.27d: yellow circle). The reason for this cross-slip is not known. Because of the cross-slip the mobility of the dislocation changes what can also be seen in the shear stress drop curve (Figure 4.26) for this case.

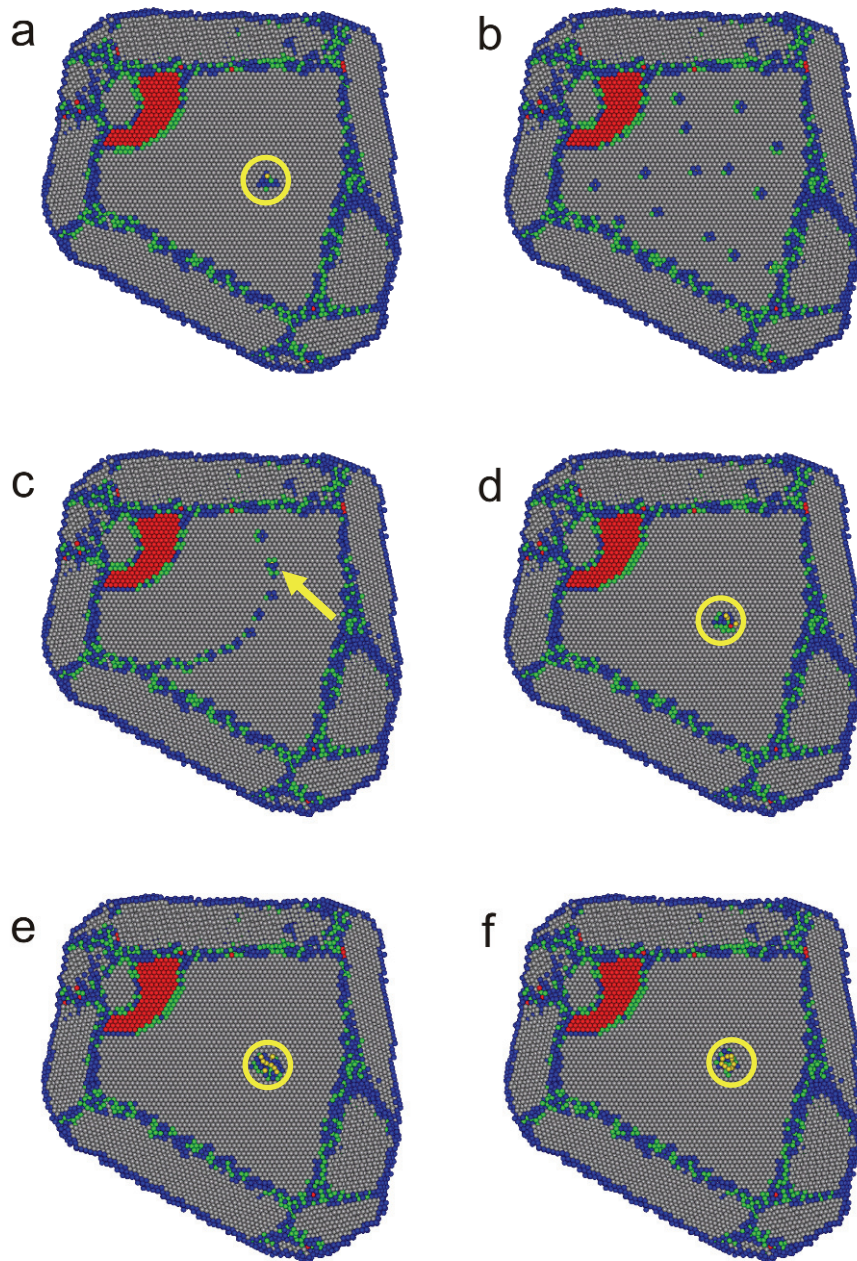


Figure 4.25 Initial configurations to study the influence of O in the grain interior on dislocation propagation. (a) shows a single O interstitial (IG-I1), (b) 14 homogeneously distributed O atoms (IG-I2), (c) 14 O along the future position of the dislocation line after it starts to propagate (IG-I3), (d) 5 O interstitials as a cluster (IG-C1), (e) 14 O interstitials as a cluster (IG-C2), (f) a precipitate of corundum containing 14 O atoms (diameter 3.7 angstroms) (IG-C3). The yellow arrow in (c) indicates a group of two O atoms.

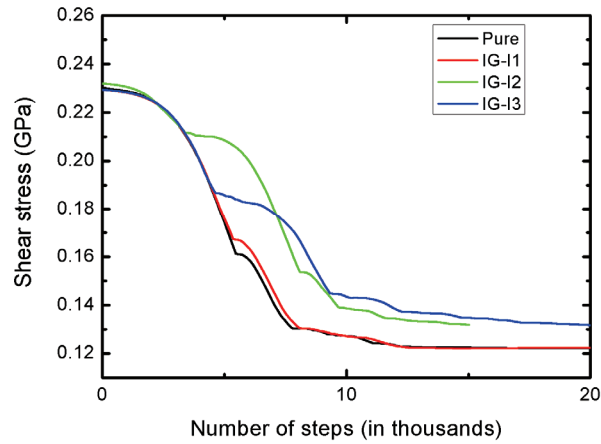


Figure 4.26 The drop in shear stress is followed for the pure and the three impure cases IG-I1, IG-I2 and IG-I3. The curves are shifted along the step axis to have the onset of the propagation at the origin. More or less the onset of the drops is shown until a plateau is reached again. This corresponds with the number of steps required of the propagation of the dislocation.

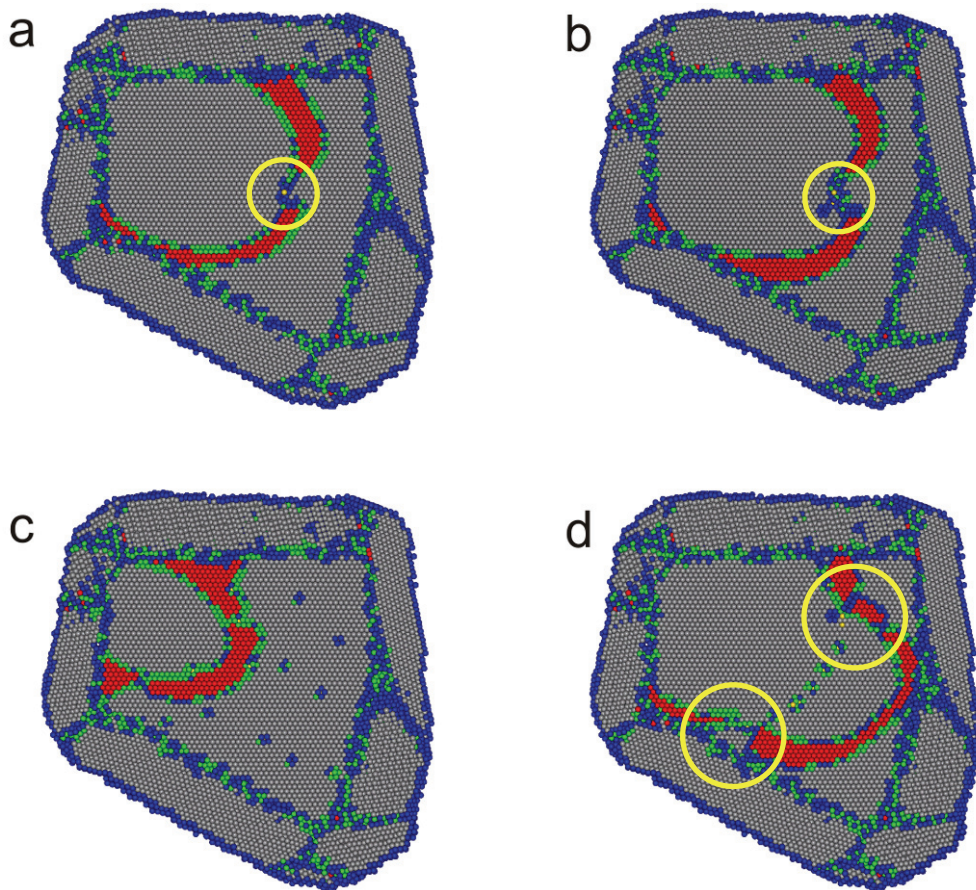


Figure 4.27 Bending of the dislocation at different obstacles. (a) one O impurity (i.e. case (a) in Figure 4.25), (b) 14 O impurities as a precipitate (i.e. case (e) in Figure 4.25), (c) a homogeneous distribution of 14 O atoms (i.e. case (b) in Figure 4.25) and (d) 14 O atoms along the dislocation (i.e. case (c) in Figure 4.25). In case (d) cross-slip is visible (yellow circles).

As in the case of two O impurities very close to each-other cross-slip has been observed in IG-I3, the number of O arranged as clusters is increased further. Obstacles containing 5 interstitial O atoms (IG-C1 shown in Figure 4.25d), 14 interstitial O atoms (IG-C2 shown in Figure 4.25e) and finally 14 O atoms in a corundum precipitate (IG-C3 shown in Figure 4.25f) are simulated. The visual change in the propagation behavior is large: The propagating dislocation bows around all the clusters and the precipitate (see e.g. Figure 4.27b). Cross-slip happens in all the cases. The change of slip plane always starts near the obstacle. The final structures (Figure 4.28) are completely different of the one obtained in the pure case which results in difference for the shear stress of the relaxed structures which Figure 4.29 shows. In Figure 4.29, it is obvious that the shear stress drop behavior is significantly changed: In all the cases with clusters or precipitates the curve is broadened a lot which indicates a significant drag effect due to the obstacles in grain. Remarkable is the fact, that the dislocation does not change the slip plane in case of one atom (IG-I1), it changes by two atomic layers in case of the cluster with 5 atoms (IG-C1) and the corundum precipitate (IG-C3) and it changes by four atomic layers for the largest cluster consisting of 14 dilute O atoms (IG-C2).

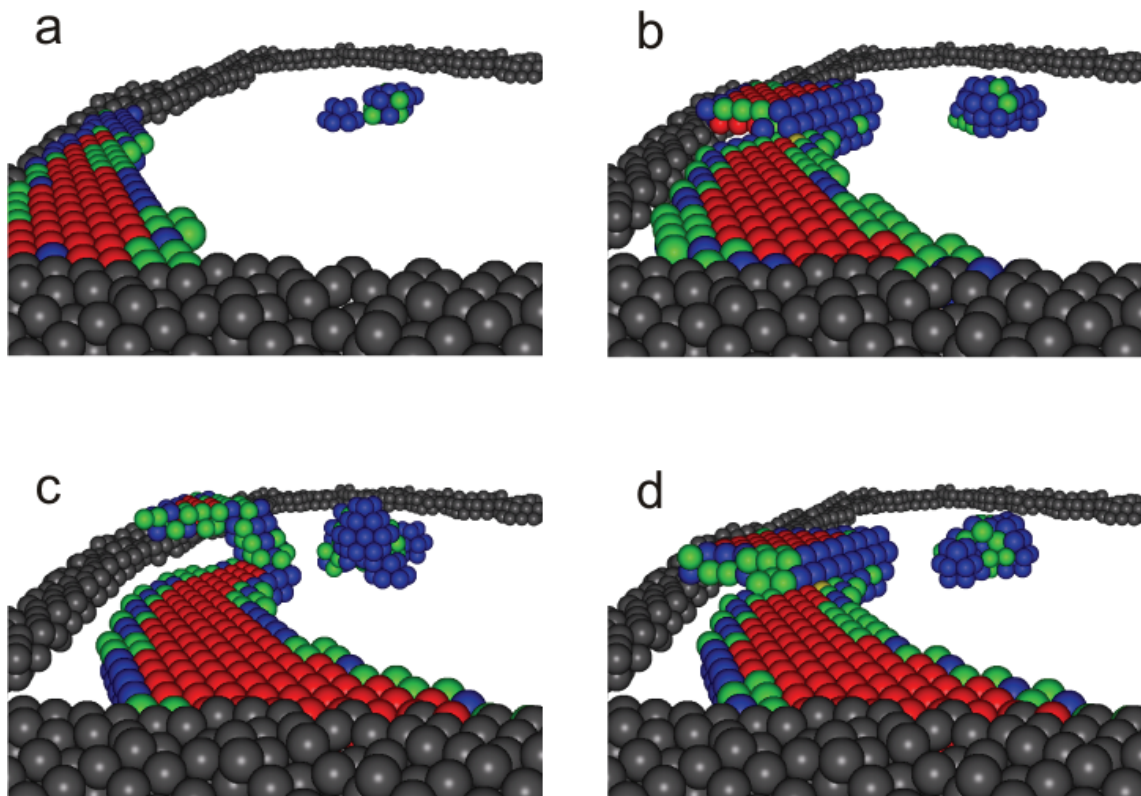


Figure 4.28 Final structures of the samples described in Figure 4.25: (a) IG-I1, (b) IG-C1, (c) IG-C2 and (d) IG-C3. The neighboring GB is illustrated as grey atoms. For the dislocation and precipitates the local crystallinity coloring is used. Fcc atoms are not displayed to emphasis the cross-slipped structure of the dislocation.

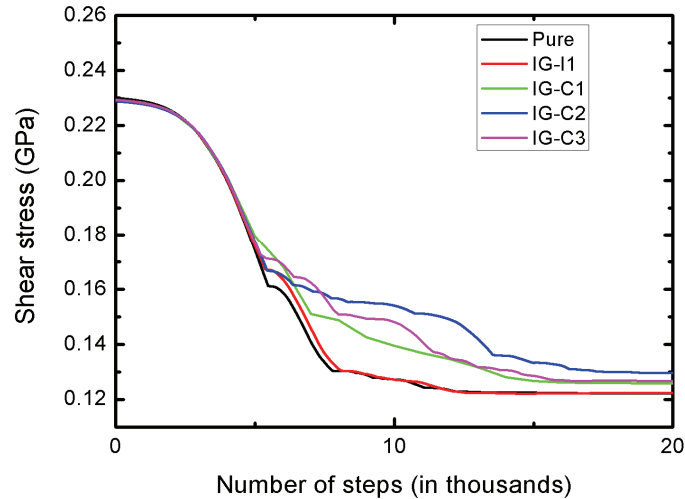


Figure 4.29 The drop in shear stress is followed for the pure and the four impure cases IG-I1, IG-C1, IG-C2 and IG-C3. The curves are shifted along the step axis to have the onset of the propagation at the origin. More or less the onset of the drops is shown until a plateau is reached again. This corresponds with the number of steps required of the propagation of the dislocation.

4.2.4 Discussion

Using the first potential for the simulation of impurities in the scenario of dislocation propagation shows a small effect if the impurities are present as substitutions in the GB. However a remarkable increase in strength of the existing pinning point due to the insertion of 28 interstitials is obtained in case GB-Ie1. The same case simulated with the second potential shows reduced pinning. A possible reason can be the step structure of the dislocation at the impurities which emerges during the relaxation probably due to the very high stress caused by the impurities.

In all the simulations using the second potential the pinning is significantly reduced if the impurities are close or too close to the existing pinning points (see e.g. GB-Ie1, GB-Is1, GB-Ce1 and GB-Cs1). The reason for this decrease has not yet been entirely understood. Changes in the bonding nature due to impurities which lead to instabilities of the structure could be a possible reason. An increase in the pinning strength, i.e. a higher critical shear strain, is mainly observed if impurities are present at the screw side of the dislocation with sufficiently large distance from the existing pinning point or even at the absorption side of the sample (GB-Ia1 and GB-Ia2). The pinning strength of the pure sample could not be reproduced in any of the cases, where O impurities are present on the edge side only (GB-Ie1, GB-Ie2, GB-Ie3, GB-Ce1 and GB-Ce2) using the second potential. Although explanations for the increase or decrease of the critical shear stress due to the O impurities in GBs are missing, it is clear that the changes

with respect to the pure case are small for the second potentials. A possible explanation can be that the inherent stress fluctuations in GBs are rather large. For the sample GB-Is1 a detailed analysis of the stress distribution around the defect and in the rest of the slip plane is executed. It is observed that stresses are not significantly changed due to the O impurities. The 4 O atoms in the GB increase the pressure locally to a peak value of 3.78 GPa on one of the atoms. However, there are several atoms in the GB with pressures over 2 GPa and more atoms which are under high tension, i.e. below than -3 GPa (see Figure 4.30).

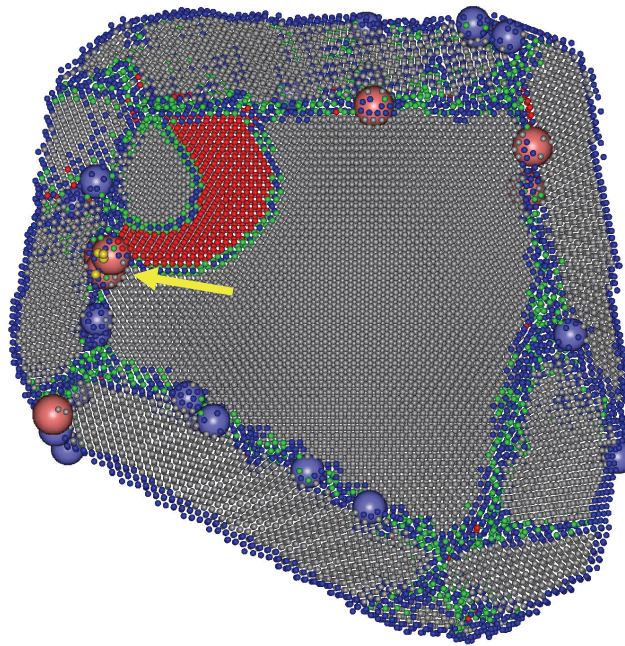


Figure 4.30 Atoms under high or low pressure: Light red spheres indicate atoms with pressure above 2 GPa and light blue indicates atoms with pressure below 3 GPa. The impurities are indicated by the yellow arrow.

As the propagating dislocation is athermally pushed through the sample, the sensitivity to the neighboring GB structure is limited. Therefore bigger effects of the impurities can be expected in finite temperature simulations. Still in a few cases a difference between pure and impure cases is present in the shear stress drop curves, e.g for GB-Ce2 (Figure 4.22), GB-S1 (Figure 4.10).

A bigger effect is observed for impurities in the grain interior. Here the stress concentration in the otherwise homogenous crystal causes a strong interaction with the propagating dislocation. The interaction between the impurity clusters and the dislocations happens without shearing of the cluster or the deposition of a dislocation loop. So, the dislocation overcomes the obstacles with a more complicated mechanism which probably is observed in form of the present cross-

slip. In all cases the evolution of the shear-stress during the propagation is significantly different from the pure case (Figure 4.26 and Figure 4.29).

To summarize: The dislocation propagation under the presence of O has been investigated. The study shows some interaction with O impurities. In all cases where there is a change in the dislocation propagation behavior due to the impurities, the dislocation is dragged. This corresponds with the literature knowledge, from which it is known that an additional stress is required to move a dislocations in a field of solute atoms or to make a dislocation overcome an obstacles consisting of foreign atoms such as dispersions, clusters or precipitates. The drag effect is more pronounced for O clusters in the middle of the grain. Here the dislocation bows around the obstacles and changes in some cases the slip plane to overcome them. However, using the given simulations it is not justified to estimate the quantitative change of mechanical properties due to the impurities. Consequently, the direct comparison with the change in mechanical properties observed by Gianola et al.⁵³ is not yet possible. However the knowledge on the interaction of dislocations with impurities in the grain interior point out that it is worth to test a more homogenous impurity distribution with foreign atoms in both grains and GBs in a fully three-dimensional nc simulations in a similar approach as it is done in section 4.1. This approach corresponds also more to the observations by Gianola et al. who has observed O atoms in GBs and grains of nc thin films using various experimental techniques^{60, 187}.

4.3 Application III - Coupled grain boundary migration

4.3.1 Motivation

As it is shown in the introduction, coupled grain-boundary migration is a relevant system to study the mobility of GBs in nc metals. Here the effect of dilute impurities on the mobility of GBs is investigated. The key idea is to investigate the effect of different O atom distributions on two Al bicrystals with symmetric tilt GBs. It is expected that the impurities have some impact on the migrating boundary such as pinning or at least a drag effect.

Beyond the link to real GB motion or stress-driven grain growth, coupled GB migration is an ideal application to test the local chemical potential approach described in section 3.1 and the potentials described in sections 3.2 and 3.3

4.3.2 Sample description and simulation details

Prof. Yuri Mishin and his coworker Dr. Vladimir Ivanov, both from George Mason University in Fairfax VA, USA started recently the investigation of coupled GB migration in Al samples. Collaboration with them has given access to pure Al samples, but also to details about simulation parameters and the knowledge on the pure samples in the form of preliminary results. Mishin and Ivanov prepared the samples by merging two symmetrically rotated crystals to a flat (CSL) GB³¹. Three different Al bicrystals have been delivered by them and two samples are used for the investigation of the effect of impurities. All the bicrystals contain symmetric tilt grain-boundaries along the [112] axis. One bicrystal has a $\Sigma 75(-751)[112]$ GB with an angle of misorientation is 23.07° (Figure 4.31). More simulations are using this sample geometry which consists in the pure case of 24000 Al atoms. The reference coordinate system is set as: y-axis along the [-751] normal to the GB, the x-axis is along [45-4] parallel to the GB plane and z-axis is parallel to the tilt axis.

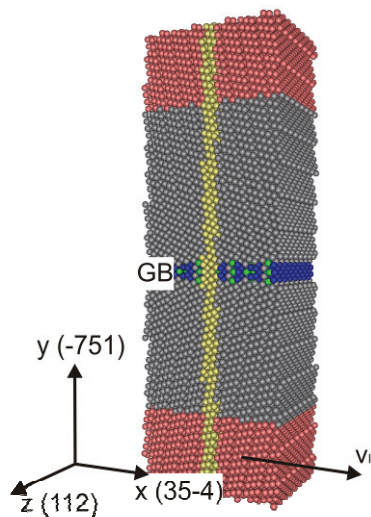


Figure 4.31 Bicrystalline simulation sample with $\Sigma 75(-751)[112]$ GB. The standard color-code for local crystallinity is used. The static atoms are colored in light red and a marker line is displayed as yellow atoms.

The other Al sample which is tested, has a $\Sigma 21(-421)[112]$ GB. The angle of misorientation between the crystals is 44.42° . The coordinate system is chosen analogous to the sample described above. The z-axis corresponds to the tilt axis, y-axis is perpendicular to the GB plane [-421] and x-axis [13-2], respectively. The sample consists of 24192 Al atoms.

Both simulation samples, delivered by Mishin and Ivanov, are small enough to be simulated on the serial version of the MD code. (So, the parallelization of the methodology in section 3.1 is developed simultaneously to the simulation of the coupled GB migration.)

Periodic boundary conditions are applied parallel to the GB whereas perpendicularly to the GB no periodicity is present. At both free surfaces (on the top and at the bottom) there is a layer of static atoms of a thickness larger than twice the EAM cutoff. The number of those static atoms is 4000 for each of the two layers in the $\Sigma 75$ sample and 3392 in each layer of the $\Sigma 21$ sample. This refers to the fixed boundary condition in ³¹.

Simulations are mostly performed at low temperature (MD at temperature of 100 K) or without temperature (MS with global quenching) to uncover the effects of the impurities without or with only minor effects of thermal noise. The MD time-step is 2 fs. This holds for MD as well as the MS. To impose the shear deformation to the sample, the static atoms of one of the layers are moved in x-direction with a constant velocity of 1 m/s. This means atoms are collectively moved in x direction in every time-step by a displacement of 0.00002 angstroms.

To follow the deformation behavior in terms of GB coupling and/or sliding a slice of atoms normal to the shear direction is tagged with an extra label. A visual representation of these atoms can be seen in Figure 4.31: the yellow plane of atoms. This plane is assumed to show the characteristic behavior for coupled GB motion or GB sliding according Figure 1.3c and d.

For the analysis of the samples the vertical position of the GB plus the global stress tensor of the system are outputted in every time-step. Configurations, containing atomic positions, energies, atomic coordination and the local crystallinity data are outputted every 250 time-steps. For these configurations the local atomic shear stress is recomputed if required.

4.3.3 Results on the $\Sigma 75$ sample

4.3.3.1 Pure simulations

The pure sample is simulated first to compare the result of the MD code used here, with the results produced by Mishin and Ivanov. Close inspection of the atomic structure of this GB sample reveals that the GB (and its subsequent motion) may be understood in terms of two fundamental structural units: triangles A and C that exist in the perfect fcc lattice and a kite-shaped unit referred to as B, located at the GB plane which accommodates the misorientation associated with the interface. The legs of the triangles A and C identified in Figure 4.32 represent the $\langle 110 \rangle$ and $\langle 111 \rangle$ orientated conventional cell of the FCC lattices. Detailed spatial

and temporal analysis of a GB migration step reveals that such a structural unit (A) transforms into the kite-shaped structural unit B displayed in Figure 4.32. Upon further GB migration such structural units return to their $[110]/(111)$ orientated conventional cell (C), which due to the misorientation is mirror symmetric to A. Thus the global GB migration step may be seen as the collective downward propagation of the $[110]$ GB dislocations on their (111) slip planes with accommodation via a lateral translation of the upper grain and resulting lowering the global xy shear stress. This atomistic process is the fundamental GB migration event associated with the stick-slip process discussed in refs. ^{29, 30}. The MD code reproduces the atomic processes observed by Mishin and Ivanov.

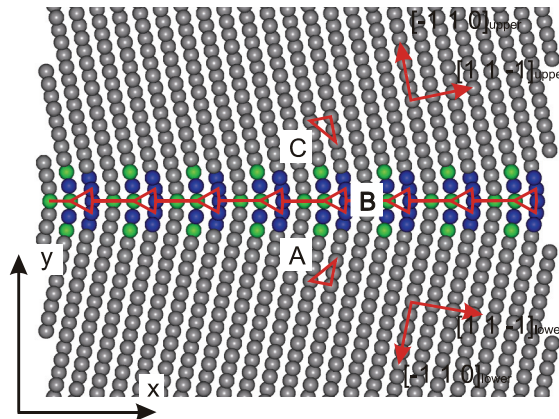


Figure 4.32 Close-up view of the GB, where again the local crystallinity coloring is used. A, B and C mark structural units.

The stick slip process observed by Mishin and co-workers shows an increase in shear stress until a critical stress value is reached at which the GB migration step begins. Subsequently the shear stress is relieved rapidly and even reaches negative values. During this relief of shear stress the actual migration event takes place, where the atoms rearrange. Figure 4.33 displays the resulting shear stress versus simulation time[‡] and the measured GB position versus simulation time of the 0 K MS simulation which shows the same behavior as observed by Mishin. The GB motion results in an immediate drop of the shear stress to an - in this case - negative value. Further static atom displacement results in a repeated linear increase in stress until a critical value at which GB motion again occurs. The deformed sample is shown in Figure 4.34. It is obvious that the marker line shows the same shape as Figure 1.3d which obviously indicates nearly perfect coupled GB migration.

[‡] MS has no concept of time: Simulation time refers here to the number of MS steps multiplied with the MS steps size of 2 fs. Like this results are comparable to MD simulations at finite temperature in terms of process times.

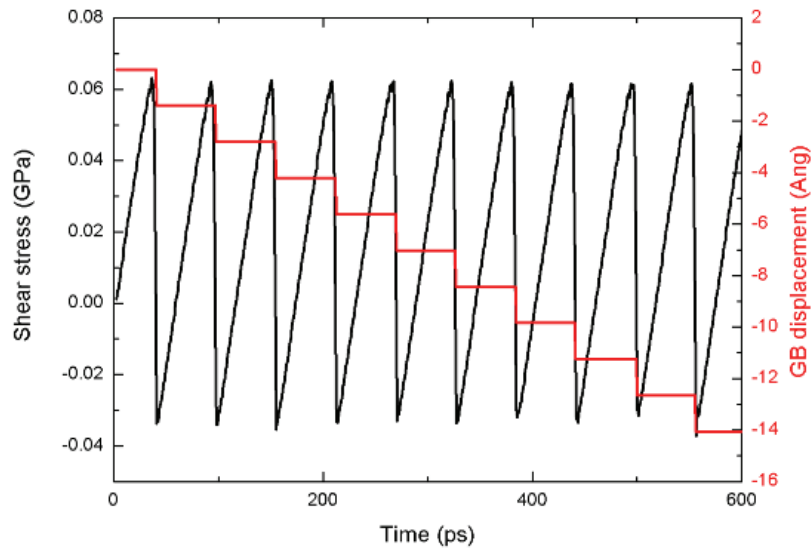


Figure 4.33 Shear stress-time (black) and GB displacement-time (red) curves of the pure sample simulated at 0 K.

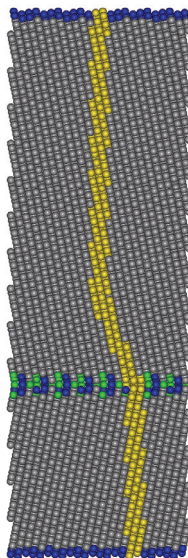


Figure 4.34 The deformed pure sample at 0 K. The yellow marker line remains continuous which is a strong indication for coupled GB migration according to Figure 1.3d.

Figure 4.35 shows the same quantities for the 100 K MD simulations and a similar behavior is evident. The rapid fluctuations of the calculated instantaneous shear stress are due to thermal vibrations. Importantly, the mean maximum shear stress at 100 K is reduced by approximately 25 MPa indicating a thermally activated process is at hand that in principle may be characterized by a migration free energy and a corresponding activation volume. Inspection of the calculated GB position also reveals fluctuations arising from the thermal displacements of the atoms about their mean position. In both the 0 K and 100 K simulations, the resulting downwards velocity of the GB is determined from the average slope of the GB position-time

curve. The theoretical prediction of the ratio between the shear deformation velocity and this GB migration velocity is given by $\beta_{\langle 110 \rangle} = 0.408$ for a misorientation of 23.07° . In both simulations a value approximately 0.406 is obtained which indicates that the observed motion is indeed coupled GB migration as defined by Refs. ^{29, 30}. This is the same behavior as it has been observed by Mishin and Ivanov.

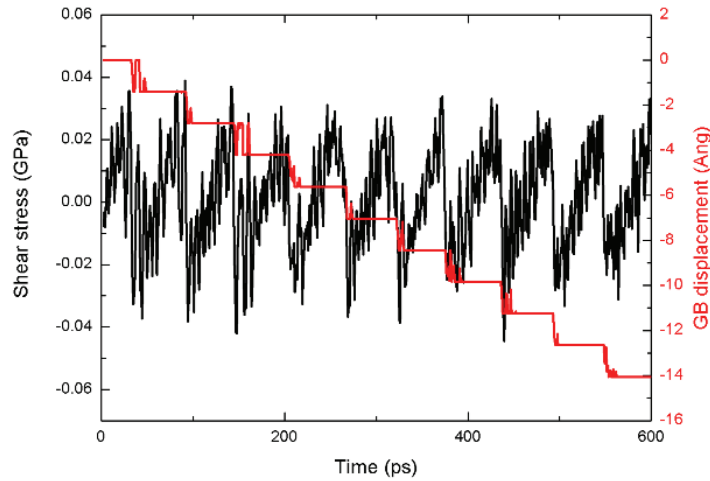


Figure 4.35 Shear stress-time (black) and GB displacement-time (red) curves of the pure sample at 100 K.

Both EAM potentials described in chapter 3 model the Al-Al interactions using Mishin and Farkas Al potential ¹⁷⁸. For this reason, the results in the pure case are the same for the first and the second potential.

4.3.3.2 Homogenous oxygen distribution without temperature

First potential

To monitor the influence of O impurities on the coupled GB migration phenomenon, O atoms are substitutionally inserted into the Al bicrystal described in section 4.3.3.1. Three samples are produced containing one, four and sixteen O atoms. The substitutions are done in the following way: nine atomic planes below the initial coincidence plane of the GB a regular grid of four times four atoms is substituted to obtain the sixteen O sample (Figure 4.36). From these sixteen O atoms the four and one O atom samples are constructed. In Figure 4.36b, the O chosen for the four O sample are indicated by the red arrows, whereas for the one O sample, the lower left O atom is selected. Due to transverse periodicity the regular planar arrangements of O impurities with corresponding surface densities of $4.4 \times 10^{15} / \text{m}^2$, $1.76 \times 10^{16} / \text{m}^2$ and $7.04 \times 10^{16} / \text{m}^2$ is therefore considered.

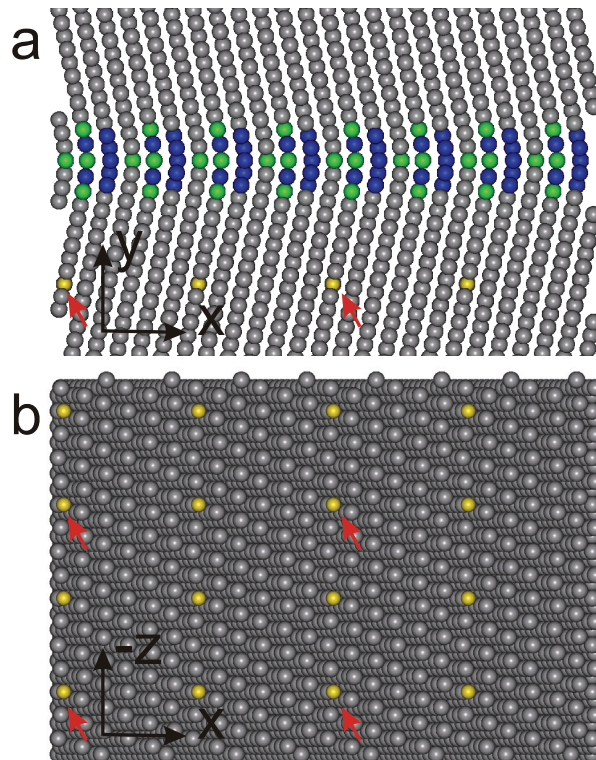


Figure 4.36 (a) Position of the 16 substitutional O atoms (yellow) in the sample relative to the GB. (b) Planar arrangement of the substitutional O atoms. In both parts, the red arrows mark the position of the O atoms in the four O atom configuration. In the one O atom configuration only the O atom in the lower left corner of (b) was used.

Figure 4.37 displays the resulting shear stress-time for a 0 K simulation of the one O configuration. A similar stick-slip behavior is evident, although as the GB approaches the single O atom via coupled GB migration, the critical shear stress needed to activate the migration mechanism first decreases and then increases, reaching a maximum value when the GB migrates away from the plane containing the O atom.

Figure 4.37 demonstrates that the presence of the O atom affects the critical shear stress needed to induce a coupled GB migration event. This influence has a spatial dependence in terms of the distance between the GB plane and the O atoms. For the 0 K simulations, as the GB plane approaches the O atom it initially becomes easier to induce the motion – the critical shear stress decreases. At a distance of approximately 7 angstroms, the critical shear stress then begins to rise. When the GB is close to the O atom the critical shear stress rapidly increases to 90MPa, reaching this maximum. Then the GB plane coincides with the O atom. After that there is a decrease in the next migration event followed by a gradual return to the critical shear stress values that may be associated with the pure Al coupled GB motion seen in Figure 4.33.

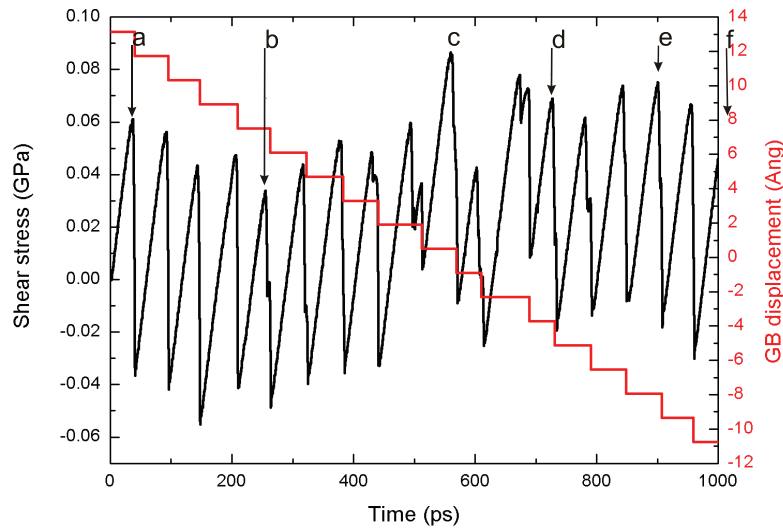


Figure 4.37 Shear stress–time (black) and GB displacement–time (red) curves of the one O sample at 0 K. The origin of the “GB displacement” axis is chosen to be at level of the impurities.

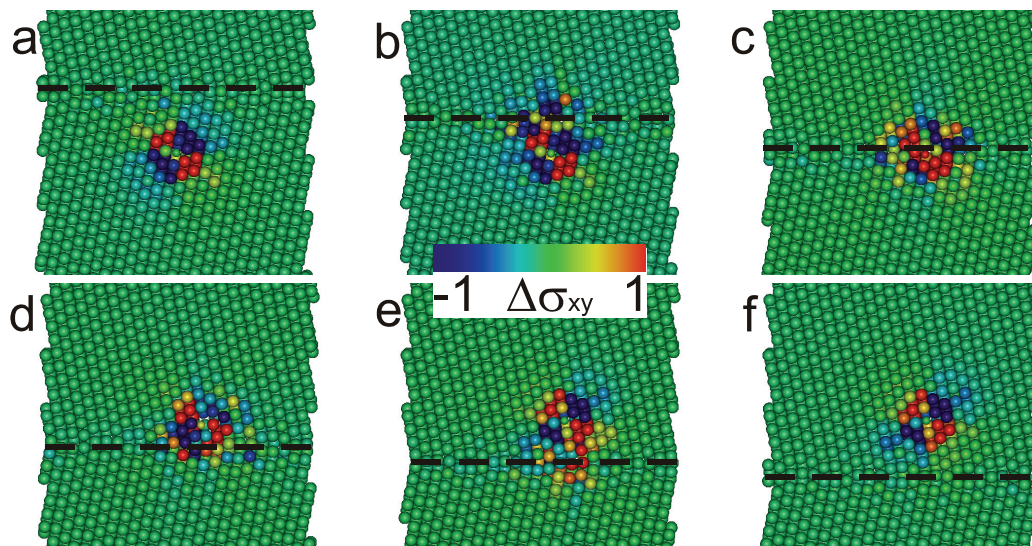


Figure 4.38 Difference in atomic xy shear stress (GPa) between the one O sample and pure sample at the shear stress peaks indicated in Figure 4.37.

To gain an understanding of how the presence of the O atom influences the critical shear stress needed to induce a coupled GB migration event, the local atomic stress tensor is investigated for the 0 K one O simulations. From Figure 3.6 it can be seen that the presence of the substitutional O defect results in a cloud of surrounding charged Al atoms experiencing a strong stress field, in particular a xy shear stress that has strong directional dependence. Figure 4.38a-f displays such local stresses due to the O as the GB approaches and passes the O at a number of configurations which are always at the critical shear stresses for which migration occurs. In Figure 4.38, the displayed stresses are determined from the local stresses of the sample in which the local xy shear field from the bicrystal sample containing no O atoms has been subtracted. The stress

signature of the critical GB configuration is therefore entirely removed and what is seen is the residual stress field due to the O atom. Figure 4.38 shows how this residual shear stress field changes as the migrating GB approaches and passes the O atom – a complex series of local stress transformations is evident. Importantly, the residual field is clearly localized around the position of the O atoms and is maintained as the GB migrates by. A clearer picture can be obtained by partially summing these residual stresses. Table 4.4 displays the global shear stress and three such partial shear stresses in which atoms having an xy shear stress magnitude greater than a given stress threshold are summed.

Configuration	Partial Residual Shear Stress (GPa)			
	$ \sigma_{xy}^i > 0$ (Global)	$ \sigma_{xy}^i > 0.01$	$ \sigma_{xy}^i > 0.05$	$ \sigma_{xy}^i > 0.1$
A	0.001	0.007	0.005	0.013
B	0.029	0.029	0.060	0.087
C	-0.024	-0.010	-0.058	-0.094
D	-0.008	-0.011	-0.013	-0.019
E	-0.015	-0.016	-0.055	-0.082
F	-0.002	-0.006	-0.009	-0.014

Table 4.4 Localness of the effect of the O impurity on the shear stress distribution

This is done for each configuration displayed in Figure 4.38. Larger thresholds increasingly include only atoms that are close to the O defect. Inspection of the global residual shear stress reveals an initially positive value which then becomes maximally negative as the GB migrates past the O and subsequently becomes less negative. The precise behavior correlates well with the changes in the critical shear stress needed for migration to occur shown in Figure 4.37. Thus the behavior seen in Figure 4.37 may be largely understood in terms of the effective shear stress that acts on the GB, which is the sum of the applied shear stress and the internal stress (residual stress) that arises due to the presence of the O defect. Thus if a defect produces a positive internal shear stress then a reduced applied shear stress is needed to activate the migration event, whereas a negative internal shear stress requires an increased applied shear stress. The important message that can be obtained from the data of Figure 4.37 is that the trends seen in the global residual shear stress become progressively enhanced when considering the increasingly local stress signature of the O – the effect of O on GB migration is localized to the atoms in the immediate surrounding of the O atoms. However, during the MS simulation only global GB migration events are observed.

From Figure 4.37 and Figure 4.38, the variation in the critical shear stress required to induce a GB migration event manifests itself in either an increased or decreased waiting time for GB. Such spatially dependent variations average out since the calculated GB migration velocity resulting in a beta factor of about 0.411, which is not so different to that of the pure Al case.

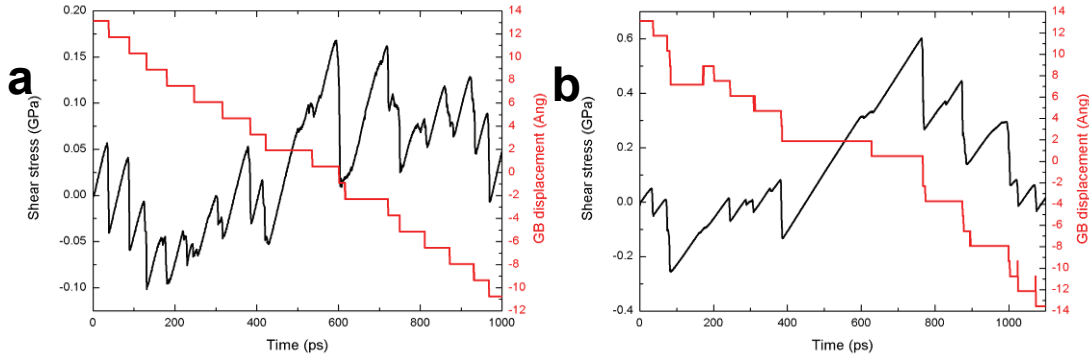


Figure 4.39 Shear stress–time (black) and GB displacement–time (red) curves of the four O sample at 0 K (a) and the sixteen O sample at 0 K (b). The origin of the “GB displacement” axes is chosen to be at level of the impurities.

If the number of O atoms in the sample is increased to four and to sixteen the shear stress-time and GB position-time data presented in Figure 4.39a and b is obtained. An amplification of the initial decrease in the critical shear stress needed to induce a migration event is obviously present as well as the latter increase in shear stress when the GB is directly nearby the O. The generally larger needed critical shear stresses also entail significantly increased waiting times between migration events demonstrated that the local mobility of the GB is significantly altered when in the presence of such a high density of O atoms. In the case of the 16 O planar arrangement the GB is for a while pinned to the O atoms. Moreover after unpinning, the subsequent time between migration events is short compared to that of the pure Al case; in this regime it can happen that the GB migrates twice to three times in relatively short time (less than 50 ps). This rapid movement may be understood by the fact that a relatively large critical shear stress is attained to make the GB migrate past the O layer. The amount of shear strain that can be relieved is geometrically constrained to that associated with the migration of one atomic layer. Therefore after migration past the O atoms there remains still a significant amount of shear stress which is immediately relieved by subsequent GB migration to pure Al regions that are only slightly affected by the O defects. Importantly, the sum of these rapid drops in shear stress due to a quick succession of GB migration events is also geometrically limited since the resulting migration cannot exceed that seen in the case of the pure Al simulation. This is reflected in the coupling factors averaged over the entire simulation which are not too different

from that of the pure case, where the average coupling constants slightly increase to values around 0.420 for the four O samples and values above 0.450 for the sixteen O samples.

Second potential

The samples tested here correspond to the one described by Figure 4.36. Plotting the resulting shear stress-time curve in case of one substitutional O atom top of the one for the first potential and the pure case, two remarkable differences are observable (see Figure 4.40): The new curve deviates later of the pure case and returns sooner to the pure curve and secondly the decrease in shear stress while GB is approaching the O impurity and the following increase for the GB at the O impurity are more pronounced. To summarize, similar effects are observed for the case of one O impurity however they are more localized and more pronounced in the quantity. This corresponds with a comparison of the local stress signatures, which show the same trends. This is also observed in Figure 3.9 in section 3.3.4 which compares the pressure fields around O defects in bulk fcc Al. There the change in pressure is more localized and higher in absolute values.

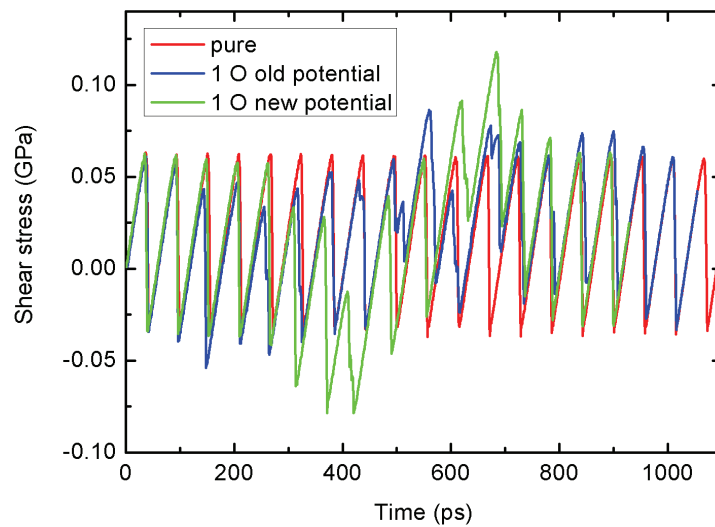


Figure 4.40 Shear stress-time curves of the pure sample (red), the one O case using potential of section 3.2 (blue) and the one O case using potential described in section 3.3 (green). Simulations where carried out without temperature (0 K).

If the O concentration is increased to four and sixteen substitutions the observations made for the one O case are more pronounced (see Figure 4.41). However, overall coupling constants are maintained due to geometrical limitations which have to be fulfilled.

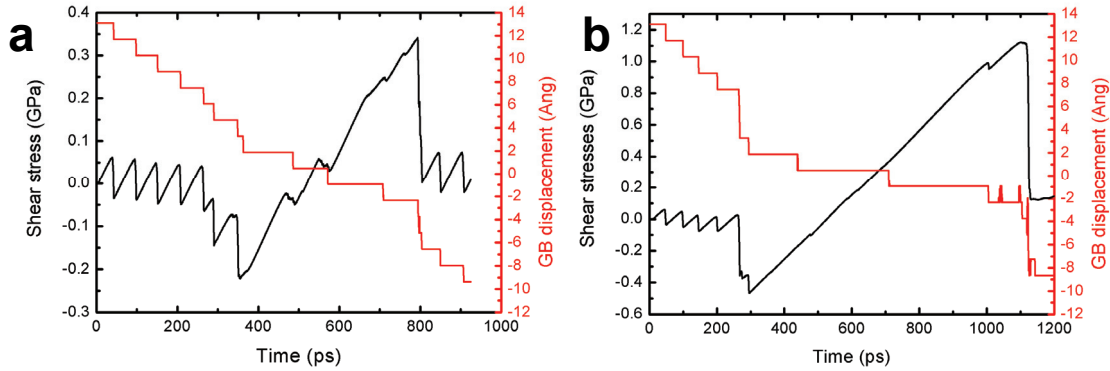


Figure 4.41 Shear stress–time (black) and GB displacement–time (red) curves of the four O sample at 0 K (a) and the sixteen O sample at 0 K (b). The origin of the “GB displacement” axes is chosen to be at level of the impurities.

Comparing the first and the second potential by the maximal shear stresses obtained for given numbers of O substitutions makes clear that there is a stronger effect in the case of the second potential (see Figure 4.42).

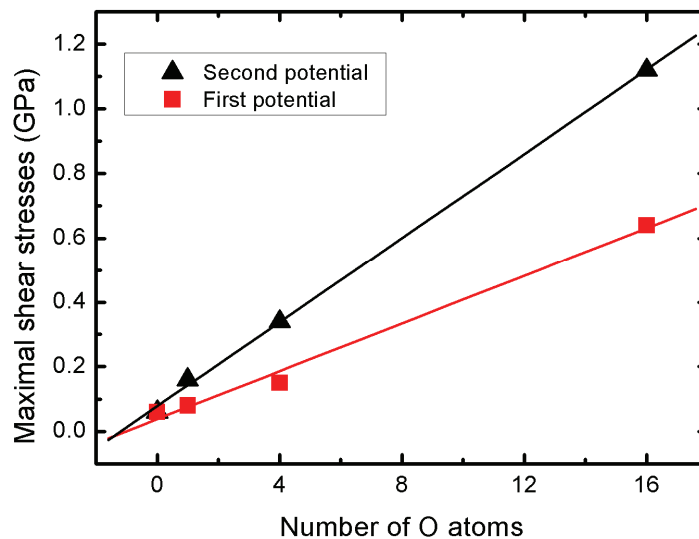


Figure 4.42 Maximal shear stress vs. number of O atoms. In case of the 1st potential the linear correlation indicated by the red line was found. In case of the 2nd potential there is also a linear correlation (black line) however the slope is steeper.

4.3.3.3 Homogenous oxygen distribution with temperature

First potential

If the same samples in section 4.3.3.2 are tested using MD simulations at 100 K temperature the results obtained from MS are reproduced with additional noise because of the thermal motion of

the atoms (Figure 4.43a-c). In the case of the one O simulation it is observed that the distance at which the critical shear stress begins to rise is now approximately 4.2 angstroms (Figure 4.43a) instead of 7 angstroms in the case without temperature (Figure 4.37).

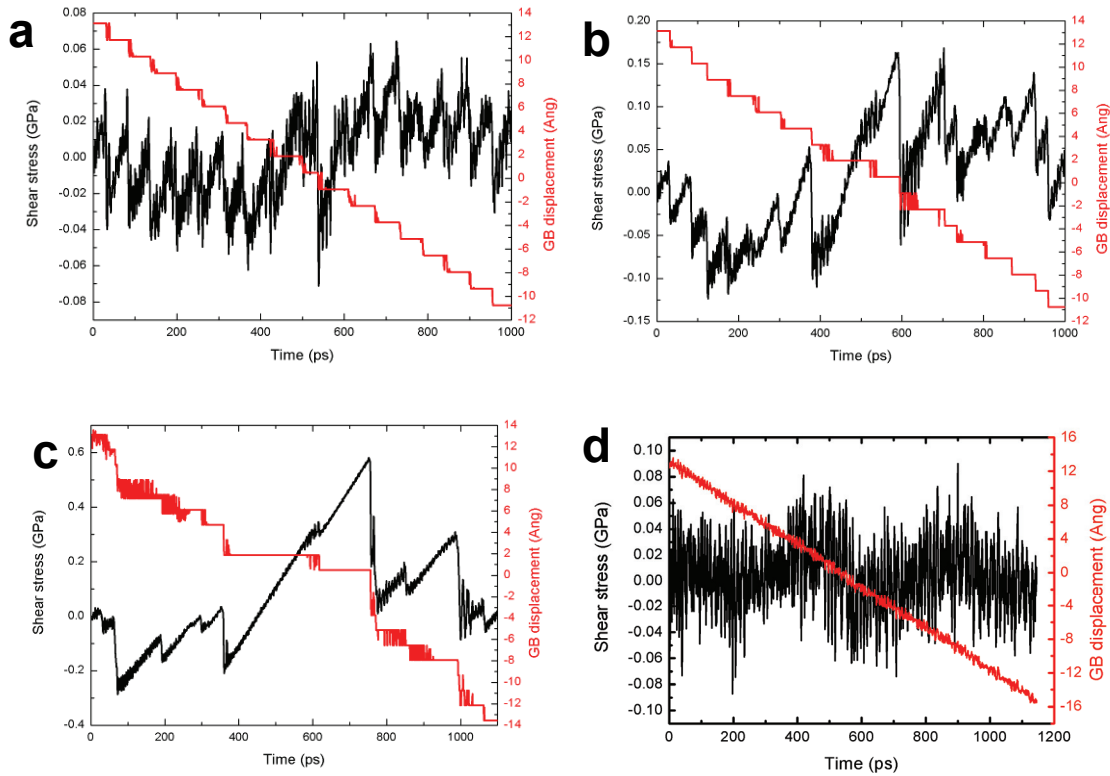


Figure 4.43 Shear stress-time (red) and GB displacement-time (red) curves for the one O case (a), the four O case (b) and the sixteen O case (c) with homogenous distribution of the substitutions at a simulation temperature of 100 K. (d) The same for a one O sample at 500 K. The origin of the “GB displacement” axes is chosen to be at level of the impurities.

To illustrate the effect of the higher temperature, the sample containing one substitutional O defect is equilibrated at 500 K. Then the sample is analogously deformed as before. Figure 4.43d shows shear stress-time and the GB displacement-time curves. As the GB displacement-time curve shows the motion of the GB happens at this higher temperature in a more continuous way than the aforementioned stick slip processes. This can also be seen in the visual inspection of atomic configurations. Hardly any discrete migration events are observed then.

The difficulty of separating the effect of the O impurities from thermal noise is obvious at this higher temperature: No more effect due to the O is e.g. visible in the GB displacement-time curve. Beside this, the simulation follows the overall trends for coupled GB migration explained by the publications of Cahn and Mishin²⁹. The overall coupling constant derived from the slope

of the GB displacement-time curve is not changed compared to cases without temperature which corresponds to Cahn and Mishin's observations.

4.3.3.4 Inhomogeneous oxygen distribution without temperature

First potential

Instead of homogeneous distributions of impurities over the whole GB plane, an inhomogeneous distribution of impurities is considered. The O atoms are placed in a plane rather close to the GB. However, they are distributed only over a quarter of the sample cross-section in an array of two by eight atoms (Figure 4.44a).

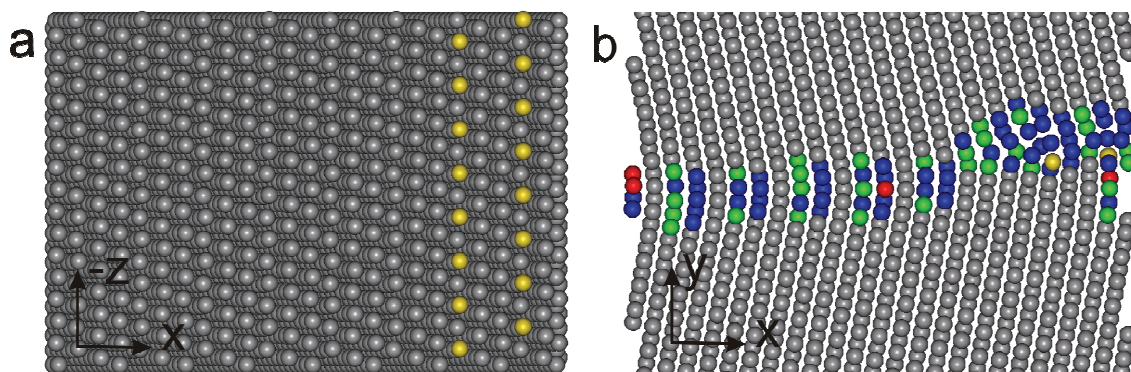


Figure 4.44 (a) O atoms positioned in a inhomogeneous distribution over only one quarter of the sample cross-section. (b) shows an atomic section, where the difference in migration behavior due to the presence of the O (right hand side) is obvious.

The resulting shear stress-time and GB displacement-time curves are shown in Figure 4.45. The fact that the impurities are placed closer to the GB in the initial configuration changes the curves in the sense, that starting point is later compared to the previous cases. The data on the GB position is split into two curves: one representing the average position for the GB over the O impurities and one for the pure part above Al atoms only. Figure 4.45 shows that the maximal critical shear stress in the inhomogeneous case (0.63 GPa) is about the same as in the case of 16 O atoms homogeneously distributed (0.64 GPa). However there is a clear difference in the motion of the GB. It can move nearly freely at the side without O whereas it is clearly pinned by the O impurities on the other side until the critical shear stress is reached. At that point of maximal shear stress, the GB part on the pure side has already moved by several migration events which can be seen in Figure 4.44b. According to Figure 4.45, the GB part over the impurities seems to move forth and back before overcoming the O atoms. However, in the visual inspection of configurations it is seen that the GB is stationary at these impurities. So, the different shape of the GB position-time curve can be explained by the fact, that it is difficult to determine the GB position on a reliable basis due to the large change in the local structure when

one part is migrating and the other is stationary. As Figure 4.45 shows, the part at the impure side also overcomes the obstacles. After successfully passing the obstacles, the critical stress decreases rapidly and the part above the impurities catches up with the part above the pure side. With sufficient distance from the impurities the planar GB is formed again which also can be seen in the visual inspection of the atomic configurations.

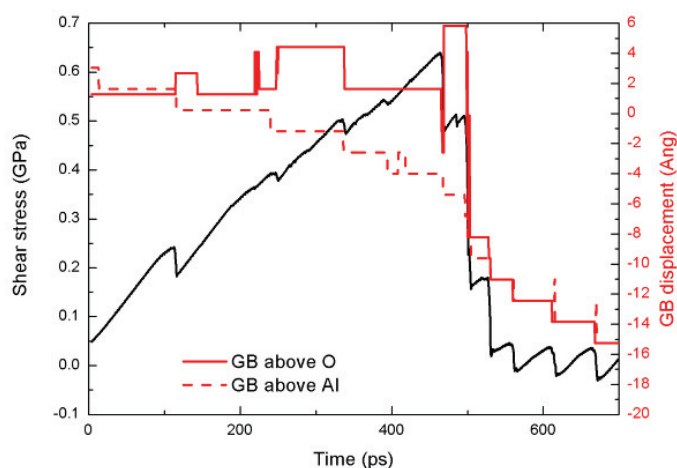


Figure 4.45 Shear stress–time (black) and GB displacement–time (red) curves of the 16 O sample with heterogeneous distribution of the O impurities at 0 K simulation temperature. The origin of the “GB displacement” axis is chosen to be at level of the impurities.

Second potential

A similar inhomogeneous O distribution as for the first potential is also investigated using the second potential Figure 4.46 however the impurities are inserted 9 atomic planes below the GB. It is observed that the GB over the impure part migrates faster towards the impurities than the part of the GB which migrates on the side without impurities (Figure 4.46b). After this the part at the impurities remains stationary and the rest of the GB can catch up and overtake. Up to a critical stress of 0.60 GPa the part at the impurities is pinned. At this point the part over the pure sample has migrated already several times (Figure 4.46c). After unpinning the impure part catches up and a planar GB is formed with large enough distance from the impurities (Figure 4.46d). However a distortion of the lattice is visible around the impurities. The O atoms are in a more excited configuration than the initially substitutional positions after the GB passed them. Apparently Al atoms close to the O atoms are missing. In a visual inspection using the atomic coordination of the sample additional Al atoms are seen near the GB (Figure 4.48). The effect happens collectively along the whole rows of O atoms.

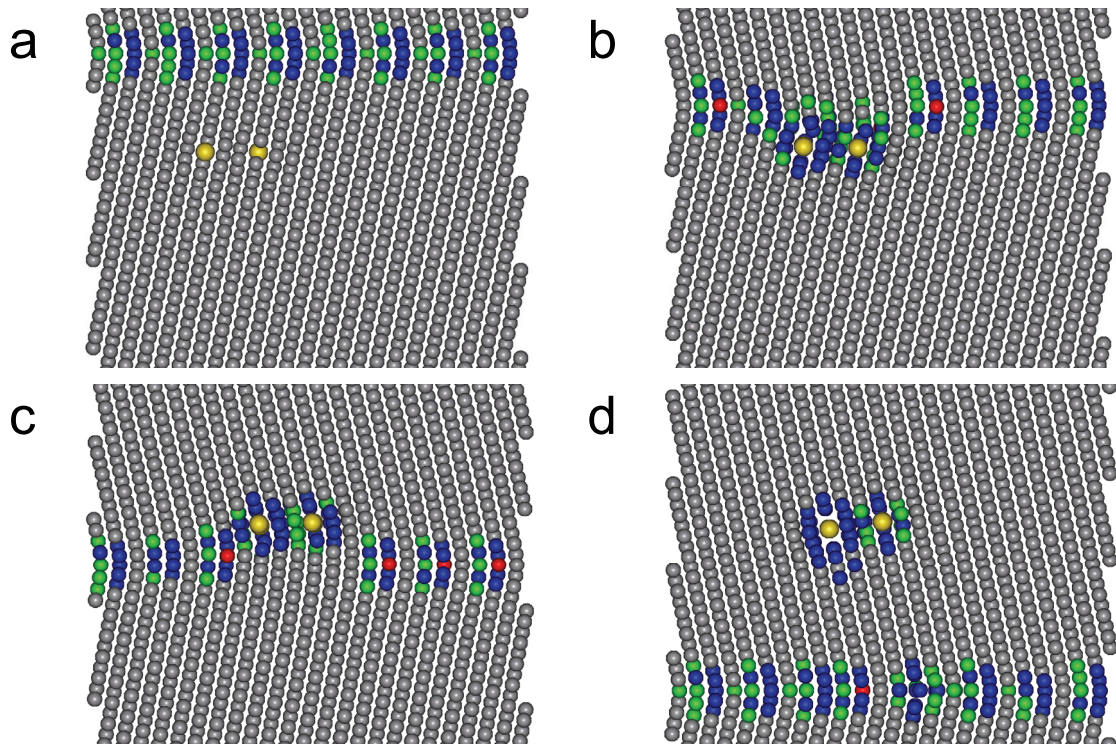


Figure 4.46 Inhomogeneous O distribution: Initial structure (a), at minimal stress after 215 ps (b), at maximal stress (after 955 ps) (c), and after 1475 ps (d).

For the second potential, the maximal shear stress obtained for the inhomogeneous O distribution is significantly lower than for the homogeneous simulation (Figure 4.47) which is different from the first potential where both are approximately the same.

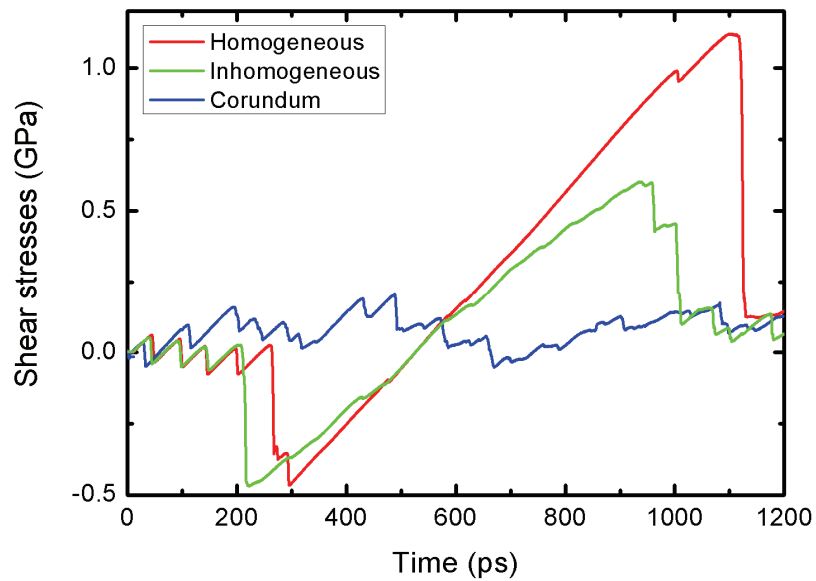


Figure 4.47 Shear-stress time curves for three sixteen O simulations. (red) with an homogeneous O distribution of 4 x 4 atoms, (green) in a inhomogeneous O distribution with all the O atoms on one side in a array of 2 x 8 atom and (blue) with a sphere of corundum in the sample.

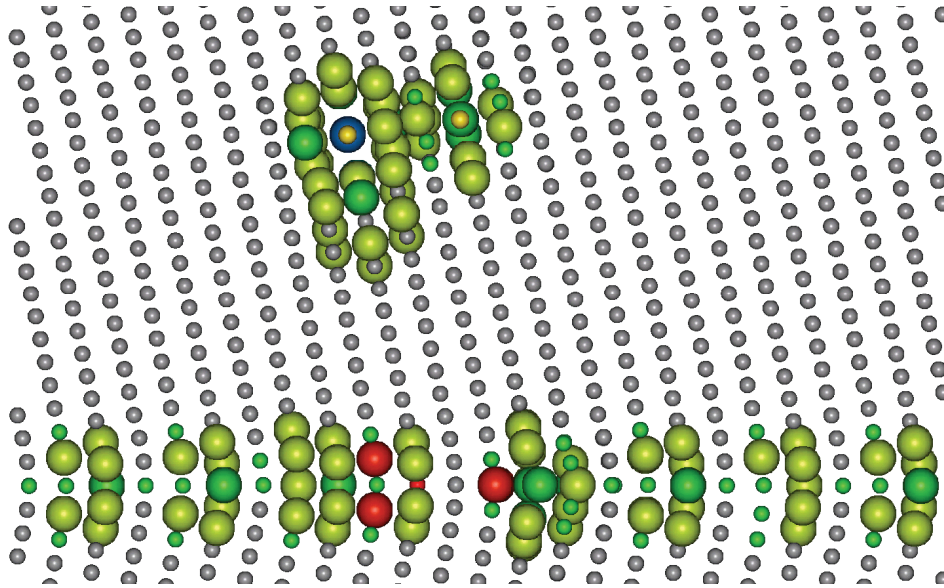


Figure 4.48 Cut through Figure 4.46d. Small atoms correspond to local crystallinity coloring. Large atoms display the atomic coordination (blue = 6 to red = 13). 12 coordinated atoms are not displayed in case of the large atoms.

As an additional geometry, a sample, where a sphere of fcc Al atoms is removed and substituted by a sphere of Al_2O_3 in a corundum arrangement, is simulated. The corundum sphere contains 16 O atoms. In the resulting shear stress-time curve it is seen that much smaller critical shear stresses are obtained (Figure 4.47: the blue curve). After the GB has passed the obstacle, the shear stresses curve does not return to the curve known from the pure case. So, over a rather long time there is an interaction between the corundum sphere and the GB. This interaction can also be seen in the visual inspection of configurations: In the initial state the corundum sphere deforms the lattice in its neighborhood without affecting the GB (Figure 4.49a), as soon as the GB is approaching the distortion of the lattice increases significantly in size (Figure 4.49b). The GB overcomes the obstacle with some bowing but not as much as in the previous inhomogeneous case as the critical strength of the obstacle is smaller (see e.g. shear-stresses-time curve Figure 4.47). Afterwards the lattice remains distorted. The GB moves further and further away but it is affected by the distortions in the lattice over a large distance (Figure 4.49c and d). The effect of the corundum on the critical shear stress is lower, but of longer range. It is important to mention that the structure of the corundum precipitate does not change much when the GB passes the obstacle. No O atom distribute further into the crystals.

The large distortion of the lattice in both cases with inhomogeneous O distributions (2 x 8 atoms and corundum) raises serious questions. A few explanations are given in the discussion (section 4.3.5).

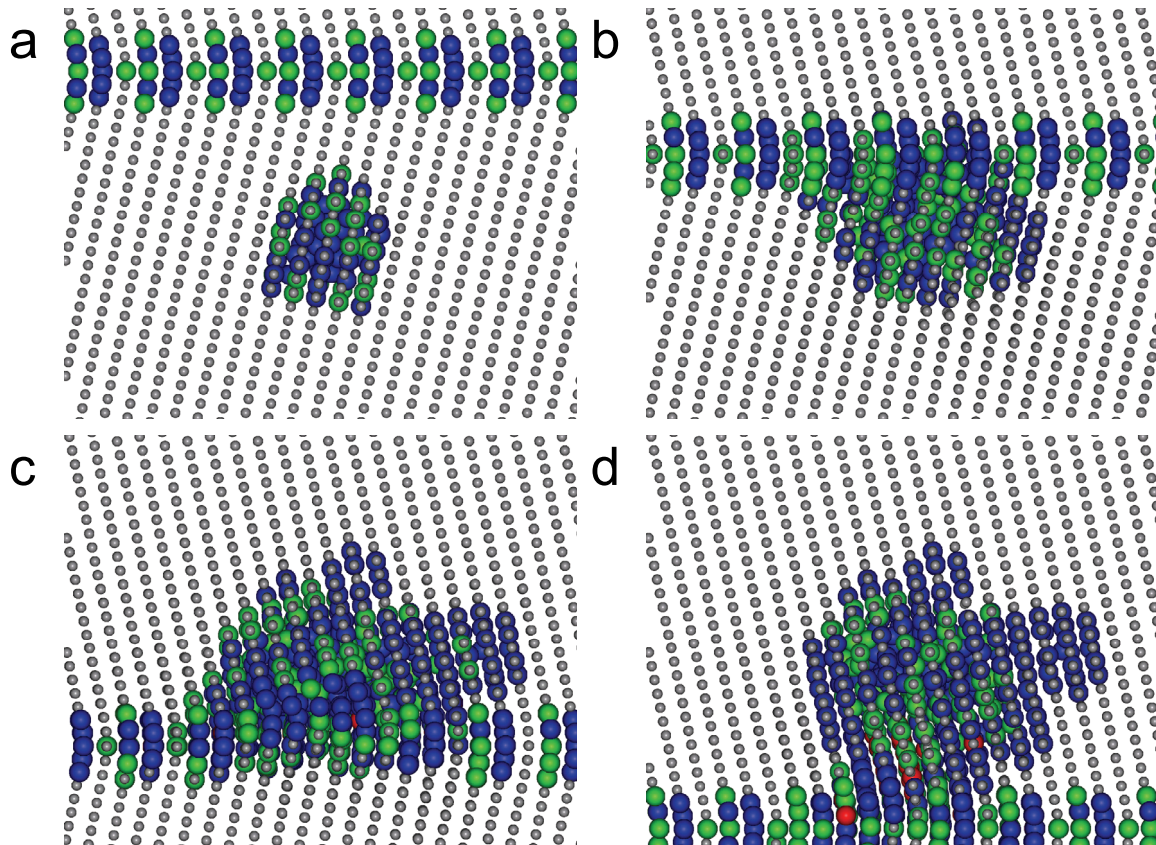


Figure 4.49 Corundum sample. Initial sample (a), Sample after 360 ps, sample after 1060 ps, and after 1400 ps.

4.3.3.5 Interstitial O impurities

First potential

To test an interstitial impurity, one O atom is added in a tetrahedral interstitial site to the Al crystal. Before the sample is deformed, it is relaxed. The tetrahedral interstitial transforms to a 100-dumbbell interstitial structure (Figure 4.51a) as this is the more stable configuration using this potential (compare section 3.2). The shear stress versus simulation time and the measured GB displacement versus simulation time curves of the 0 K MS simulations (Figure 4.50a) look rather similar to the one of the substitutional defect, however the maximal critical shear stress is higher (120 MPa instead of 90 MPa for the substitutional).

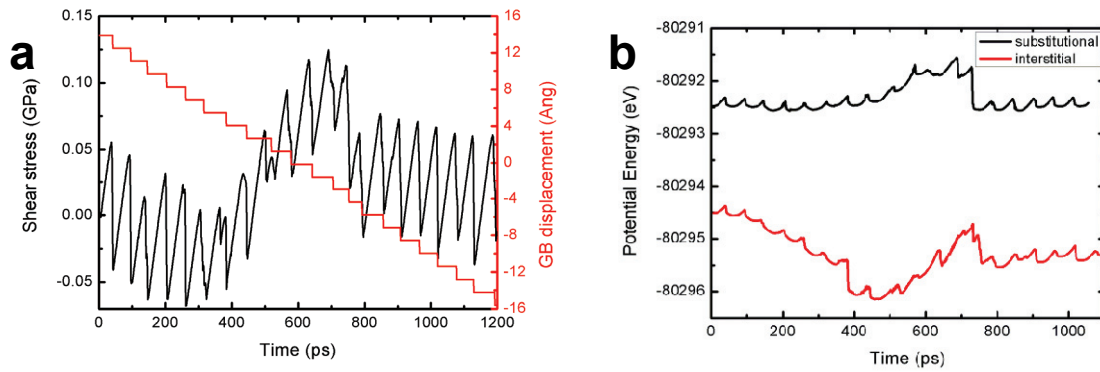


Figure 4.50 (a) Shear stress–time (black) and GB displacement–time (red) curves of the one O sample at 0 K with the O impurity at a interstitial side and (b) the corresponding potential energies–time curves for the substitutional (black) and interstitial case (red). The origin of the “GB displacement” axis is chosen to be at level of the impurities.

In the visual inspection of the simulation data, it is observed that the O atom pushes an Al atom in the GB out of its position as soon as the O is in the GB (Figure 4.51b). After the GB migrates further, the O atom does not move with the GB and moves to a substitutional position in the fcc Al lattice Figure 4.51c. The Al atom which has been pushed away by the O atom pushes another Al atom out of its position in the layer below where the GB is migrating to. Like this, there is always an additional atom in the GB, however these are different Al atoms and not the O impurity. These additional atoms are migrating to the free volume of the GB structure, i.e. to the middle of the kite structure “B” in Figure 4.32. In terms of energy it is interesting to see (Figure 4.50b), that the final structure, which contains the additional Al atom in the GB and the substitutional O impurity, is lower than the initial structure with the 100-dumbbell O interstitial. This is different from the substitutional case where initial and final structures are at the same energetic level.

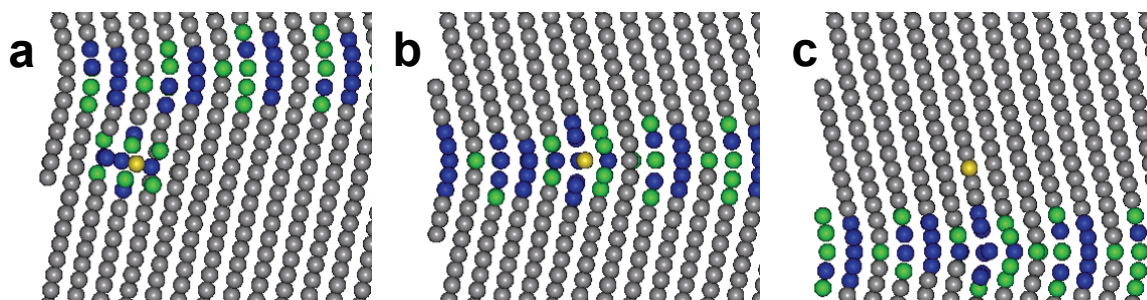


Figure 4.51 Lattice position of a additional O atom (yellow) during coupled grain boundary migration: (a) before the GB has passed the O atom is in a (100)-dumbbell position. (b) the O atom is additional in the grain boundary and (c) the O is in a substitutional position and the GB contains an additional Al atom.

4.3.4 Results on the $\Sigma 21$ sample

4.3.4.1 Pure

First potential

From private communication with Mishin and Ivanov and from Ref. ³¹ it is known that the $\Sigma 21$ sample shows only coupled GB motion at finite temperatures (see Figure 7 in Ref. ³¹). For the study of the influence of O impurities on GB migration, simulations at low temperatures are preferred to minimize thermal noise. Therefore the pure sample is first studied at 0 K and at 100 K. As one can see in Figure 4.52a, the shear stress-time curve at 0 K shows a different behavior than the saw-tooth curve for the $\Sigma 75$ sample (Figure 4.33). Also the motion of the GB is unlike the case of the other sample.

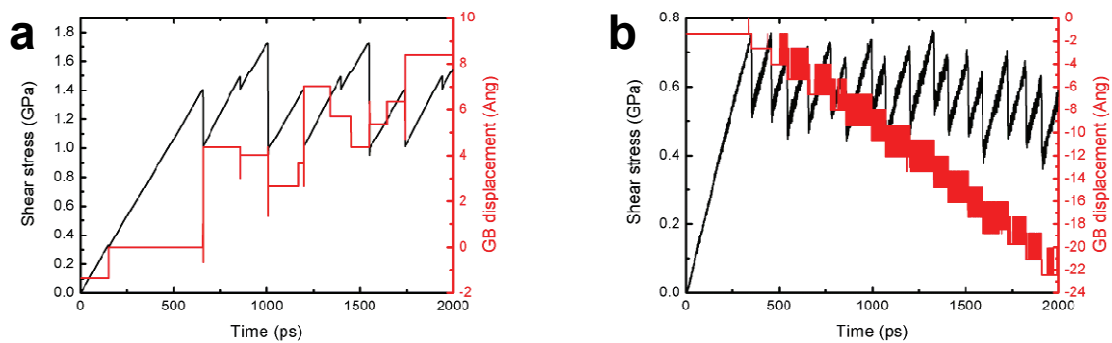


Figure 4.52 Shear stress–time (black) and GB displacement–time (red) curves of pure sample with a $\Sigma 21$ GB simulated at 0 K (a) and 100 K (b).

In case of a simulation temperature of 100 K things become more similar: There is a saw-tooth curve and the GB moves downwards using more or less discrete migration events (Figure 4.52b). This corresponds with findings of Mishin and Ivanov ³¹, who observe coupling in the temperature range from 100 K to 900 K for this system. Also the coupling constant β of 0.8 is well reproduced as it is evident from Figure 4.52b. The mechanism for the coupled GB motion under finite temperature is similar to the $\Sigma 75$ sample. Details on the mechanism can be found in e.g. Figure 5 of Ref ³¹.

For the 0 K simulation the GB moves less than half as much in the normal direction and even in the opposite direction compared to the samples simulated at 100 K temperature. Visual inspection of configurations outputted during the run at 0 K shows that the GB is more sliding than showing a coupled motion which can also be seen from a single frame taken at a later point in the simulation (at about 10 % shear strain). Here the yellow marker plane is more or less perpendicular (the bending is due to the applied load) to the GB and it is hardly connected. This

corresponds more with Figure 1.3c which is the prototypic picture for GB sliding. However some trends corresponding to coupling are visible in Figure 4.52a and Figure 4.53a. At 100 K, the shape of the marker line in the deformed state of the sample corresponds with Figure 1.3d which is an indication for coupled GB motion (Figure 4.53b).

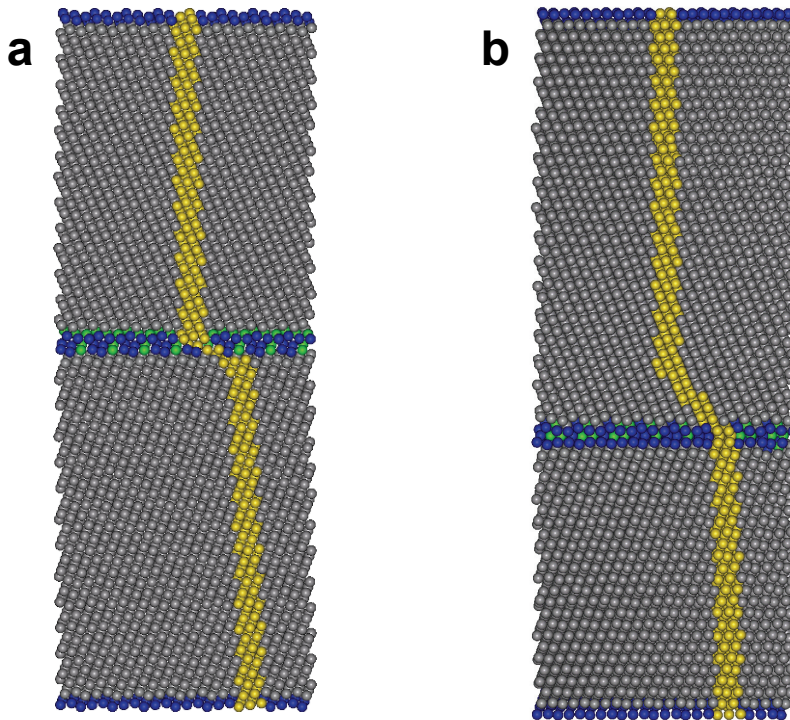


Figure 4.53 Deformed $\Sigma 21$ GB simulation sample. (a) At 0 K: The marker line remains more or less perpendicular and seems to be discontinuous which is an indication for a strong GB sliding contribution as shown in Figure 1.3c. (b) At 100 K: The continuous marker line shows the shape of coupled GB migration in Figure 1.3d.

4.3.4.2 Homogenous oxygen distribution with temperature

First potential

MD simulations at 100 K temperature are carried out to investigate the influence of O impurities on coupled GB migration, An increasing amount of O impurities (one, four and sixteen substitutions) are added to the samples in a homogenous way analogous to section 4.3.3 on the $\Sigma 75$ GB.

Deformation of these samples gives the shear stress-time and GB displacement-time curves shown in Figure 4.54 and Figure 4.55. The critical shear stresses are slightly reduced in case of one O impurity (Figure 4.54) compared to the pure case. However no significant increase in the maximal shear stress comparable to the $\Sigma 75$ samples is visible.

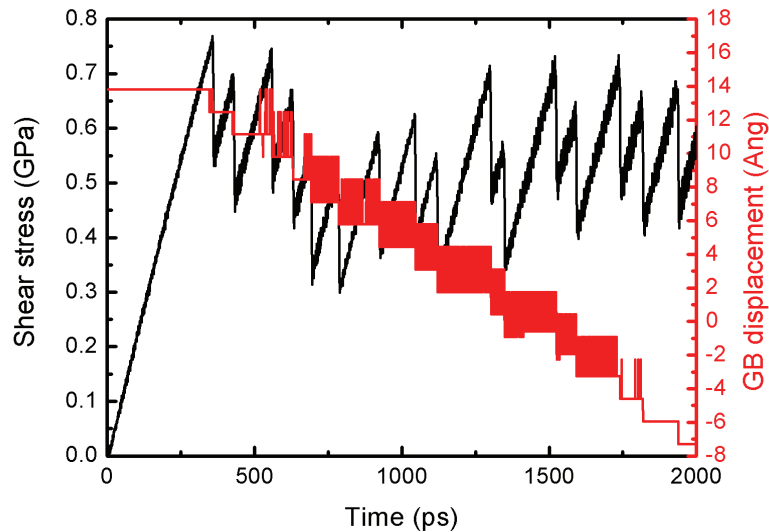


Figure 4.54 Shear stress–time (black) and GB displacement–time (red) curves of the one O sample with a $\Sigma 21$ GB simulated at 100 K. The origin of the “GB displacement” axis is chosen to be at level of the impurities.

If the number of O atoms is increased to four and sixteen, the reduction of shear stress is more significant, especially in the latter case (Figure 4.55). According to Figure 4.55b the motion of the GB is nearly stopped at the level of the 16 O impurities. An increase in maximal stress is observed after the GB has reached the plane containing the O atoms. The figure could even suggest a change in mechanism from coupled GB motion to e.g. GB sliding. However these speculations can not be confirmed as the data of the atomic structures for all the impure cases has been lost before the simulations have finished. Currently the simulations are rerun to clarify the detailed mechanisms.

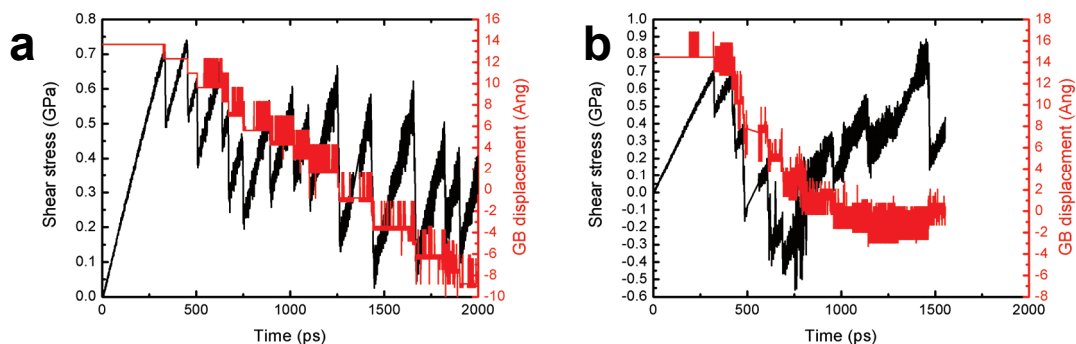


Figure 4.55 Shear stress–time (black) and GB displacement–time (red) curves of the four O sample (a) and a sixteen O sample (b) with a $\Sigma 21$ GB simulated at 100 K. The origin of the “GB displacement” axes is chosen to be at level of the impurities.

4.3.5 Discussion

The effect of O impurities on the mobility of GB is tested within the framework of coupled GB migration. In all the simulated cases, O atoms have never segregated towards the GB or have moved with the migrating GB. However diffusive processes which are necessary to observe these effects are suppressed by the low simulation temperature and by the given time-scales. According to the short time-scales, GBs are moving with a tremendous speed compared to experimental values which gives the O impurities no chance to accommodate in more favorable positions, e.g. in the GB. Additionally the expected picture of impurities segregating to the defects, e.g. GBs, is not reproduced here since the simulation temperature is too low to move solute atoms from their well-relaxed lattice position towards the GBs. Instead of letting the impurities move and segregate to GBs, the presented simulations can be interpreted as a try to study GB/impurity effects by forcing the GB to move towards or over the impurities. It is e.g. seen that GBs approach the plane containing the O defects faster than pure planes, which might be linked to the affinity between impurities and defects such as GBs. This means, the increase in normal velocity of the GB when it approaches the O atoms could be caused by the attractive force between the impurities and the GB. In this case the mobile GB is moved to the stationary impurities however the same attractive force could lead to segregation of mobile impurities to stationary GBs.

Further, it is shown that the change in global shear stress due to impurities arises locally around the defect atom (see Figure 4.38 in section 4.3.3.2). This shows remarkably that impurities which produce strain and stress fields interact with the stress field of other defects, such as the GB in this case. This corresponds to the understanding for interactions of impurities (e.g. solute atoms or precipitates) with defects. The interstitial O atom shows a higher maximal critical shear stress than the substitutional. This corresponds with the expectations in Ref. ¹⁸⁸, which mention that the interstitial impurity perturbs the atomic configuration and the bonding more than a substitution. Using the given potential (the first potential presented in section 3.2) shows the preference of the O atom to be in the lattice as substitution instead of being in the [100]-dumbbell interstitial site. This can be seen from the change of position during the simulation and from the energy of the final configuration which is lower than the initial energy. This result is dependent on the potential and has not been confirmed or disproved by ab initio calculations or experiments, so far. Again the accommodation processes can be questioned due to the high velocity of the GB, the short time-scales and the missing temperature.

In the case of the inhomogeneous O distribution and the corundum structure using the second potential a large distortion remains in the sample after the GB passed the O atoms or the

precipitate. The resulting structure might be an artifact caused by the high stress, athermal simulation conditions. Possibly, these distortions of the lattice could anneal out if the same samples are simulated at a smaller strain-rate and/or at finite temperature. However the EAM potential can also have some influence as for the first potential no comparable distortion of the lattice after the GB passes the inhomogeneous O distribution is observed.

The use of different potentials and samples showed that results can change in values obtained so quantitative predictions are precarious. Independent of the potential, results show important qualitative effects e.g. a drag of GB due to impurities. This drag effect is most pronounced for the highest O concentrations in both samples ($\Sigma 75$ and $\Sigma 21$). The publications by Lucke, Detert, Cahn and Stuwe³⁹⁻⁴¹ claimed decades ago that impurities can reduce the mobility of GBs significantly. A drag effect for GB is reported for small amounts of soluble, foreign atoms. This literature trend of reduced interface mobility due to impurities is very obvious in the case of inhomogeneously distributed O atoms, where the GB can move freely on the side without impurities and is significantly pinned at the impurities on the other side. Similar changes in critical shear stresses can be expected in experiments. The reduction of the mobility of interfaces such as GBs can also be used as an experimental observation criterion for the influence of impurities. A possible indication for the validity of the observed trends is the fact that the grain growth is more pronounced in purer samples as reported by Gianola and co-workers⁵³. However experimental conditions are generally much more complex and various side effects could blur these results. In the case of grain growth it can e.g. not be excluded that an oxide layer on the surface passivates internal processes.

Detailed spatial and temporal analysis of the actual GB migration events for both the pure Al and homogeneous AIO systems reveal no initially local process – the GBs do not migrate locally with for example a subsequent migration of a GB step that eventually results in the migration of the entire GB – even at 100 K temperature. This observation can be expected due to the imposed periodicity and choice of relatively short periodic lengths forcing the coupled GB migration event to be a collective process that occurs globally over the entire GB plane. In contrast, migration of GBs in the cases of the inhomogeneous O distributions happens locally. It is envisaged that using much larger samples such local processes could begin to occur at finite temperature due to local fluctuations at the GB. This is especially expected for the presence of O atoms which affect significantly the critical stress required for migration to occur. For example, a large bi-crystal sample has a planar distribution of O at surface densities much smaller than considered here, it is expected that “isolated” O could pin locally the GB leading to a GB step structure that accommodates the different levels of GB migration within the sample as a function of distance from the O defect.

In summary, coupled GB migration in Al bicrystals has been studied under the presence of O impurities. Some of the observed effects, e.g. the reduced mobility of the GB, are in good agreement with the existing literature on GB/impurities effects which affect the mobility of GBs. Other effects, such as impurities which segregate to the GB or move with the propagating GB could not be observed as the simulation temperatures are too low and the simulation method used is too limited in time-scale. Accelerated molecular dynamics methods^{126, 127, 189, 190}, which are successfully used by Mishin and Voter¹⁹¹, could help to solve the time-scale issue.

5 Discussion

5.1 Applications

5.1.1 Samples and simulation conditions

5.1.1.1 Samples

As there is little knowledge on simulations of nonmetallic impurities in metals, especially in nc metals, a representative selection of configurations is made. Less complex simulation geometries, such as bicrystals or the dislocation sample which consists of mainly one grain and its nc environment, are more powerful in enlightening the possible role of impurities since a smaller number of processes happen in these samples at the same time. In all applications in chapter 4 the O distribution is modified to enhance the impact of the O impurities. E.g. in the case of the nc sample, the O distribution is embedded in triple junctions, because this could anchor the microstructure and consequently influence the mechanical behavior. Additionally, the O distribution is modified according to observations of dislocations in the pure sample. In the cases of dislocation propagation and/or coupled GB migration, many different O distributions are tested with different impact of the impurities. In both cases a stronger effect is achieved if the homogeneity in the structure is broken either by distributing O impurities in an inhomogeneous way (coupled GB migration) or by putting the O atom in the normally homogenous center of the grain (dislocation propagation).

5.1.1.2 Simulation conditions

As thermal motion of atoms produces noise which can cover effects of interest, a restriction to lower temperatures or even 0 K is frequently done in this work by using the MS method. It gives access to a series of intermediate configurations which are connected by physical events and it successfully removes thermal noise which facilitates the comparison between different simulations such as pure and impure. However there are pitfalls in the usage of this method: MS is developed to relax the potential energy of a given configuration, i.e. moving atoms of an initial configuration to a configuration which corresponds to a local minimum in potential energy. The intermediate configurations are physically less meaningful as they are at most stationary points of the potential energy surface. Using MS means, that one simulates athermally. In this athermal limit processes have no concept of time. So a comparison of process rates or velocities is difficult. Moreover processes such as dislocation propagation, pinning and unpinning, which are known to be thermally activated⁶⁶, are made active by applying stresses which are higher than in the corresponding finite temperature simulations. As an example, the critical shear stress in the pure $\Sigma 75$ coupled GB migration simulation is reduced by 30 MPa if

the simulation is executed with 100 K MD instead of MS. In case of the inhomogeneous O distribution (Figure 4.46) and in the case of the corundum precipitate (Figure 4.49) in the $\Sigma 75$ sample a huge distortion of the lattice is observed when the GB passes the impurities using the second potential. These distortions could be an artifact of the simulation athermal conditions. Another consequence of athermal simulations is that processes are less sensitive to the given environment and corresponding stress concentration. Athermal simulations bulldozes through energy barriers which might be important in the experimental regime. Chang and Chen also report on the reduced sensitivity in athermal simulations and even conclude that MS is “not a suitable method for the studying the behavior of nanomaterials beyond the elastic limit”¹⁹². In the lower stress regime at finite temperature (or lower strain rate), processes are much more diverse, e.g. more dislocation cross-slip can appear, as Brandl et al. recently showed⁷². This is especially an issue in the simulations of the dislocation propagation which have been performed with MS and therefore in the athermal limit. Additionally, there is the effect of global quenching which produces rather unphysical events during the relaxation. Global quenching means that velocities of all the atoms are simultaneously removed, when a maximum in kinetic energy is reached. Two alternatives to MS with global quench are tested as case-studies: MD at 1 K (Figure 5.1) and MS with local quenching (Figure 5.2). In case of the 1 K MD simulation the process of dislocation propagation for the pure sample presented in section 4.2.3.1 is studied. It is not changed much compared to the corresponding MS simulation with global quench and the shear stress evolution curve follows the same trends. However the kinks due to quenching are not present any more (Figure 5.1).

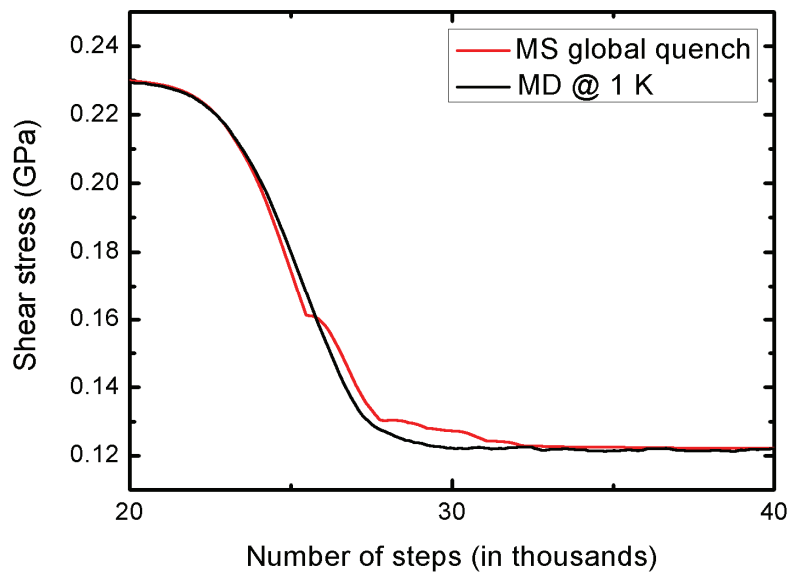


Figure 5.1 Pure sample with 1 K MD (black) or MS using global quenching (red).

In the other case (Figure 5.2) the “IG-I2” sample presented in section 4.2.3.7 is studied using MS with local quenching. Local quenching means that the atomic velocities are removed individually if the scalar product between the acceleration and the velocity of an atom is negative. It is observed that the dislocation still propagates. It also overcomes the local pinning sites caused by the impurities in a similar way as in the MS simulation using global quenching. However the simulation with local quenching (Figure 5.2: red curve) requires a order of magnitude more relaxation steps than in the case of global quenching (Figure 5.2: black curve). Due to the small differences in the resulting dislocation propagation behavior between MS with local and global quenching and due to the long simulation time in the case of local quenching, no other sample are tested using MS with local quenching.

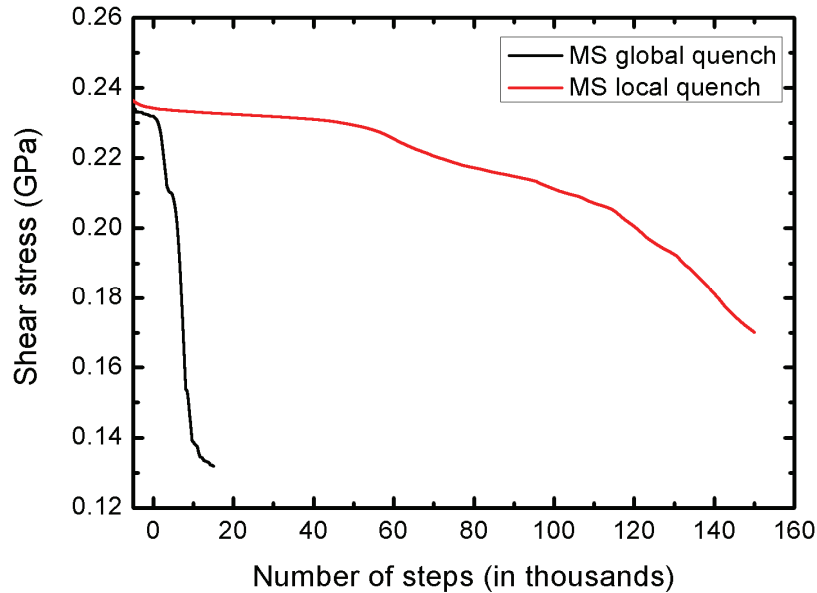


Figure 5.2 The “IG-I2” sample with global (black) and local (red) quenching.

5.1.2 Performance of the method

5.1.2.1 Nanocrystalline samples

Thanks to the local chemical potential approach and to the EAM potential with shorter cutoff distances it is possible to simulate the deformation of an nc sample with more than 1.2 million atoms and impurities. This simulation is performed using 64 parallel cores on the Palu system of the Swiss National Supercomputing Center (CSCS). The simulation sample is modified to have the same number of neutral clusters as having computing cores in order to obtain a good load balancing. An MD time-step in the simulation takes about 3.7 seconds wall clock time without charge update but with calculation of the electrostatic energies, forces and stresses. The charge

update is performed in every 10th time-step. Those MD steps with charge update take less than 12 seconds. So an average MD step takes less than 5 seconds wall clock time. This is about a magnitude more than the underlying EAM implementation for pure Al which performs on the corresponding pure sample using the same number of cores at about 0.5 seconds per time-step.

The major limitation of the developed method in this application is the fact that atoms move too close to each other in the impure case. This leads to a stop of the whole simulation at a strain of about 6.5% because the electrostatic part is not solvable any more for atoms which are so close. A partial reason might lay in the parameterization of the first potential. Especially the repulsion at very short distances is too weak and for the case of O-O interactions even attractive. This is a result which can happen in a fitting procedure and which can be improved by artificially adding a repulsive contribution to the very short-range of the potential.

5.1.2.2 Dislocation propagation

For the simulation of dislocation propagation first the serial and later the parallel implementation on 8 cores are used. In both cases the performance is dependent on the O distribution. In the computationally worst case where the of O atoms are distributed in the whole slip plane of the dislocation in the sample with about 275000 atoms, the average MD time-step takes a wall clock time of less than 3 seconds on the Rosa supercomputer at CSCS. In the serial case the same sample can be simulated in about 35 seconds per time-step without charge update and 70 seconds with charge update. The average time-step is then of the order of 40 seconds which is still a large improvement compared to the beginning where only the charge update of 4 O in 13500 Al took 22.5 minutes (however on a slower computer).

5.1.2.3 Coupled grain boundary migration

All the simulations of coupled GB migration are performed in serial computation. The wall clock time during the simulation depends on the amount of O impurities and on their distribution. In case of only one O atom in the $\Sigma 75$ sample (24000 atoms) an average MD time-step took about 2.3 seconds without charge update and 3.2 seconds with charge update. The average MD step with charge update in every tenth step takes about 2.5 seconds. In the computationally worst case of the $\Sigma 75$ sample with 16 impurities the wall clock time of a MD step is between 20 seconds without charge update and 40 seconds with charge update.

5.1.2.4 Time-scale issue

The time-scale limit of MD is for most applications a constriction. As the implemented method for the simulation of impurities brings additional computational costs, a restriction to smaller simulation times has to be done. The time-scale limitation which is present in both pure and

impure simulations and which leads to the very high strain rates makes it difficult to compare simulation results to experimental findings. However simulations might help to uncover causes of processes or mechanisms among which impurities play an important role.

5.2 Developments

5.2.1 Local chemical potential approach

The local chemical potential approach offers faster access to charges in sub-regions of samples around isolated O atoms or clusters of O atoms by excluding a large fraction of atoms from the charge update. Such an approach reduces the computational cost in the case of dilute O impurities as fewer charges have to be calculated. This is especially true, when O impurities are grouped in well separated clusters as it is done for the impure nc samples (section 4.1). A distribution of small O clusters or isolated O atoms in GBs and grains could also match Gianola's descriptions^{60, 187}. He did not measure a higher O concentration in GBs using EELS and he did not find any buried O layers using Auger depth profiling. Although the scenario of O layers and especially oxide surfaces has not been the focus in the development, the method can give some improvement if many metallic atoms are far enough from the oxide and are therefore neglected in the charge optimization. Considering for example a sample (Figure 5.3a) with a thin layer of amorphous oxide (yellow atoms) on the top, a large fraction of atoms can be neglected from charge optimization: If Al atoms are further than the constrained buffer region (red atoms) given by the selected cutoff away from all O atoms, they are excluded from the charge update procedure by the classification scheme presented in section 3.1.3.

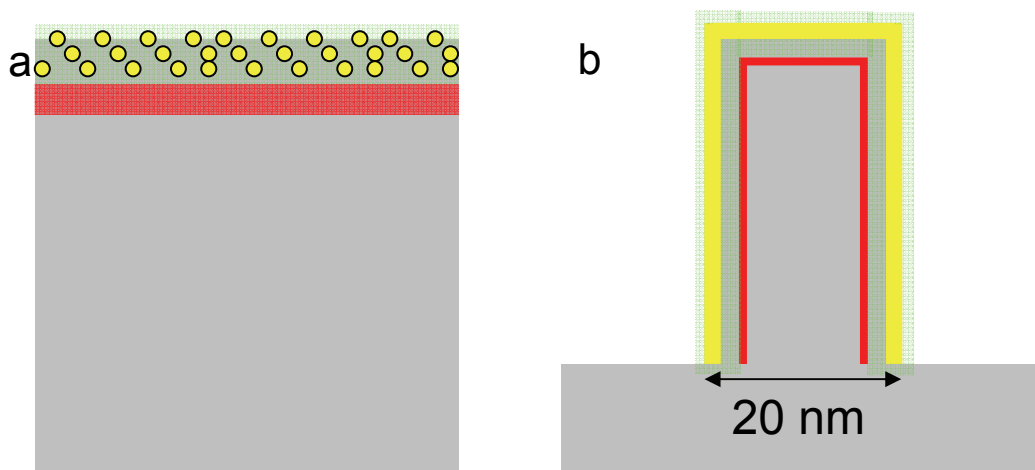


Figure 5.3 (a) Sample with a layer of O atoms at the top. (b) Cross section through a cylindrical nano-pillar with an O layer at the surface. Yellow indicates O atoms, green are regions with full charge optimization, red regions are constrained in the charge update and grey regions represent atoms being neglected in the charge update according to Figure 3.3.

In a similar way, the local chemical potential approach makes the simulation of a nano-pillar with an oxide layer on the surface (Figure 5.3b) considerable. Assuming a cylindrical Al nano-pillar with 20 nm cross section and 40 nm height the sample contains approximately 800000 atoms (760000 fcc Al atoms and 40000 O atoms at the surface) ignoring the base. Assuming further, that the O atoms (yellow) are present only at the surface and the charge transfer involves only the outer 2 nm (green and red atoms), a pillar of 16 nm cross section and 38 nm height can be neglected from the charge update. These are about 450000 atoms or more than half of the atoms. Still, solving a charge optimization problem which involves a system of 350000 atoms is very demanding.

The technical implementation of the method is largely based on the reformulation of Streit and Mintmire's optimization problem using Lagrange multiplier notation. This improves also the computational efficiency of solution of the global charge update compared to the publication by Vashishta and Nakano¹⁵⁶. In the publication, it is suggested performing the charge update by solving two linear systems of equations whereas here only one system is solved.

The concept of local chemical potentials is transferable. One can think e.g. of properties which are computed globally although they have more a local character and maybe also a large screening such as magnetism.

Implementation

The serial implementation is powerful. The clustering based on graph theory, where only the positions of the O atoms are represented as a graph, is a computationally very efficient way for labeling the atoms. The application of a commercial or open-source solver library (in this case UMFPACK¹⁷²⁻¹⁷⁵) shows a significant performance improvement compared to self-programmed solution routines for standard problems such as linear systems of equations. Manual programming according to a recipe (e.g. Numerical recipes¹⁸³) in combination with automated code generator for the given computer architecture can be an alternative for the future.

The parallel code is developed based on the assumption of a dilute O distribution in many small neutral sub-regions. These sub-regions can be distributed to different computing cores. In the case where the first assumption is fulfilled, the efficiency and the load balancing is good. This however limits the distribution of O atoms a lot. The O concentration has to be sufficiently dilute and distances between O atoms have to be large enough to be able to send different sub-regions to different computing cores. In case of a small number of neutral sub-regions (e.g. much smaller than the number of cores) and/or large sub-regions the load balancing is bad. In

the worst case charges for one huge sub-region have to be optimized on one core and all the others computing cores are idling at the same time. This would be the case in the example of the nano-pillar (Figure 5.3b). A possible solution to improve the load balancing is to distribute the information of the whole charge optimization problem (i.e. equation 30) and solve it on all cores by using a parallel solver for linear systems of equations. This has been tested by Dr. Olivier Politano however it is not implemented in the current version of the code.

So far, the architecture of state of the art parallel computers, i.e. several execution nodes with more than one multi-core processor which access the same memory, has not been exploited: Parallelization is only obtained from message passing (MPI) between the cores which means data is assumed to be separated between cores. However, cores belonging to the same node access the same memory. Therefore a hybrid OpenMP/MPI-implementation saves communication costs.

The precision is for some properties e.g. the stresses or even the charges not very crucial to obtain satisfactory results or sufficiently good energy conservation. For these properties a restriction to single precision instead of double precision can increase the performance. (Currently all the properties are calculated in double precision.) In case of a clear separation of tasks which have to be calculated in single precision (e.g. charge optimization) and in double precision (e.g. force and position update) the use of future hybrid (CPU and GPU) architectures can open new perspectives. GPUs have e.g. an overwhelming performance on single precision computation. GPUs with more than a teraflop performance on one processor exist now.

5.2.2 EAM potentials

Two potentials have been developed based on ab initio data. For one of them also properties of the α -corundum structure have been included in the fitting. Both potentials are applied in the simulation of O impurities in Al. Reduced cutoff distances give significant improvement in the performance. In a few cases the simulations are executed using both potentials which allows for direct comparison. In cases of pure simulations no change is observed, because both potentials use the same Al-Al interaction which is based on Mishin-Farkas Al potential¹⁷⁸. However in the impure case, e.g. in the simulation of the coupled GB motion, a change in critical or maximal stresses is observable for the two potentials (see Figure 4.40 and Figure 4.42). As suggested by Figure 3.9, the second potential causes a stress distribution around impurities which is of shorter range but higher in absolute values. Still the overall trends observed in coupled GB migration are preserved by switching between the potential.

How representative the database used in the fitting is and whether the set of calculated and fitted properties is large enough to call the potential “accurate” is questionable. Weaknesses are obvious for the first potential as e.g. the corundum structure can not be modeled correctly: The electrostatic parameters have not been adjusted after the exchange of the orbital functions which leads to wrong charges for corundum structure and therefore an incorrect description of corundum’s electrostatic interactions. The corundum structure has also never been considered in the fitting of the first potential. As a result, the first potential models the non-electrostatic interactions in corundum in an unlikely way, which leads to instabilities of the structure.

The second version of the potential, which takes the corundum structure explicitly into account in the fitting, is able to preserve it. In the fitting elastic constants are used to make the model of the corundum structure more stable to distortions. However the resulting description of the corundum structure is still very fragile. Possible reasons are internal stresses which could not be entirely removed in the fitting. As a result, the corundum structure can transform to another corundum structure which uses different internal parameters for its description. Due to the fragility of corundum, the second potential should be applied carefully under well-selected conditions (e.g. at temperatures clearly below room temperature).

5.2.2.1 Changes in the electrostatics

Figure 3.2 shows that the charge on a single O is significantly reduced in absolute value compared to the charges in the corundum structure due to the non-stoichiometric ratio of Al and O atoms. The charge of the substitutional O atom is in the displayed case -1.166 e produced with Streitz and Mintmire’s potential¹⁰². If the orbital functions are changed from 1s orbitals for all atoms to 2s for O and 3s for Al without adjusting the electrostatic parameters, the same atom has a charge of -0.2250 e. In this case, the structure is relaxed using the first potential. In case of the second potential where the electrostatic parameters are modified in order to reproduce Streitz and Mintmire’s charges for the corundum structure the value of the same charge is -0.5143 e.

Whether one of these O charges is a good estimate for the real charge is hard to say as no comparison exists. In principle, it is possible, to calculate charges from DFT calculations by assigning contributions of the electronic densities to individual atoms which gives something like atomic charges (see Appendix B). However, tests have shown that these atomic charges are very dependent on the method of charge calculation and a comparison with values calculated in MD is difficult. Therefore charges are so far modified to reproduce the corundum charges, only. A further comparison is useful.

5.2.2.2 Underlying AI potentials

Both potentials have limitations and for the continuation of simulations of dilute O impurities in Al a new potential could be fitted. Here, for both potentials Mishin and Farkas Al potential published in “Physical Review B”¹⁷⁸ is used for the Al-Al interaction mainly to reproduce Mishin and Ivanov’s results on coupled GB migration. Depending on the application, one can also select other Al potentials such as the Mishin and Farkas potential which is published in the MRS proceedings¹⁸⁶ and which is frequently used in the Materials Science and Simulation group¹⁰⁷. There are minor differences between the potentials in terms of fitted properties, e.g. in the elastic constants, in the phonon frequencies, in the stacking fault energies and in the surface energies. Still a rather different behavior is observed if the MRS potential (analytical description instead of the spline-fitted PRB version) is applied e.g. in coupled GB migration: The shear stress-time curve changes its morphology from a saw-tooth-like curve (PRB) to a more sinusoidal curve (MRS) as shown in Figure 5.4. However the stick-slip process for the atomic motion is maintained which indicates again that coupled GB migration is a purely geometrical phenomenon. The mentioned difference can be explained by the known fact that the analytical potential of Mishin and Farkas¹⁸⁶ is soft at short range. This can also lead to differences in stress-strain curves for the deformation of nc samples or different critical athermal stress barriers for the pinning of dislocations. As the Materials Science and Simulation group uses the analytical version of the potential¹⁸⁶ more frequently than the spline fitted version¹⁷⁸ a refit of an empirical AIO potential on the basis of the analytical potential might be useful for a direct comparison of existing pure simulation data. The continuation of the usage of 2s and 3s orbitals is recommended in any case, however the electrostatic parameters should be improved by including them in the fitting procedure. In general, if corundum is reproduced sufficiently well by an empirical potential, the potential is more transferable. However including corundum in the fitting makes it more complicated and time consuming.

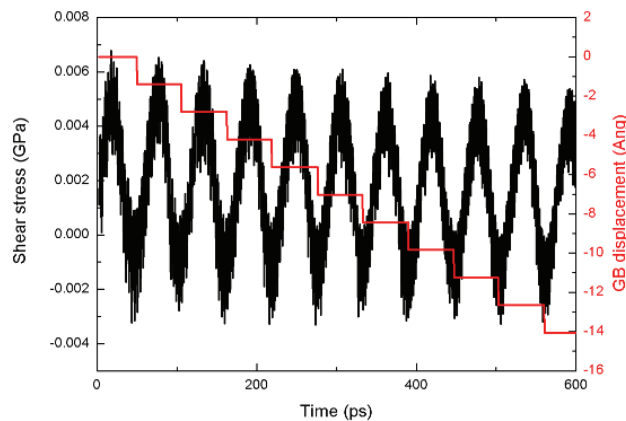


Figure 5.4 Shear stress-time (black) and GB displacement-time (red) curves of the pure $\Sigma 75$ sample simulated at 0 K using the empirical potential given in Ref.¹⁸⁶.

6 Conclusions and outlook

A method for the simulation of dilute O impurities in nc Al is presented. The development of the method is described and its possibilities and limitations are illustrated for three categories of applications. Many of these applications become accessible for simulation only through the gain in computational efficiency of the presented developments.

In all the applications, the focus is on the change of mechanical properties due to dilute O impurities in nc Al. In several cases one can see that impurities reduce the mobility of propagating defects such as dislocations or GBs which corresponds to existing knowledge. However the magnitude of change in mechanical properties, e.g. in case of the deformation of the nc sample are smaller than the one known from experiments (c.f. Gianola's work⁵³). This is on the one hand a reminder that simulation conditions are still far from experimental ones. (Especially athermal simulations bulldoze through energy barriers which might be important in the experimental regime.) On the other hand, it shows clearly that the method should be used to study processes and not quantities. In the best case the method can be used to develop new ideas for experiments, e.g. by studying specific O distributions and their effects, which can be a basis for comparison of future experiments.

The whole methodology used for the simulation of dilute O in Al is based on the framework of Streitz and Mintimire¹⁰². This work allows for MD simulations with variable charges. Electrostatic energies, forces and stresses can be explicitly added to the calculation by the usage of charges. However the computational effort to determine the charges is considerably large. This project reduces this effort significantly by introducing the local chemical potential approach for dilute O distributions. The method offers great prospective for the calculation of local properties by the application of local chemical potentials. Streitz and Mintimire potential¹⁰² has got other weaknesses, when it comes to the simulation of impurities, e.g. the long-range EAM potential for the non-electrostatic interaction. This is substituted by two alternatives for EAM potentials. Whether one of the fitted potential is sufficient to be applied in a broader context of simulations of impurities has been questioned. The whole method presented here should clearly be further developed to be able to compete with reality and/or experiments in the future.

Depending on the type of simulations the parallel implementation should be reconsidered and adapted to exploit modern supercomputer architectures more efficiently. A refitting of the EAM potential should be considered e.g. to be also able to simulate the more natural form of surface oxides which are amorphous. Beyond this, there is the concern about the physics, which is used in Streitz and Mintimire. The gain in physical accuracy due to the description of ionic bonding via variable charges compared to conventional MD using e.g. empirical EAM or MEAM

potentials might still not justify the computational efforts. Especially a comparison with the rather recent MEAM potential for AlO system by Sekkal and co-workers would be desirable⁹⁵. For the simulation of dilute impurities other approaches such as the embedded ion method (EIM)⁹¹ or the more bond order like charge transfer method by Albe¹⁹³ should be tested in terms of accuracy and efficiency. All these charge transfer methods are within the framework of classical molecular dynamics and remain empirical. As an alternative multi-scale method which locally simulated with ab initio techniques e.g. for the impurities and which simulate the metallic interaction in the big majority of the samples with conventional MD.

Independent of the choice of method, one should study many more simple and complex systems to gain more knowledge on the role of impurities in metals and in particular in nc metals.

References

- ¹ J. P. Hirth and J. Lothe, *Theory of Dislocations* (John Wiley & Sons, 1982).
- ² M. Legros, B. R. Elliott, M. N. Rittner, et al., *Philosophical Magazine a-Physics of Condensed Matter Structure Defects and Mechanical Properties* **80**, 1017 (2000).
- ³ J. C. M. Li, *Transactions of the Metallurgical Society of Aime* **227**, 239 (1963).
- ⁴ E. O. Hall, *Proceedings of the Physical Society of London Section B* **64**, 747 (1951).
- ⁵ N. J. Petch, *Journal of the Iron and Steel Institute* **174**, 25 (1953).
- ⁶ D. C. Chrzan, J. W. Morris, Y. N. Osetsky, et al., *MRS Bulletin* **34**, 173 (2009).
- ⁷ M. Legros, G. Dehm, E. Arzt, et al., *Science* **319**, 1646 (2008).
- ⁸ D. N. Seidman, E. A. Marquis, and D. C. Dunand, *Acta Materialia* **50**, 4021 (2002).
- ⁹ C. Molteni, G. P. Francis, M. C. Payne, et al., *Physical Review Letters* **76**, 1284 (1996).
- ¹⁰ C. Molteni, N. Marzari, M. C. Payne, et al., *Physical Review Letters* **79**, 869 (1997).
- ¹¹ J. C. Hamilton and S. M. Foiles, *Physical Review B* **65**, 064104 (2002).
- ¹² F. Sansoz and J. F. Molinari, *Acta Materialia* **53**, 1931 (2005).
- ¹³ L. Q. Chen and G. Kalonji, *Philosophical Magazine a-Physics of Condensed Matter Structure Defects and Mechanical Properties* **66**, 11 (1992).
- ¹⁴ M. Shiga and W. Shinoda, *Physical Review B* **70**, 054102 (2004).
- ¹⁵ N. Chandra and P. Dang, *Journal of Materials Science* **34**, 655 (1999).
- ¹⁶ A. J. Haslam, D. Moldovan, V. Yamakov, et al., *Acta Materialia* **51**, 2097 (2003).
- ¹⁷ C. H. Li, E. H. Edwards, J. Washburn, et al., *Acta Metallurgica* **1**, 223 (1953).
- ¹⁸ D. W. Bainbridge, C. H. Li, and E. H. Edwards, *Acta Metallurgica* **2**, 322 (1954).
- ¹⁹ M. Biscondi and C. Goux, *Memoires Scientifiques De La Revue De Metallurgie* **65**, 167 (1968).
- ²⁰ H. Fukutomi, T. Iseki, T. Endo, et al., *Acta Metallurgica Et Materialia* **39**, 1445 (1991).

- 21 M. Winning, G. Gottstein, and L. S. Shvindlerman, *Acta Materialia* **49**, 211
(2001).
- 22 M. Winning, G. Gottstein, and L. S. Shvindlerman, *Acta Materialia* **50**, 353
(2002).
- 23 A. D. Sheikh-Ali, J. A. Szpunar, and H. Garmestani, *Interface Science* **11**, 439
(2003).
- 24 H. Yoshida, K. Yokoyama, N. Shibata, et al., *Acta Materialia* **52**, 2349 (2004).
- 25 M. Legros, D. S. Gianola, and K. J. Hemker, *Acta Materialia* **56**, 3380 (2008).
- 26 F. Momprou, D. Caillard, and M. Legros, *Acta Materialia* **57**, 2198 (2009).
- 27 D. A. Molodov and L. S. Shvindlerman, *International Journal of Materials
Research* **100**, 461 (2009).
- 28 J. W. Cahn and J. E. Taylor, *Acta Materialia* **52**, 4887 (2004).
- 29 J. W. Cahn, Y. Mishin, and A. Suzuki, *Acta Materialia* **54**, 4953 (2006).
- 30 J. W. Cahn, Y. Mishin, and A. Suzuki, *Philosophical Magazine* **86**, 3965 (2006).
- 31 V. A. Ivanov and Y. Mishin, *Physical Review B* **78**, 064106 (2008).
- 32 H. Zhang, D. Duy, and D. J. Srolovitz, *Philosophical Magazine* **88**, 243 (2008).
- 33 D. A. Molodov, V. A. Ivanov, and G. Gottstein, *Acta Materialia* **55**, 1843
(2007).
- 34 M. Winning, *Philosophical Magazine* **87**, 5017 (2007).
- 35 N. Bernstein, *Acta Materialia* **56**, 1106 (2008).
- 36 Y. Mishin, M. Asta, and J. Li, *Acta Materialia* **58**, 1117 (2010).
- 37 A. P. Sutton and R. W. Balluffi, *Interfaces in Crystalline Materials* (Clarendon
Press, Oxford, 1995).
- 38 D. Caillard, F. Momprou, and M. Legros, *Acta Materialia* **57**, 2390 (2009).
- 39 K. Lucke and K. Detert, *Acta Metallurgica* **5**, 628 (1957).
- 40 K. Lucke and H. P. Stuwe, *Acta Metallurgica* **19**, 1087 (1971).
- 41 J. W. Cahn, *Acta Metallurgica* **10**, 789 (1962).
- 42 D. I. Thomson, V. Heine, M. W. Finnis, et al., *Philosophical Magazine Letters*
76, 281 (1997).
- 43 D. I. Thomson, V. Heine, M. C. Payne, et al., *Acta Materialia* **48**, 3623 (2000).
- 44 J. R. Rice and J. S. Wang, *Materials Science and Engineering a-Structural
Materials Properties Microstructure and Processing* **107**, 23 (1989).
- 45 E. Arzt, *Acta Materialia* **46**, 5611 (1998).
- 46 U. F. Kocks and H. Mecking, *Progress in Materials Science* **48**, 171 (2003).

- 47 K. S. Kumar, S. Suresh, M. F. Chisholm, et al., *Acta Materialia* **51**, 387 (2003).
- 48 M. W. Chen, E. Ma, K. J. Hemker, et al., *Science* **300**, 1275 (2003).
- 49 X. L. Wu and E. Ma, *Applied Physics Letters* **88**, 231911 (2006).
- 50 Z. Budrovic, H. Van Swygenhoven, P. M. Derlet, et al., *Science* **304**, 273 (2004).
- 51 S. Brandstetter, Z. Budrovic, S. Van Petegem, et al., *Applied Physics Letters* **87**, 231910 (2005).
- 52 T. Ungar, J. Gubicza, G. Ribarik, et al., *Journal of Applied Crystallography* **34**, 298 (2001).
- 53 D. S. Gianola, S. Van Petegem, M. Legros, et al., *Acta Materialia* **54**, 2253 (2006).
- 54 K. Zhang, J. R. Weertman, and J. A. Eastman, *Applied Physics Letters* **87**, 061921 (2005).
- 55 X. Z. Liao, A. R. Kilmametov, R. Z. Valiev, et al., *Applied Physics Letters* **88**, 021909 (2006).
- 56 S. Brandstetter, K. Zhang, A. Escudro, et al., *Scripta Materialia* **58**, 61 (2008).
- 57 T. J. Rupert, D. S. Gianola, Y. Gan, et al., *Science* **326**, 1686 (2009).
- 58 C. C. Koch, R. O. Scattergood, K. A. Darling, et al., *Journal of Materials Science* **43**, 7264 (2008).
- 59 S. Brandstetter, *Deformation Mechanisms of Nanocrystalline Nickel Studied by In-situ X-Ray Diffraction* (Ecole Polytechnique Federal (EPFL), Lausanne, 2008).
- 60 D. S. Gianola, *Deformation mechanisms in nanocrystalline aluminum thin films: an experimental investigation*, Baltimore, Maryland, 2007).
- 61 J. Schiotz, F. D. Di Tolla, and K. W. Jacobsen, *Nature* **391**, 561 (1998).
- 62 J. Schiotz and K. W. Jacobsen, *Science* **301**, 1357 (2003).
- 63 J. Schiotz, T. Vegge, F. D. Di Tolla, et al., *Physical Review B* **60**, 11971 (1999).
- 64 H. Van Swygenhoven, *Science* **296**, 66 (2002).
- 65 H. Van Swygenhoven, *Nature Materials* **5**, 841 (2006).
- 66 H. Van Swygenhoven, P. M. Derlet, and A. G. Froseth, *Acta Materialia* **54**, 1975 (2006).
- 67 H. Van Swygenhoven, P. M. Derlet, and A. Hasnaoui, *Physical Review B* **66**, 024101 (2002).

- 68 E. Bitzek, C. Brandl, P. M. Derlet, et al., *Physical Review Letters* **100**, 235501 (2008).
- 69 E. Bitzek, C. Brandl, D. Weygand, et al., *Modelling and Simulation in Materials Science and Engineering* **17**, 055008 (2009).
- 70 E. Bitzek, P. M. Derlet, P. Andersen, et al., *Acta Materialia* **56**, 4846 (2008).
- 71 C. Brandl, E. Bitzek, P. M. Derlet, et al., *Applied Physics Letters* **91**, 111914 (2007).
- 72 C. Brandl, P. Derlet, and H. Van Swygenhoven, *Philosophical Magazine* **89**, 3465 (2009).
- 73 A. S. Argon and S. Yip, *Philosophical Magazine Letters* **86**, 713 (2006).
- 74 B. J. Pestman, J. T. M. De Hosson, and V. Vitek, *Philosophical Magazine a-Physics of Condensed Matter Structure Defects and Mechanical Properties* **64**, 951 (1991).
- 75 M. de Koning, R. J. Kurtz, V. V. Bulatov, et al., *Journal of Nuclear Materials* **323**, 281 (2003).
- 76 M. de Koning, R. Miller, V. V. Bulatov, et al., *Philosophical Magazine a-Physics of Condensed Matter Structure Defects and Mechanical Properties* **82**, 2511 (2002).
- 77 M. P. Dewald and W. A. Curtin, *Modelling and Simulation in Materials Science and Engineering* **15**, S193 (2007).
- 78 H. Jang and D. Farkas, *Materials Letters* **61**, 868 (2007).
- 79 Z. H. Jin, P. Gumbsch, K. Albe, et al., *Acta Materialia* **56**, 1126 (2008).
- 80 Z. H. Jin, P. Gumbsch, E. Ma, et al., *Scripta Materialia* **54**, 1163 (2006).
- 81 M. A. Tschopp, D. E. Spearot, and D. L. McDowell, in *Dislocations in Solids, A Tribute to F.R.N. Nabarro*, edited by J. P. Hirth (Elsevier, 2008), Vol. 14, p. 43.
- 82 D. Farkas, S. Mohanty, and J. Monk, *Physical Review Letters* **98**, 165502 (2007).
- 83 V. Yamakov, D. Moldovan, K. Rastogi, et al., *Acta Materialia* **54**, 4053 (2006).
- 84 D. Farkas, A. Froseth, and H. Van Swygenhoven, *Scripta Materialia* **55**, 695 (2006).
- 85 P. C. Millett, R. P. Selvam, and A. Saxena, *Materials Science and Engineering a-Structural Materials Properties Microstructure and Processing* **431**, 92 (2006).
- 86 P. C. Millett, R. P. Selvam, and A. Saxena, *Acta Materialia* **54**, 297 (2006).
- 87 P. C. Millett, R. P. Selvam, and A. Saxena, *Acta Materialia* **55**, 2329 (2007).

- 88 P. C. Millett, R. P. Selvan, S. Bansal, et al., *Acta Materialia* **53**, 3671 (2005).
- 89 L. A. Zepeda-Ruiz, G. H. Gilmer, B. Sadigh, et al., *Applied Physics Letters* **87**,
231904 (2005).
- 90 R. K. Rajgarhia, S. W. Koh, D. Spearot, et al., *Molecular Simulation* **34**, 35
(2008).
- 91 X. W. Zhou and F. P. Doty, *Physical Review B* **78**, 224307 (2008).
- 92 D. W. Brenner, *Physical Review Letters* **63**, 1022 (1989).
- 93 M. I. Baskes, *Physical Review Letters* **59**, 2666 (1987).
- 94 M. I. Baskes, *Physical Review B* **46**, 2727 (1992).
- 95 W. Sekkal and A. Zaoui, *Physica B-Condensed Matter* **404**, 335 (2009).
- 96 K. Govers, S. Lemehov, M. Hou, et al., *Journal of Nuclear Materials* **366**, 161
(2007).
- 97 K. Govers, S. Lemehov, M. Hou, et al., *Journal of Nuclear Materials* **376**, 66
(2008).
- 98 R. A. Buckingham, *Proceedings of the Royal Society of London Series a-
Mathematical and Physical Sciences* **168**, 264 (1938).
- 99 B. G. Dick and A. W. Overhauser, *Physical Review* **112**, 90 (1958).
- 100 M. Stoneham, J. Harding, and T. Harker, *MRS Bulletin* **21**, 29 (1996).
- 101 G. J. Dienes, D. O. Welch, C. R. Fischer, et al., *Physical Review B* **11**, 3060
(1975).
- 102 F. H. Streitz and J. W. Mintmire, *Physical Review B* **50**, 11996 (1994).
- 103 A. Yasukawa, *Jsme International Journal Series a-Mechanics and Material
Engineering* **39**, 313 (1996).
- 104 T. Iwasaki and H. Miura, *Journal of Materials Research* **16**, 1789 (2001).
- 105 A. C. T. van Duin, S. Dasgupta, F. Lorant, et al., *Journal of Physical Chemistry
A* **105**, 9396 (2001).
- 106 A. Nakano, R. K. Kalia, K. Nomura, et al., *Computational Materials Science* **38**,
642 (2007).
- 107 H. Van Swygenhoven, *Materials Science and Simulation, NUM-ASQ, Paul
Scherrer Intitiut*, <http://mss.web.psi.ch>, (2010).
- 108 R. Car and M. Parrinello, *Physical Review Letters* **55**, 2471 (1985).
- 109 P. Hohenberg and W. Kohn, *Physical Review B* **136**, B864 (1964).
- 110 W. Kohn and L. J. Sham, *Physical Review* **140**, 1133 (1965).
- 111 F. Jensen, *Introduction to computational chemistry* (Wiley, Chichester, 2007).

- 112 E. Kaxiras, *Atomic and electronic structure of solids* (Cambridge University
Press, Cambridge MA, 2003).
- 113 P. E. Blochl, *Physical Review B* **50**, 17953 (1994).
- 114 G. Kresse and J. Furthmüller, *Physical Review B* **54**, 11169 (1996).
- 115 G. Kresse and J. Furthmüller, *Computational Materials Science* **6**, 15 (1996).
- 116 G. Kresse and J. Hafner, *Physical Review B* **47**, 558 (1993).
- 117 G. Kresse and J. Hafner, *Physical Review B* **49**, 14251 (1994).
- 118 G. Kresse and D. Joubert, *Physical Review B* **59**, 1758 (1999).
- 119 J. P. Perdew, K. Burke, and M. Ernzerhof, *Physical Review Letters* **77**, 3865
(1996).
- 120 J. P. Perdew, K. Burke, and M. Ernzerhof, *Physical Review Letters* **78**, 1396
(1997).
- 121 M. P. Allen and D. Tildesley, *Computer simulation of liquids* (Clarendon Press,
Oxford, 1996).
- 122 D. Frenkel and B. Smit, *Understanding molecular simulation* (Academic Press,
San Diego CA, 2002).
- 123 D. Rapaport, *The art of molecular dynamics simulation* (Cambridge University
Press, Cambridge, 2004).
- 124 G. S. Heffelfinger, *Computer Physics Communications* **128**, 219 (2000).
- 125 H. Van Swygenhoven and P. M. Derlet, in *Dislocations in Solids, A Tribute to
F.R.N. Nabarro*, edited by J. P. Hirth (Elsevier, 2008), Vol. 14, p. 1.
- 126 A. F. Voter, *Journal of Chemical Physics* **106**, 4665 (1997).
- 127 A. F. Voter, *Physical Review Letters* **78**, 3908 (1997).
- 128 L. Verlet, *Physical Review* **159**, 98 (1967).
- 129 W. G. Hairer E., *Stiff and differential-algebraic problems* (Springer, Berlin,
2002).
- 130 J. E. Lennard-Jones, *Proceedings of the Physical Society* **43**, 461 (1931).
- 131 M. W. Finnis, A. T. Paxton, D. G. Pettifor, et al., *Philosophical Magazine a-
Physics of Condensed Matter Structure Defects and Mechanical Properties* **58**,
143 (1988).
- 132 D. Raabe, *Computational materials science* (Wiley-VCH, Weinheim, 1998).
- 133 M. W. Finnis and J. E. Sinclair, *Philosophical Magazine a-Physics of Condensed
Matter Structure Defects and Mechanical Properties* **50**, 45 (1984).
- 134 F. Cleri and V. Rosato, *Physical Review B* **48**, 22 (1993).

- 135 M. S. Daw and M. I. Baskes, Physical Review Letters **50**, 1285 (1983).
- 136 R. A. Johnson, Physical Review B **39**, 12554 (1989).
- 137 M. Parrinello and A. Rahman, Journal of Applied Physics **52**, 7182 (1981).
- 138 M. Parrinello and A. Rahman, Physical Review Letters **45**, 1196 (1980).
- 139 J. D. Honeycutt and H. C. Andersen, J. Phys. Chem. **91**, 4950 (1987).
- 140 H. Tsuzuki, P. S. Branicio, and J. P. Rino, Computer Physics Communications
177, 523 (2007).
- 141 J. F. Lutsko, Journal of Applied Physics **64**, 1152 (1988).
- 142 J. Cormier, J. M. Rickman, and T. J. Delph, Journal of Applied Physics **89**, 99
(2001).
- 143 M. Samaras, P. M. Derlet, H. Van Swygenhoven, et al., Physical Review B **68**,
224111 (2003).
- 144 R. Iczkowski and J. L. Margrave, Journal of the American Chemical Society **83**,
3547 (1961).
- 145 R. G. Parr, R. A. Donnelly, M. Levy, et al., Journal of Chemical Physics **68**,
3801 (1978).
- 146 A. K. Rappe and W. A. Goddard, Journal of Physical Chemistry **95**, 3358
(1991).
- 147 C. C. J. Roothaan, Journal of Chemical Physics **19**, 1445 (1951).
- 148 S. G. Gibbon P., in *Quantum Simulations of Complex Many-Body Systems:
From Theory to Algorithms, Lecture Notes*, edited by M. D. Grotendorst J.,
Muramatsu A. (John von Neumann Institute for Computing, Juelich, Germany,
2002), Vol. 10, p. 467.
- 149 A. Y. Toukmaji and J. A. Board, Computer Physics Communications **95**, 73
(1996).
- 150 J. Kolafa and J. W. Perram, Molecular Simulation **9**, 351 (1992).
- 151 T. Campbell, R. K. Kalia, A. Nakano, et al., Physical Review Letters **82**, 4866
(1999).
- 152 A. Hasnaoui, O. Politano, J. M. Salazar, et al., Physical Review B **73**, 035427
(2006).
- 153 A. Hasnaoui, O. Politano, J. M. Salazar, et al., Surface Science **579**, 47 (2005).
- 154 S. Garruchet, A. Hasnaoui, O. Politano, et al., in *Diffusion in Materials: Dimat
2004, Pt I and 2*, 2005), Vol. 237-240, p. 145.

- 155 S. K. R. S. Sankaranarayanan and S. Ramanathan, Physical Review B **78**,
085420 (2008).
- 156 A. Nakano, Computer Physics Communications **104**, 59 (1997).
- 157 S. Ogata, T. J. Campbell, R. K. Kalia, et al., Computer Physics Communications
153, 445 (2003).
- 158 S. Ogata, H. Iyetomi, K. Tsuruta, et al., Journal of Applied Physics **86**, 3036
(1999).
- 159 X. W. Zhou, H. N. G. Wadley, J. S. Filhol, et al., Physical Review B **69**, 035402
(2004).
- 160 V. Tomar and M. Zhou, Physical Review B **73**, 174116 (2006).
- 161 J. G. Yu, S. B. Sinnott, and S. R. Phillpot, Physical Review B **75**, 085311
(2007).
- 162 X. W. Zhou and H. N. G. Wadley, Journal of Physics-Condensed Matter **17**,
3619 (2005).
- 163 P. Vashishta, M. E. Bachlechner, T. Campbell, et al., Progress of Theoretical
Physics Supplement, 175 (2000).
- 164 P. Deuffhard, *Newton methods for nonlinear problems : affine invariance and
adaptive alorithms* (Springer, Berlin, 2004).
- 165 S. K. R. S. Sankaranarayanan, E. Kaxiras, and S. Ramanathan, Energy &
Environmental Science **2**, 1196 (2009).
- 166 S. K. R. S. Sankaranarayanan, E. Kaxiras, and S. Ramanathan, Physical Review
Letters **102**, 095504 (2009).
- 167 J. D. Gale, C. R. A. Catlow, and W. C. Mackrodt, Modelling and Simulation in
Materials Science and Engineering **1**, 73 (1992).
- 168 I. Manassidis and M. J. Gillan, Journal of the American Ceramic Society **77**, 335
(1994).
- 169 M. Causa, R. Dovesi, C. Roetti, et al., Chemical Physics Letters **140**, 120
(1987).
- 170 L. Salasco, R. Dovesi, R. Orlando, et al., Molecular Physics **72**, 267 (1991).
- 171 C. Sousa, F. Illas, and G. Pacchioni, Journal of Chemical Physics **99**, 6818
(1993).
- 172 T. A. Davis, Acm Transactions on Mathematical Software **30**, 165 (2004).
- 173 T. A. Davis, Acm Transactions on Mathematical Software **30**, 196 (2004).

- 174 T. A. Davis and I. S. Duff, *Siam Journal on Matrix Analysis and Applications* **18**, 140 (1997).
- 175 T. A. Davis and I. S. Duff, *Acm Transactions on Mathematical Software* **25**, 1 (1999).
- 176 K. Refson, *Computer Physics Communications* **126**, 310 (2000).
- 177 J. D. Gale and A. L. Rohl, *Molecular Simulation* **29**, 291 (2003).
- 178 Y. Mishin, D. Farkas, M. J. Mehl, et al., *Physical Review B* **59**, 3393 (1999).
- 179 M. I. Baskes, SAND **96**, 8484C (1996).
- 180 E. W. Weissenstein, in *MathWorld - A Wolfram Web Resource*, Vol. 2009.
- 181 S. I. A. Abramowitz M., *Handbook of mathematical functions with formulas, graphs, and mathematical tables* (Dober Publications, New York, 1970).
- 182 S. Kirkpatrick, C. D. Gelatt, and M. P. Vecchi, *Science* **220**, 671 (1983).
- 183 W. H. Press, *Numerical recipes in Fortran: the art of scientific computing* (Cambridge University Press, Cambridge, 1994).
- 184 M. M. Ossowski, L. L. Boyer, M. J. Mehl, et al., *Physical Review B* **66**, 224302 (2002).
- 185 P. M. Derlet and H. Van Swygenhoven, *Physical Review B* **67**, 014202 (2003).
- 186 Y. Mishin, D. Frakas, M. J. Mehl, et al., in *Mat. Res. Soc. Symp. Proc.* (Materials Research Society, 1999), Vol. 538, p. 533.
- 187 D. S. Gianola, B. G. Mendis, X. M. Cheng, et al., *Materials Science and Engineering a-Structural Materials Properties Microstructure and Processing* **483**, 637 (2008).
- 188 R. W. K. Honeycombe, *The Plastic Deformation of Metals* (Edward Arnold, London, 1984).
- 189 A. F. Voter, *Physical Review B* **57**, 13985 (1998).
- 190 A. F. Voter, *Abstracts of Papers of the American Chemical Society* **220**, U264 (2000).
- 191 Y. Mishin, A. Suzuki, B. P. Uberuaga, et al., *Physical Review B* **75**, 224101 (2007).
- 192 I. L. Chang and Y. C. Chen, *Nanotechnology* **18**, 315701 (2007).
- 193 K. Albe, J. Nord, and K. Nordlund, *Philosophical Magazine* **89**, 3477 (2009).
- 194 P. Villars, L. D. Calvert, and W. B. Pearson, *Pearson's handbook of crystallographic data for intermetallic phases* (ASM International, Materials Park, OH, 1991).

- ¹⁹⁵ J. Meister and W. H. E. Schwarz, *Journal of Physical Chemistry* **98**, 8245 (1994).
- ¹⁹⁶ R. S. Mulliken, *Journal of Chemical Physics* **23**, 1833 (1955).
- ¹⁹⁷ R. F. W. Bader, *Atoms in molecules: a quantum theory* (Clarendon Press, Oxford, 1990).
- ¹⁹⁸ F. L. Hirshfeld, *Theoretica Chimica Acta* **44**, 129 (1977).

Appendix A - The corundum structure

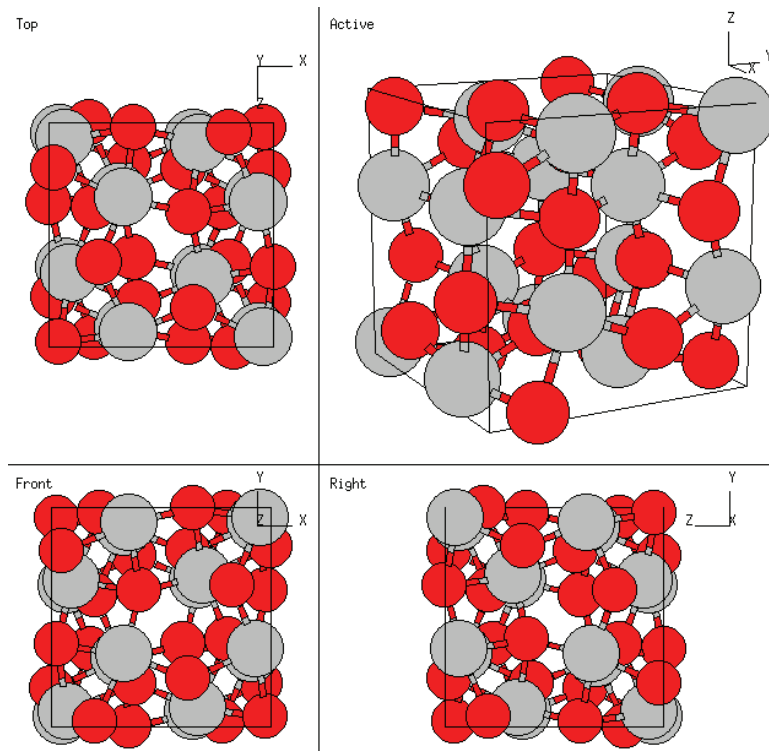


Figure A.1 The corundum structure. Al atoms in grey and O atoms in red from: http://cst-www.nrl.navy.mil/lattice/struk/d5_1.html

The corundum structure is described by specifying primitive vectors and basis vectors according to the following website: http://cst-www.nrl.navy.mil/lattice/struk/d5_1.html:

Although corundum has a rhombohedral primitive unit cell, Pearson's Handbook § and other references use the equivalent hexagonal lattice, which contains 3 primitive cells. Since the primitive cell is of more interest the rhombohedral structure is used.

According to Pearson's Handbook $a_{\text{HCP}} = 4.758 \text{ \AA}$. and $c_{\text{HCP}} = 12.99 \text{ \AA}$. This is translated to $a = 3.621 \text{ \AA}$. and $b = 0.257 \text{ \AA}$.

Corundum is defined up to two internal parameters. These internal parameters (x_1 and z_1) are in the hexagonal case $x_{\text{Al}} (\text{hex}) = 0.35228$ and $x_{\text{O}} (\text{hex}) = 0.3064$. On the rhombohedral lattice this translates to $z_1 = x_{\text{Al}} (\text{hex}) = 0.35228$ and $x_1 = \frac{1}{4} - x_{\text{O}} (\text{hex}) = -0.0564$

§ 194 P. Villars, L. D. Calvert, and W. B. Pearson, *Pearson's handbook of crystallographic data for intermetallic phases* (ASM International, Materials Park, OH, 1991).

Primitive vectors:

$$A1 = b X + a Y + a Z$$

$$A2 = a X + b Y + a Z$$

$$A3 = a X + a Y + b Z$$

Basis vectors:

$$B1 = + z1 (A1 + A2 + A3) = + z1 (2a + b) (X + Y + Z) \quad (A1)$$

$$B2 = - z1 (A1 + A2 + A3) = - z1 (2a + b) (X + Y + Z) \quad (A1)$$

$$B3 = + (\frac{1}{2} + z1) (A1 + A2 + A3) = + (\frac{1}{2} + z1) (2a + b) (X + Y + Z) \quad (A1)$$

$$B4 = - (\frac{1}{2} + z1) (A1 + A2 + A3) = - (\frac{1}{2} + z1) (2a + b) (X + Y + Z) \quad (A1)$$

$$\begin{aligned} B5 &= + x1 A1 + (\frac{1}{2} - x1) A2 + \frac{1}{4} A3 \\ &= + [(\frac{3}{4} - x1) a + x1 b] X + [(\frac{1}{4} + x1) a + (\frac{1}{2} - x1) b] Y + [\frac{1}{2} a + \frac{1}{4} b] Z \end{aligned} \quad (O)$$

$$\begin{aligned} B6 &= - x1 A1 - (\frac{1}{2} - x1) A2 - \frac{1}{4} A3 \\ &= - [(\frac{3}{4} - x1) a + x1 b] X - [(\frac{1}{4} + x1) a + (\frac{1}{2} - x1) b] Y - [\frac{1}{2} a + \frac{1}{4} b] Z \end{aligned} \quad (O)$$

$$\begin{aligned} B7 &= + (\frac{1}{2} - x1) A1 + (\frac{1}{4}) A2 + x1 A3 \\ &= + [(\frac{1}{4} + x1) a + (\frac{1}{2} - x1) b] X + [(\frac{1}{4} + x1) a + (\frac{1}{2} a + \frac{1}{4} b)] Y \\ &\quad + [(\frac{3}{4} - x1) a + x1 b] Z \end{aligned} \quad (O)$$

$$\begin{aligned} B8 &= - (\frac{1}{2} - x1) A1 - (\frac{1}{4}) A2 - x1 A3 \\ &= - [(\frac{1}{4} + x1) a + (\frac{1}{2} - x1) b] X - [(\frac{1}{4} + x1) a + (\frac{1}{2} a + \frac{1}{4} b)] Y \\ &\quad - [(\frac{3}{4} - x1) a + x1 b] Z \end{aligned} \quad (O)$$

$$\begin{aligned} B9 &= + \frac{1}{4} A1 + x1 A2 + (\frac{1}{2} - x1) A3 \\ &= + [\frac{1}{2} a + \frac{1}{4} b] X + [(\frac{3}{4} - x1) a + x1 b] Y + [(\frac{1}{4} + x1) a + (\frac{1}{2} - x1) b] Z \end{aligned} \quad (O)$$

$$\begin{aligned} B10 &= - \frac{1}{4} A1 - x1 A2 - (\frac{1}{2} - x1) A3 \\ &= - [\frac{1}{2} a + \frac{1}{4} b] X - [(\frac{3}{4} - x1) a + x1 b] Y - [(\frac{1}{4} + x1) a + (\frac{1}{2} - x1) b] Z \end{aligned} \quad (O)$$

Appendix B – Partial charge determination

In most ionic or covalent systems the charges are not distributed as multitudes of the elementary charge unit. Often the charge is smeared out between the atoms and across the bonds. As a consequence, charges with an absolute value smaller than one elementary charge unit so-called partial charges are produced. A lot of approaches try to assign these partial charges to the corresponding atoms based on various sources such as the wave functions, the electron density, spectroscopy or other experimental data. Meister and Schwarz^{**} review a lot of methods.

Probably, the most well-known method is the population analysis of the wave function by Mulliken^{††}. The Mulliken charges q_a^{mul} are obtained by subtracting the sum of products of overlap integrals S_{ij} with one-electron density matrix elements P_{ij} from the nuclear charge Z_a of an atom a .

$$q_a^{mul} = Z_a - \sum_{i,j \in a} P_{ij} S_{ji} \quad (37.)$$

Unfortunately, the result is known to be non-unique and that there can be artifacts.

People performing DFT calculations usually obtain in the end of their calculation directly the electron density, which can be directly partitioned to derive the atomic charges. Famous methods for this are the Bader's method^{‡‡} which splits up the molecular density into non overlapping pieces by separating the surfaces through the density minima along gradient lines from one nucleus to another.

$$q_a^{bad} = Z_a - \int_{\text{compartment } a} dr^3 \rho_{mol} \quad (38.)$$

Bader's charges are generally expected to be too big in absolute values.

^{**} 195 J. Meister and W. H. E. Schwarz, *Journal of Physical Chemistry* **98**, 8245 (1994).

^{††} 196 R. S. Mulliken, *Journal of Chemical Physics* **23**, 1833 (1955).

^{‡‡} 197 R. F. W. Bader, *Atoms in molecules: a quantum theory* (Clarendon Press, Oxford, 1990).

Hirshfeld charges ^{§§} are claimed to be more realistic. They are based on the definition of a promolecule or procrystal by superposition of the atomic ground state electron densities. They are assumed to be overlapping, neutral and spherically averaged. $\rho_{pro} = \sum_a \rho_a$. The atomic

Hirshfeld charge is then given by:

$$q_a^{hir} = Z_a - \int dr^3 \frac{\rho_a}{\rho_{pro}} \rho_{mol}. \quad (39.)$$

As the word procrystal indicates, this method fits well to describe the charge distribution assigned to point charges in a crystalline specimen.

§§ 198 F. L. Hirshfeld, *Theoretica Chimica Acta* **44**, 129 (1977).

A personal retrospect

This project for the simulation of O impurities in Al has many interesting aspects: Personally, I could apply a lot of my skills I gathered during my studies in computational science and engineering. The optimization of the charge determination problem of Streitz and Mintmire for the purpose of dilute O concentrations has been especially interesting for me. After a solution was found for this problem I have spent many weeks to program and test the serial and the parallel version of the MD code with variable charges and the local chemical potential approach. Mainly the parallel version has challenged me a lot. I knew the fitting of empirical potentials only from theory before I started my PhD and I have learned a lot in the practical execution of this task.

One of my tasks has been the application of my developments to investigate the role of O impurities in nc Al. The field of nc metals (and also materials science in general) has been rather new to me. Reading the current literature, discussing with other people, but also travelling to courses, workshops and conferences broadened my personal horizon a lot. I have learned various things starting from as simple concepts as the one of interstitials in crystalline materials to the rather challenging interactions of impurities with e.g. GBs or dislocations. A lot of people have contributed in this learning process. So, I am at the point where I want to thank many of these people who have broadened my mind and contributed to the potential success of this thesis.

First of all, I want to thank Prof. Helena Van Swygenhoven, my thesis director, for giving me the possibility to investigate this interesting topic. She set up an excellent environment to work in e.g. the stimulating infrastructure at PSI, the productive collaboration with Dr. Olivier Politano from U-Bourgogne in Dijon and the financial support for me and my family. During the thesis, Helena has contributed with several discussions on my topic. In such discussions the road map for the project has been adjusted from time to time. As group leader, she has cared also for a constructive and pleasant climate in the group.

The technical advice during the work came mostly from Dr. Peter Derlet at PSI and from Olivier. Peter has always had an open door to discuss anything on a very detailed but also very theoretical level. With Olivier, the MD code has been transferred to a MD code with variable charges which includes all the developments presented in this thesis. Additionally further or other developments have been studied in literature and/or have even been tested in the code, e.g. multiple time-steps algorithms, separate thermostats for Al and O, the fast multipole method or

parallel solvers for linear systems of equations. Oliver also contributed a lot by his literature knowledge on the specific topic of simulation of O in metallic environments. All the three people mentioned so far have contributed a lot to my posters, presentations, and publications. Last but not least, they have also been critical readers and correctors of several versions of my thesis.

As a next person, I want to thank Dr. Christian Brandl for sharing an office with me for more than three years. Christian and me, we have had a lot of supportive discussions. As both of us have been working in the field of atomistic simulations a regular transfer of knowledge but also computational tricks and tools has taken place. Prof. Erik Bitzek, a former postdoctoral researcher in the Materials Science and Simulation group, shared his knowledge on MD in generous way so that I could learn a lot from his advices. Especially, he pointed out the difficulty of the complexity of the nc samples. Samuele Chiesa has criticized my work on a more theoretical basis and has always been helpful to understand the physics behind the problems. All other group members contributed either scientifically or at least in making my life more enjoyable with dinners, parties or spending free time in the mountains. I thank all of them (Dr. Steven Van Petegem, Dr. Alexander Evans, Dr. Jorge Martinez Garcia, Dr. Stefan Brandstetter, Dr. Robert Maaß, Ning Gao, Julien Zimmermann, Deniz Kecik, Stephane Pierret, Michael Weisser, Cecile Marichal, Mario Velasco Sanchez and a few guest students) very much for the time we spent together.

During the simulation of the bicrystals I have been in frequent e-mail contact with Dr. Vladimir Ivanov from George Mason University in Fairfax VA. I want also to thank him for his valuable support in terms of additional information and cross-checking of preliminary results.

Beside the work at PSI I have had several chances to get advises for the continuation of my work in the form of private communications with professors. I want to mention here the conversation with Prof. Diana Farkas from Virginia Tech. in Blacksburg VA and Marc Hou from ULB in Bruxelles at the TMS Annual Meeting 2007 in Orlando, the comments of Yuri Mishin from George Mason University in Fairfax VA at the Small Scale Plasticity Workshop in Braunwald and the chat with Daniel Gianola from U Penn. in Philadelphia PA at the MRS Fall Meeting 2009 in Boston.

For finishing my thesis I want to thank the readers Prof. Marc Hou from ULB in Bruxelles, Prof. Ralph Spolenak from ETH Zurich, and Prof. Efthimios Kaxiras, EPFL Lausanne for their constructive comments on my work. Additionally I want to thank Prof. Nadine Baluc, EPFL Lausanne for chairing the examination procedure.

Last but not least I feel the need to acknowledge my family: My wife Jolanda and my three kids Seraina, Olivia and Fabris. They have had the patience to let me work on this subject without being offered a fortune. My travelling, which I have appreciated a lot, has always been a hard time for my wife, as she has been alone with an increasing number of kids. But I have always felt a lot of support of them what has always been an additional motivation for me.

Curriculum vitae

Personal details

Date of birth	14 th of March, 1979
Place of origin	Menzingen ZG
Marital status	Married, with 3 children

Education

2000-2003	Studies of mathematics and physics at ETH Zurich
2003-2006	Studies of computational science and engineering at ETH Zurich
2006-2010	Doctoral school in materials science and engineering at EPF Lausanne / PhD work in the Materials Science and Simulation group at Paul Scherrer Institut, Villigen

Publications

- ‘Comparison of thermodynamic properties of coarse-grained and atomic level simulation models’, *ChemPhysChem* **8** (2007), p. 452 – 461
- ‘Statistical analysis of quantum chemical data using generalized XML/CML archives for the derivation of molecular design rules’, *Chimia* **61** (2007), p. 165 – 168
- ‘A local chemical potential approach within the variable charge method formalism’, *Modelling and Simulation in Materials Science and Engineering*, **16** (2008), 025006
- ‘Variable-charge method applied to study coupled grain boundary migration in the presence of oxygen’, *Acta Materialia*, **57** (2009), p. 1988 – 2001

Awards

- Willi-Studer-Preis of ETH Zurich: Best diploma in computational science and engineering of the year 2006
- Poster award at the annual meeting of the Swiss chemical society 2006
- Selected for joint workshop with Tokyo Institute of Technology at the 2009 doctorals day in materials science at EPF Lausanne